Viscoelastic Finite Difference Modeling

Joakim O. Blanch
Johan O.A. Robertsson
William W. Symes

February, 1993

TR93-04

Viscoelastic
Finite Difference Modeling

Joakim O. Blanch
Johan O. A. Robertsson
William W. Symes

Rice University
Houston, Texas, U.S.A.

February 1993

Contents:

ABSTRACT

Real earth media disperse and attenuate propagating waves. This anelastic behavior can be well described by a viscoelastic model. We have developed a finite difference simulator to model wave propagation in viscoelastic media. The finite difference method was chosen in favor of other methods for several reasons. Finite difference codes are more portable than, for instance, pseudo-spectral codes. Moreover, finite difference schemes provide a convenient environment to define complicated boundaries. The finite difference method for viscoelastic wave propagation has been thoroughly investigated with convergence tests, dispersion and stability analyses. Two 2-D examples illustrate the difference between viscoelastic and elastic wave propagation.

INTRODUCTION

To a high degree, elasticity is a good model for wave propagation through the earth. No real materials, however, are perfectly elastic, but rather anelastic. In real media, wave energy is gradually converted into heat. Attenuation of propagating wave forms is in some cases quite significant and could be a source of erroneous results in forward modeling, inversion and imaging if neglected (*Liu et al.*, 1976). The quality factor, Q, characterizes the attenuation of waves in a material. This is a measure of how many wavelengths a wave must propagate through the material before its amplitude drops by 1/e. It is a practical measure for field measurements and it is therefore desirable to develop a theoretical model using quality factors for pressure- and shear-waves.

There are several ways of modeling anelastic phenomena. One approach is to model materials through their mechanical analogs using components such as springs and dashpots. Such a model is called a viscoelastic model and in the elastic limit this reduces to a single spring with a spring constant corresponding to the elastic properties of the material. The so called standard linear solid is a simple viscoelastic model containing of a spring in parallel with spring and a dashpot in series. An array of standard linear solids in parallel may be used to approximate a specific viscoelastic model with a certain Q versus frequency relation.

Earth materials have been shown to have a nearly constant quality factor, Q, over the seismic frequency range (review in *Bourbie et al.*, 1987). A viscoelastic model consisting of a series of standard linear solids in parallel can closely approximate a constant Q over a specified frequency range. We have developed a constant Q optimization algorithm based on work by *Liu et al.* [1976]. As a rule by thumb one standard linear solid per octave in the specified frequency band is sufficient to achieve a good approximation. Since attenuation and dispersion are related through Kramers-Krönig's relation, the constant Q model also yields a realistic dispersion relation. *Futterman* [1962] derived a theoretical dispersion relation for materials with a constant Q. *Wuenschel* [1965] experimentally showed Plexiglas and shale to have nearly frequency-independent quality factor over several octaves.

We based our finite difference approach on a system of first order linear partial differential equations derived through the introduction of so called memory variables. The stress-strain relation contain a convolution in the viscoelastic case. Viscoelastic media may therefore be regarded as remembering earlier deformation states. This is reflected through the memory variables which are added to the equations governing the components of the stress tensor. The memory variables are governed by separate

differential equations. *Day and Minster* [1984] also derived a system of first order partial differential equations by using Padé approximations to approximate the convolution in the stress-strain relation.

Control of numerical dispersion is important since viscoelastic media are intrinsically dispersive. For this reason earlier viscoelastic wave propagation simulators have been based on pseudo-spectral methods (e.g. *Carcione et al.*, 1988). Numerical dispersion can to the same degree also be controlled using finite difference methods on denser grids. A computationally expensive part of pseudo-spectral schemes is the FFT that must be performed each time step. Moreover, efficient pseudo-spectral codes tend to be machine dependent due to FFT-routines, etc. This is not the case for finite difference codes. The principal arguments for choosing a finite difference method to simulate viscoelastic wave propagation are portability of efficient code, ability to model complicated boundaries accurately, and the ability to control the simulation accuracy.

We have implemented and investigated O(2,2), O(2,4), and O(4,4) accurate schemes. These have been thoroughly investigated through convergence tests, dispersion and stability analyses. The discrete dispersion relation for the system was found to be the product of a well known term responsible for wave propagation and another term responsible for attenuation. The stability criteria for the viscoelastic schemes are approximately the same as for the analog elastic schemes. The Courant number must however be adjusted to the highest phase velocity (found at the infinite frequency) in the viscoelastic medium. We have performed convergence tests where we compared the analytic solution for single wavenumbers to the numerical solution for identical initial conditions.

In this paper we will start with a brief review of viscoelastic theory. We will then present our algorithm for constant Q optimization. We will then pursue the theory by deriving the equations governing viscoelastic wave propagation and also formulate these as a system of linear first order partial differential equations. Next we will summarize the implementation and the tests we did for the different schemes. After this we will present results from convergence tests and stability and dispersion analyses. For practical reasons we have limited this analysis to 1-D. Our results may be directly applied to modeling of higher dimensions viscoelastic wave propagation. We describe explicitly the 2-D extension of our method and exhibit two examples where disregarding anelasticity seriously limit the realism of the problems.

THEORETICAL MODEL - LINEAR VISCOELASTICITY

In this section we derive a theoretical anelastic model based on viscoelastic theory, a phenomenological way to describe combined elastic and viscous behavior of materials. The basic hypothesis is that a current value of the stress tensor depends upon the history of the strain tensor. The simplest viscoelastic models are the Maxwell and the Kelvin-Voigt models, which essentially represent a fluid and a solid respectively. Both models will be treated more thoroughly below.

Basic definitions

The viscoelastic hypothesis, can be described as,

$$\sigma_{ij}(t) = \overset{\infty}{\underset{s=0}{\psi_{ij}}}(\varepsilon_{kl}(t-s), \varepsilon_{kl}(t)) \tag{1}$$

(*Christensen*, 1982) where ψ is a linear tensor valued functional which transforms each strain history, $\varepsilon_{ij}(t), -\infty \le t \le \infty$, into the corresponding stress history, $\sigma_{ij}(t)$. In general all field variables depend both on time and position. If the functional is linear and the strain history assumed to be continuous, Riesz' representation theorem allows us to write the functional as a Stieltjes integral,

$$\sigma_{ij}(t) = \int_0^{\infty} \varepsilon_{kl}(t-s) dG_{ijkl}(s). \tag{2}$$

The fourth order tensor, G, collapses into two independent functions for an isotropic and homogeneous material, assuming the strain history to be a symmetric tensor defined as in linear elasticity. By including a step discontinuity for the strain at t=0, constraining $\varepsilon_{ij}(t) = 0$ for t<0, and assuming that $G_{ijkl} \in C^1$, the constitutive relation (2) reduces to,

$$\sigma_{ij}(t) = G_{ijkl}(0)\varepsilon_{kl}(t) + \int_0^t G_{ijkl}(t-\tau)\frac{d\varepsilon_{kl}(\tau)}{d\tau} d\tau \tag{3}$$

In 1-D, the special case of simple shear in an isotropic homogeneous material (3) reduces to,

$$\sigma(t) = G(0)\varepsilon(t) + \int_0^t G(t-\tau)\dot{\varepsilon}(\tau)d\tau \tag{4}$$

where

$$\dot{\varepsilon}(t) = \frac{d\varepsilon(t)}{dt}$$

G is called the stress relaxation function and is the viscoelastic analog to the Lamé constant, μ, in linear elasticity. Equation (4) may also be written as,

$$\sigma = G * d\varepsilon = \varepsilon * dG \tag{5}$$

where * denotes Stieltjes convolution. For sufficiently well behaving functions G and ε, (5) can be written as,

$$\sigma = G * \dot{\varepsilon} = \varepsilon * \dot{G} \tag{6}$$

where * denotes conventional convolution.

The creep compliance, J, is the inverse of G, in the sense that,

$$\varepsilon = \sigma * \dot{J} = J * \dot{\sigma} \tag{7}$$

By Laplace transforming (6) and (7) and eliminating the stress and the strain, we obtain,

$$s\hat{J}(s)s\hat{G}(s) = 1 \tag{8}$$

Viscoelastic solids and fluids may be distinguished by the behavior of their relaxation functions at infinite time, that is by studying G(∞). If G(∞)=0 the material is defined as a fluid, whereas when G(∞)≠0 the material is defined as a solid.

Differential operator form of stress-strain relations in one dimension

If we assume that the Laplace transform of G can be approximated by a rational function, this is

$$s\hat{G}(s) = \frac{Q(s)}{P(s)} \tag{9}$$

then the stress-strain relation is equivalent to,

$$P(D)\sigma(t) = Q(D)\varepsilon(t) \tag{10}$$

where

$$\begin{aligned} P(D) &= \sum_{k=0}^{N} p_k D^k \\ Q(D) &= \sum_{k=0}^{N} q_k D^k \end{aligned} \tag{11}$$

Here, D is the differential operator d/dt and N is an arbitrary natural number. This is called the differential operator form of the stress-strain relations. By Laplace transforming (10) and (11) we obtain,

$$P(s)\hat{\sigma}(s) - \frac{1}{s}\sum_{k=1}^{N} p_k \sum_{r=1}^{k} s^r \sigma^{(k-r)}(0) = Q(s)\hat{\varepsilon}(s) - \frac{1}{s}\sum_{k=1}^{N} q_k \sum_{r=1}^{k} s^r \varepsilon^{(k-r)}(0) \tag{12}$$

Through identification with terms in (9) and (12) we obtain,

$$\sum_{r=k}^{N} p_r \sigma^{(r-k)}(0) = \sum_{r=k}^{N} q_r \varepsilon^{(r-k)}(0). \tag{13}$$

The above assumption of a rational approximation can be justified by realizing that a realistic relaxation function only can have step discontinuities, which results in a 1/s behavior for the Laplace transform of G for large s. Hence, if we assume the order of Q to be less than or equal to the order of P+1 and the rational sP(s)/Q(s) to have no multiple roots, we can express G as a constant plus a sum of N+1 (or less) inverse first order polynomials. That is,

$$G(s) = K + \sum_{k=0}^{N} \frac{a_k}{b_k + s} \tag{14}$$

The case when the order of Q is greater than the order of P+1 represents infinite stress at finite strain or in other words, the non-physical case of rigid bodies. By inverse Laplace transforming (14) the general solution for G in the time domain is obtained as,

$$G(t) = K + \sum_{k=0}^{N} c_k e^{-\frac{t}{\tau_k}} \tag{15}$$

A mechanical viscoelastic model

The mechanical models used in viscoelasticity are usually expressed as combinations of elastic and viscous elements. The elastic model is the spring and the viscous model is the dashpot (illustrated in Figure 1a). The constitutive relations for these are,

$$\sigma = k\varepsilon, \text{ for the spring,}$$
$$\text{and} \tag{16}$$
$$\sigma = \eta\dot{\varepsilon}, \text{ for the dashpot.}$$

These models may be combined either in series or in parallel to form different viscoelastic elements. A spring and a dashpot connected in series is called the Maxwell model, whereas a parallel connection is called the Kelvin-Voigt model. The Maxwell model essentially represents a fluid, whereas the Kelvin-Voigt model represents a solid. Another important viscoelastic configuration, the standard linear solid, is composed of a Maxwell model in parallel with a spring. This is illustrated in Figure 1b. A similar configuration is the so called Zener model, which consists of a Kelvin-Voigt model in series with a spring. Both the standard linear solid and the Zener model are viscoelastic solids.

The relaxation function, G, for the standard linear solid is,

$$G(t) = k_1 e^{-t/\tau_\sigma} + k_2 \tag{17}$$

where

$$\tau_\sigma = \eta / k_1$$

and the creep compliance, J, is,

$$J(t) = \frac{1}{k_2} - \frac{k_1}{k_2(k_1 + k_2)} e^{-t/\tau_\varepsilon} \tag{18}$$

where

$$\tau_\varepsilon = \frac{\eta(k_1 + k_2)}{k_1 k_2}$$

Equation (17) may also be written on the form,

$$G(t) = k_2(1 + (\frac{\tau_\varepsilon}{\tau_\sigma} - 1)e^{-t/\tau_\sigma}) \tag{19}$$

L standard linear solids in parallel yield the relaxation function, G, as,

$$G(t) = K(1 - \sum_{l=1}^{L}(1 - \frac{\tau_{\varepsilon l}}{\tau_{\sigma l}})e^{-t/\tau_{\sigma l}}) \tag{20}$$

where

$$K = \sum_{l=1}^{L} k_{2l}$$

$$\tau_{\sigma l} = \eta_l / k_{1l}$$

$$\tau_{\varepsilon l} = \eta \frac{k_1 + K}{k_1 K}.$$

Equations (15) and (20) are equivalent and we may therefore describe an essentially arbitrary linear viscoelastic material as an array of several standard linear solids in parallel. This is also equivalent to a spring in parallel with an array of several Maxwell elements in parallel. Expressing the causality constraint explicitly, the form we will use for a general viscoelastic material is,

$$\psi(t) = M_R\left(1 - \sum_{l=1}^{L}\left(1 - \frac{\tau_{\varepsilon l}}{\tau_{\sigma l}}\right)e^{-t/\tau_{\sigma l}}\right)\theta(t) \tag{21}$$

where M_R is the relaxed modulus of the medium (*Pipkin*, 1986) and $\theta(t)$ is the Heaviside function defined as,

$$\theta(t) = \begin{cases} 0, t < 0 \\ 1, t \geq 0 \end{cases}$$

REALISTIC ATTENUATION AND DISPERSION MODELING

Certain experimental results have shown that earth materials generally have constant Q, both for pressure and shear waves over a limited range of frequencies (review in *Bourbie et al.,* 1987). Thus it is highly desirable to find a way to model a constant Q, which in turn will yield a realistic dispersion relation (*Futterman*, 1962). In this section we describe an algorithm for Q-optimization for an array of standard linear solids in parallel.

Constant Q optimization

The quality factor, Q, is defined as,

$$Q(\omega) = \frac{\mathrm{Re}\left[M_C(\omega)\right]}{\mathrm{Im}\left[M_C(\omega)\right]} \tag{22}$$

where $M_C(\omega)$ is the complex bulk modulus, defined as the Fourier transform of $\psi(t)$, which for the case of L standard linear solids was derived in (21).

Our objective is to optimize Q such that it is approximately constant equal to Q_0 over a limited passband. The inverse problem is better formulated if we optimize 1/Q instead of Q, which of course does not limit us. For an array of L standard linear solids, this is,

Find

$$Min\ \phi = Min \int_{Pass\ Band} \left(Q_0^{-1} - Q^{-1}\right)^2 d\omega$$

where

$$Q^{-1} = \frac{\sum_{l=1}^{L} \frac{\omega(\tau_{\varepsilon l} - \tau_{\sigma l})}{1+\omega^2\tau_{\sigma l}^2}}{1 - L + \sum_{l=1}^{L} \frac{1+\omega^2\tau_{\varepsilon l}\tau_{\sigma l}}{1+\omega^2\tau_{\sigma l}^2}} \tag{23}$$

This inverse problem is ill conditioned, and further simplifications are necessary to obtain an applicable algorithm. We found that for most cases of interest (*Bourbie et al.*, 1987) one can make the approximation $\tau_{\varepsilon l} \approx \tau_{\sigma l}$. This approximation and (23) yields,

$$Q^{-1} \approx \sum_{l=1}^{L} \frac{\omega(\tau_{\varepsilon l} - \tau_{\sigma l})}{1+\omega^2 \tau_{\sigma l}^{\ 2}} \tag{24}$$

From (23), we can calculate Q^{-1} for one pair of relaxation mechanisms. This is,

$$Q^{-1} = \frac{\omega(\tau_\varepsilon - \tau_\sigma)}{1+\omega^2 \tau_\sigma \tau_\varepsilon} \tag{25}$$

Note that when $\tau_{\varepsilon l} \approx \tau_{\sigma l}$, (24) can be regarded as the sum of one-pair relaxation mechanism models given by (25).

For one pair of relaxation mechanisms, the function Q^{-1} has a unique maximum at a certain frequency given by,

$$\omega_{\max} = \frac{1}{\sqrt{\tau_\varepsilon \tau_\sigma}} \tag{26}$$

Since $\tau_{\varepsilon l} \approx \tau_{\sigma l}$, we use the notation "to fix a pair of relaxation mechanisms at a certain frequency" when setting,

$$\tau_{\sigma l} = \frac{1}{\omega} \tag{27}$$

at the desired frequency.

Using (23) we optimized Q^{-1} with respect to the variables $(\tau_{\varepsilon l} - \tau_{\sigma l})$ and $\tau_{\sigma l}$, using the conjugate gradient method. In Figure 2, we have optimized 3 pairs of relaxation mechanisms for a constant Q of 100, between 100 and 500 Hz. Note that the optimized Q is very close to the desired Q in the frequency interval. It should be emphasized that the approximation $\tau_{\varepsilon l} \approx \tau_{\sigma l}$ is better the larger Q is. The method is slow, but as we shall see there is a more efficient way to do the optimization. In Figure 3 we study the dependence of Q on perturbations of the optimized mechanisms. The effect of increasing all relaxation times by 20% is minimal. This is also the case if we would increase them with as much as 100%. The effect is much more dramatic when only $\tau_{\sigma l}$ is increased by 20%, while keeping $\tau_{\varepsilon l}$ constant. Thus, a small perturbation in one of the

relaxation times in a pair has a significant impact on Q, while equal perturbations in both relaxation times in a pair have negligible effects. From the experiments we draw two conclusions. First, the difference between $\tau_{\varepsilon l}$ and $\tau_{\sigma l}$ essentially determines the magnitude of Q. Second, when optimizing Q, the relaxation times will be evenly distributed over a logarithmic scale ranging from the lower bound of the pass band to the upper bound, in the sense discussed above. One pair of relaxation mechanisms per octave is sufficient to yield a constant Q over a pass band. By distributing $\tau_{\sigma l}$ in the way described above, our problem is reduced to an over-determined linear system of equations, where the only variables are $(\tau_{\varepsilon l} - \tau_{\sigma l})$. This was solved by using singular value decomposition.

In Figure 4 we have optimized 3 relaxation mechanisms for a constant Q of 50, from 100 Hz to 500 Hz. Here Q is overestimated by an almost constant offset (Q=52 instead of Q=50). The error is larger than in the case illustrated above, since the approximations are worse the lower Q is. This is due to the difference between the relaxation mechanisms in a pair which increases with decreasing Q. If we, for some reason, want to have a very accurate approximation of a constant Q of 50, the optimization may be done at Q=48 for instance.

We now have an algorithm to generate a realistic attenuation and dispersion model to use in the viscoelastic code.

VISCOELASTIC WAVE PROPAGATION

The equations describing wave propagation in viscoelastic media can be derived in terms of the creep compliance or the stress relaxation modulus. Here we choose to derive it from the latter. For simplicity, we will derive the equations for the one-dimensional case where the viscoelastic equations are the same as the viscoacoustic. A generalization to higher dimensions is analogous to the derivation done here. The constitutive equation is,

$$\sigma = \psi * \dot{\varepsilon} \tag{28}$$

The dot denotes a time derivative, σ is the stress, ε is the strain, and ψ is the complex modulus (*Pipkin*, 1986). As described above a viscoelastic medium may be modeled as an array of standard linear solids in parallel. Each is characterized by two variables, the stress relaxation time, τ_σ, and the strain relaxation time, τ_ε. The relaxation modulus for an array of L parallel standard linear solids is given by (21). We will refer to a particular *set of relaxation mechanisms* as the two different relaxation times corresponding to one of the steps.

From the definitions of pressure and dilatation (*Gurtin*, 1981) we know that,

$$\sigma = -p \tag{29}$$

and

$$\dot{\varepsilon} = v_x \tag{30}$$

Taking the time derivative of (28) and using (21) leads to,

$$-\dot{p} = \dot{\psi} * v_x \tag{31}$$

that is,

$$-\dot{p} = M_R\left(1 - \sum_{l=1}^{L}\left(\frac{\tau_{\varepsilon l}}{\tau_{\sigma l}} - 1\right)\right)v_x + \sum_{l=1}^{L}\left(M_R\theta(t)\frac{1}{\tau_{\sigma l}}\left(1 - \frac{\tau_{\varepsilon l}}{\tau_{\sigma l}}\right)e^{-t/\tau_{\sigma l}}\right) * v_x \tag{32}$$

The convolution terms in (32) may be eliminated by introducing so called memory variables, which will be denoted r_l (*Carcione et al.*, 1988). Equation (32) thereby reduces to,

$$-\dot{p} = M_R\left(1-\sum_{l=1}^{L}\left(\frac{\tau_{\varepsilon l}}{\tau_{\sigma l}}-1\right)\right)v_x + \sum_{l=1}^{L} r_l \tag{33}$$

where

$$r_l = M_R\left(\theta(t)\frac{1}{\tau_{\sigma l}}\left(1-\frac{\tau_{\varepsilon l}}{\tau_{\sigma l}}\right)e^{-t/\tau_{\sigma l}}\right) * v_x, \quad 1 \le l \le L \tag{34}$$

From (34) we see that r_l are governed by convolutions of v_x with exponential functions, i.e. the kernels of r_l are of exponential character. A set of first order linear differential equations may be obtained instead of the convolutions as follows. First, by taking the time derivative of (34) we obtain,

$$\dot{r}_l = M_R\left(\frac{d}{dt}\left(\theta(t)\frac{1}{\tau_{\sigma l}}\left(1-\frac{\tau_{\varepsilon l}}{\tau_{\sigma l}}\right)e^{-t/\tau_{\sigma l}}\right)\right) * v_x, \quad 1 \le l \le L \tag{35}$$

which gives us,

$$\begin{aligned}\dot{r}_l = &-\frac{1}{\tau_{\sigma l}} M_R\left(\theta(t)\frac{1}{\tau_{\sigma l}}\left(1-\frac{\tau_{\varepsilon l}}{\tau_{\sigma l}}\right)e^{-t/\tau_{\sigma l}}\right) * v_x + \\ &\left(\delta(t) M_R \frac{1}{\tau_{\sigma l}}\left(1-\frac{\tau_{\varepsilon l}}{\tau_{\sigma l}}\right)e^{-t/\tau_{\sigma l}}\right) * v_x, \quad 1 \le l \le L\end{aligned} \tag{36}$$

From (34) we see that (36) reduces to,

$$\dot{r}_l = -\frac{1}{\tau_{\sigma l}} r_l + M_R \frac{1}{\tau_{\sigma l}}\left(1-\frac{\tau_{\varepsilon l}}{\tau_{\sigma l}}\right)v_x, \quad 1 \le l \le L \tag{37}$$

We have now derived a set of first order linear differential equations for the memory variables. Newton's second law completes the full description of wave propagation in a viscoelastic medium. This is,

$$\rho \dot{v} = -p_x \tag{38}$$

(33), (37) and, (38) is the system of first order linear differential equations that fully describe one dimensional viscoelastic wave propagation in a medium with L sets of standard linear solid relaxation mechanisms that we will use.

IMPLEMENTATION AND NUMERICAL EXPERIMENTS

The system of L+2 first order linear partial differential equations we wish to solve is given by (33), (37), and (38). This is,

$$\begin{cases} -\dot{p} = M_R\left(1 - \sum_{l=1}^{L}\left(\frac{\tau_{\varepsilon l}}{\tau_{\sigma l}} - 1\right)\right)v_x + \sum_{l=1}^{L} r_l \\ \rho\dot{v} = -p_x \\ \dot{r}_l = -\frac{1}{\tau_{\sigma l}} r_l + M_R \frac{1}{\tau_{\sigma l}}\left(1 - \frac{\tau_{\varepsilon l}}{\tau_{\sigma l}}\right)v_x, \quad 1 \le l \le L \end{cases}$$

We made several tests for different schemes using a Ricker wavelet with a central frequency at 35 Hz propagating in the positive x direction in a 2000 m long homogeneous interval with periodic boundary conditions. The initial condition is plotted in Figure 5. The relaxation modulus (corresponds to the Lamé constant in the elastic case), M_R, was 8 GPa and the density 2000 kg/m^3. This leads to a velocity of 2000 m/s in the 0 Hz limit. For simplicity we used one set of relaxation mechanisms per Q-model. These are listed in Table 1.

Equation (37) proved to be stiff under some extreme circumstances but otherwise quite robust. We investigated several time stepping schemes to approximate (37) such as, Adams-Bashforth methods, Gear's methods, and the Crank-Nicholson scheme. In Figures 6 and 7 we display two cases with severe numerical dispersion using an O(2,4) scheme for (33) and (38), comparing the 4:th order Gear's method to Crank-Nicholson as approximation for (37). Even in these extreme cases the difference is minimal and hence we decided to use the Crank-Nicholson approximation for (37).

We decided to use a Leapfrog scheme to approximate the time derivatives in (33) and (38). This conserves energy which is important since we must be able to distinguish between physical and numerical attenuation when modeling anelastic media. One of the principal arguments for using spectral methods instead of finite differences has been to avoid confusing physical dispersion with numerical dispersion. If all spatial derivatives in our system of differential equations is approximated by second order accurate central differences the numerical dispersion is indeed severe. This scheme will be referred to as the O(2,2) scheme. A Courant number close to 1 and a spatial discretization of 1m (25

grid-points per wavelength at the highest frequency) proved to be optimal. In Figure 8 we compare snapshots at 2.25 s for the O(2,2) code at different values of Q. Q=10,000 can be regarded as the acoustic limit and as we can see the wavelet has suffered from significant numerical dispersion. As we shall see later, this scheme also does not model the attenuation correctly.

Dablain (1986) and *Levander* (1988) have investigated the accuracy of high order spatial accurate schemes for wave propagation. Increasing the spatial accuracy from second to fourth order improves the dispersion characteristics dramatically. In what we will refer to as the O(2,4) scheme all second order accurate approximations of the spatial derivatives have been replaced by fourth order accurate approximations. In Figure 9 we compare snapshots at 2.25 s at different values of Q. There is no visible numerical dispersion and moreover, as we shall see, the attenuation is modeled accurately. In Figures 10 and 11 we have varied the Courant number and the spatial discretization respectively. A Courant number of 0.2 and a spatial discretization of 2 m (12 grid-points per wavelength at the highest frequency) proved to be optimal. This scheme has several advantages. First, it is relatively computationally inexpensive (compared to the O(2,2) scheme and the O(4,4) scheme which we will describe next). It also models wave propagation in viscoelastic media accurately to a high degree. The major drawback is its poor characteristics at high Courant numbers. It is necessary to go as low as a Courant number of 0.2 in order to have sufficiently low numerical dispersion. On the other hand, half as many grid-points per wavelength are sufficient compared to the O(2,2) scheme.

The O(2,4) finite difference approximation for the system of differential equations is,

$$\frac{p_j^{n+1} - p_j^{n-1}}{2\Delta t} = -M_R\left(1 - \sum_{l=1}^{L}\left(\frac{\tau_{\varepsilon l}}{\tau_{\sigma l}} - 1\right)\right)\frac{-v_{j+2}^n + 8v_{j+1}^n - 8v_{j-1}^n + v_{j-2}^n}{12\Delta x} - \sum_{l=1}^{L} r_{j,l}^n \tag{39}$$

$$\rho\frac{v_j^{n+1} - v_j^{n-1}}{2\Delta t} = -\frac{-p_{j+2}^n + 8p_{j+1}^n - 8p_{j-1}^n + p_{j-2}^n}{12\Delta x} \tag{40}$$

$$\frac{r_{j,l}^{n+1}-r_{j,l}^{n}}{\Delta t}=-\frac{1}{2\tau_{\sigma l}}\left(r_{j,l}^{n+1}+r_{j,l}^{n}\right)+M_R\frac{1}{2\tau_{\sigma l}}\left(1-\frac{\tau_{\varepsilon l}}{\tau_{\sigma l}}\right)\cdot$$
$$\cdot\left(\frac{-v_{j+2}^{n}+8v_{j+1}^{n}-8v_{j-1}^{n}+v_{j-2}^{n}}{12\Delta x}+\frac{-v_{j+2}^{n+1}+8v_{j+1}^{n+1}-8v_{j-1}^{n+1}+v_{j-2}^{n+1}}{12\Delta x}\right) \tag{41}$$

$l=1,\ldots\quad\ldots,L$

The equivalent differential equations (EDE) are derived by using Taylor expansions in (39), (40), and (41). We obtain,

$$\dot{p}=-M_R\left(1-\sum_{l=1}^{L}\left(\frac{\tau_{\varepsilon l}}{\tau_{\sigma l}}-1\right)\right)v_x-\sum_{l=1}^{L}r_l-\frac{\Delta t^2}{6}\dddot{p}+O\left(\Delta t^4,\Delta x^4\right) \tag{42}$$

$$\rho\dot{v}=-p_x-\frac{\Delta t^2}{6}\dddot{v}+O\left(\Delta t^4,\Delta x^4\right) \tag{43}$$

$$\dot{r}_l=-\frac{1}{\tau_{\sigma l}}r_l+M_R\frac{1}{\tau_{\sigma l}}\left(1-\frac{\tau_{\varepsilon l}}{\tau_{\sigma l}}\right)v_x+O\left(\Delta t^2,\Delta x^4\right),\quad l=1,\ldots\quad\ldots,L \tag{44}$$

Hence, we have shown that the schemes are second order accurate in time and fourth order accurate in space.

It is sometimes possible to improve the accuracy by using a so called compact scheme (*Dablain*, 1986). The accuracy of finite difference approximations such as (39) through (41) can be increased from second to fourth order in time by subtracting the highest order inaccurate term in the EDE (equations (42), (43), and (44)) as fourth order spatial finite difference approximations using the exact system of differential equations (equations (33), (37), and (38)). For the case when there only is one pair of relaxation mechanisms, the third order time derivatives expressed as spatial derivatives are,

$$v_{ttt}=-M_R\frac{\tau_\varepsilon}{\tau_\sigma}\frac{1}{\rho^2}p_{xxx}-\frac{1}{\tau_\sigma}\frac{1}{\rho}r_x-M_R\frac{1}{\tau_\sigma}\frac{1}{\rho}\left(\frac{\tau_\varepsilon}{\tau_\sigma}-1\right)v_{xx} \tag{45}$$

$$p_{tt} = -M_R{}^2\left(\frac{\tau_\varepsilon}{\tau_\sigma}\right)^2\frac{1}{\rho}v_{xxx} - M_R\frac{\tau_\varepsilon}{\tau_\sigma}\frac{1}{\rho}r_{xx} - \frac{1}{\tau_\sigma{}^2}r - \\ - M_R\frac{1}{\tau_\sigma{}^2}\left(\frac{\tau_\varepsilon}{\tau_\sigma}-1\right)v_x - M_R\frac{1}{\tau_\sigma}\frac{1}{\rho}\left(\frac{\tau_\varepsilon}{\tau_\sigma}-1\right)p_{xx} \tag{46}$$

We used (45) and (46) in (42) and (43) to derive a fourth order space and time accurate compact scheme for (33) and (38). We did not increase the accuracy in time for (37) since this did not improve the result to any significant extent. We will refer to this scheme as the O(4,4) scheme.

We found a Courant number close to 1 and 2m grid-spacing (12 grid-points per wavelength at the highest frequency) to be optimal. This is illustrated in Figures 12 and 13. In Figure 14 we compare snapshots at 2.25 s for the O(4,4) scheme at different values of Q. No numerical dispersion is visible. The accuracy gained compared to the O(2,4) scheme is minimal but we are now able to use a four times as large Courant number.

In Figures 15 and 16 we compare snapshots at 2.25 s for the O(2,2), the O(2,4), and the O(4,4) scheme for a optimal choice of simulation parameters at Q=50 and Q=10,000. The solutions from the O(4,4) and the O(2,4) schemes are close with minimal numerical dispersion while the O(2,2) scheme is quite poor.

It is possible to obtain analytic viscoacoustic solutions for some simple geometries by replacing the velocity in the Fourier transform of the acoustic wave equation by the complex velocity corresponding to the specific viscoacoustic model (*Bland*, 1960). This allows us to check the accuracy of our finite difference schemes. In Figures 17 and 18 we compare seismograms using two different values of Q (Q=200 and Q=10,000) for the analytic solution and the O(4,4) scheme. Here we used an amplitude modulated 50 Hz signal as our initial condition. The two solutions are very close to each other. Since we already have showed that solutions from the O(2,4) and the O(4,4) scheme are close we have now showed that both the O(4,4) scheme and the O(2,4) scheme model viscoelasticity very accurately.

In Table 2 we display three pairs of relaxation mechanisms, obtained through the optimization algorithm described above, which yields an essentially constant Q of 200 between 20 and 80 Hz. In Figure 19 we compare a snapshot at 2.25 s and a Q of 200 using the O(2,4) scheme for one pair of relaxation mechanisms (Table 1) to an identical simulation, but for a case when we use three pairs of relaxation mechanisms (Table 2). The difference is small and hence it seems like the optimization of a constant Q is not as crucial as might have been anticipated in simulating viscoelastic wave propagation. For

practical purposes it might even be sufficient to use even fewer pairs of relaxation mechanisms than one per octave, as we stated as good rule of thumb. The explanation for this is found from the memory variables. In Figure 20 we have plotted the memory variables corresponding to the different relaxation mechanisms for the case where we used three pairs to model a constant Q. The magnitude of the curves varies dramatically. Hence, the main contribution to the viscoelastic modeling stems from the memory variable corresponding to the first set of relaxation mechanisms which intuitively seems to be reasonable. In Figure 21 we compare this memory variable to the memory variable in the simulation where we only used one pair of relaxation mechanisms. The two curves are very close to each other.

Finally, in Figure 22, we compare two snapshots (t=1.25 s and t=2.25 s) for a simulation using the three relaxation mechanisms listed in Table 2 and the O(4,4) code.

We found that the O(4,4) and the O(2,4) scheme model viscoelasticity sufficiently accurate and that the O(2,2) scheme hardly is of any use. The O(4,4) scheme is only slightly more accurate than the O(2,4) scheme for moderate Courant numbers and is also computationally more expensive. This is reflected through the number of calculations per grid-point. In 1-D, the number of calculations per grid-point (counting addition's, subtraction's, multiplication's, and division's equally), is about 75 for the O(4,4) scheme, 45 for the O(2,4) scheme, and 30 for the O(2,2) scheme. An advantage with the O(4,4) scheme is the ability of running simulations at high Courant numbers, i.e. fewer time steps are needed, which makes this scheme preferable in the 1-D case. To achieve high accuracy over a wide range of Courant numbers is also desirable when propagating waves through heterogeneous media where velocities may vary throughout the grid. However, when generalizing to the 2-D viscoelastic case, the O(4,4) scheme becomes extremely computationally expensive so that the advantages with the O(2,4) scheme are superior.

The pseudo O(4,4) scheme

The high operation count and the asymmetry of the dispersion relation for the O(4,4) scheme led us to derive an approximately O(4,4) scheme, which we chose to call a pseudo O(4,4) scheme. The viscoelastic constitutive relation is used directly instead of the equation system with memory variables. Equation (31) and (38) are,

$$\begin{cases} p_t = -\dot{\psi} * v_x \\ v_t = -\dfrac{1}{\rho} p_x \end{cases} \tag{47}$$

To create a compact scheme we must find the third order time derivatives of pressure and velocity expressed as spatial derivatives. From (47) these are found to be

$$\begin{cases} p_{ttt} = -\dfrac{1}{\rho}\dot{\psi} * (\dot{\psi} * v_{xxx}) \\ v_{ttt} = -\dfrac{1}{\rho^2}\dot{\psi} * p_{xxx} \end{cases} \tag{48}$$

These correction terms in a finite difference scheme yields,

$$\begin{cases} p_{\Delta t} = -\dot{\psi} * (v_{\Delta x} + \dfrac{\Delta t^2}{6\rho}\dot{\psi} * v_{\Delta x^3}) \\ v_{\Delta t} = -\dfrac{1}{\rho}p_{\Delta x} - \dfrac{\Delta t^2}{6\rho^2}\dot{\psi} * p_{\Delta x^3} \end{cases} \tag{49}$$

The Δ denotes finite difference approximations of the derivatives. The time derivative of the relaxation function contains one term multiplied with a Dirac delta function and one term multiplied with a unit step function. To derive the pseudo O(4,4) scheme the relaxation function, appearing in the convolutions with the third order spatial derivatives, is approximated with the term multiplied with the Dirac delta function. This approximation yields,

$$\begin{cases} p_{\Delta t} = -\dot{\psi} * (v_{\Delta x} + \dfrac{\Delta t^2}{6}\dfrac{M_R\tau_\varepsilon}{\rho\tau_\sigma} v_{\Delta x^3}) \\ v_{\Delta t} = -\dfrac{1}{\rho}(p_{\Delta x} - \dfrac{\Delta t^2}{6}\dfrac{M_R\tau_\varepsilon}{\rho\tau_\sigma} p_{\Delta x^3}) \end{cases} \tag{50}$$

Introduction of the memory variable yields the following system of equations, for one relaxation mechanism,

$$\begin{cases} p_{\Delta t} = -M_R(v_{\Delta x} - \dfrac{\Delta t^2}{6}\dfrac{M_R\tau_\varepsilon}{\rho\tau_\sigma}v_{\Delta x^3}) - r \\ r_{\Delta t} = -\dfrac{1}{\tau_\sigma}(r + (\dfrac{\tau_\varepsilon}{\tau_\sigma} - 1)(v_{\Delta x} - \dfrac{\Delta t^2}{6}\dfrac{M_R\tau_\varepsilon}{\rho\tau_\sigma}v_{\Delta x^3})) \\ v_{\Delta t} = -\dfrac{1}{\rho}(p_{\Delta x} - \dfrac{\Delta t^2}{6}\dfrac{M_R\tau_\varepsilon}{\rho\tau_\sigma}p_{\Delta x^3}) \end{cases} \tag{51}$$

Compared to the O(4,4) scheme fewer spatial derivatives have to be calculated in each time step. The accuracy and the dispersive properties of the pseudo O(4,4) scheme are close to those of the O(4,4) scheme, as is demonstrated in the Dispersion and Stability Analyses section. This is why we called this scheme the pseudo O(4,4) scheme.

CONVERGENCE TESTS

We performed a series of convergence tests for the different schemes to assure accuracy. Convergence was shown for the case of a propagating sinusoid, since an analytical solution for this problem is easy to obtain. We compared this to the numerical results from analog finite difference simulations and calculated the difference in the L2-sense.

Analytic solution for a single wavenumber

An analytic solution for a single wavenumber, k, is easy to find. By Fourier transforming (33), (37), and (38) in space we obtain a system of ordinary differential equations for a fixed k,

$$\dot{\underline{x}} = \underline{\underline{A}}\,\underline{x} \tag{52}$$

where

$$\underline{x} = \begin{pmatrix} p \\ r \\ v \end{pmatrix}$$

$$\underline{\underline{A}} = \begin{pmatrix} 0 & -1 & -ikM\tau_\varepsilon / \tau_\sigma \\ 0 & -1/\tau_\sigma & -ikM(\tau_\varepsilon / \tau_\sigma - 1)/\tau_\sigma \\ -ik/\rho & 0 & 0 \end{pmatrix}$$

This has the exponential solution which is obtained through the eigenvalues and corresponding eigenvectors of $\underline{\underline{A}}$. One eigenvalue is real and corresponds to an exponentially decaying solution. The other two eigenvalues are complex conjugates and correspond to propagating modes. By choosing one of the complex eigenvalues, the solution for a sinusoid propagating in one direction is found. The characteristic equation is a third order polynomial equation and the eigenvalues and eigenvectors must be determined numerically. We chose this analytic solution for convergence tests since these can be determined very accurately.

Test method

The convergence tests were done using a 40 Hz harmonic wave propagating in a medium with a velocity of 2000 m/s and Q=50. The initial conditions for the finite difference schemes were calculated using the analytic solution. Snapshots after 1.00 s from finite difference tests were compared to corresponding analytic solutions. The finite difference schemes were tested for 50, 25, 10, 5, and 2 grid-points/wavelength. The ratio $\Delta t/\Delta x$ was kept constant for the tests using the O(2,2) and O(4,4) schemes so that the error decreased equally in time and space. The ratio $\Delta t/(\Delta x)^2$ was kept constant when testing the O(2,4) scheme for the same reason. This results in a O(4,4) behavior for the O(2,4) scheme during the convergence tests. The O(2,4) scheme was also tested for a constant Courant number of 0.4. The tests were performed at a Courant number of 0.8 for the O(2,2) and O(4,4) schemes. The simulation parameters are listed in Table 3.

Results of the convergence tests

The difference between the analytical solution and the results using the O(2,2) scheme is displayed in Figure 23. As expected, the best fit line for the logarithm of the L2-error as a function of the number of grid-points/wavelength has a slope close to -2 (-2.24). The surprisingly close fit for the 10 grid-points/wavelength test is due to the periodicity of the analytic solution. The numerical solution is actually numerically dispersed a full wavelength, which results in the apparent close fit. Snapshots for different numbers of grid-points/wavelength at 1.00 s are plotted in Figures 24 and 25. The result for the O(2,4) scheme (non-constant Courant number) is displayed in Figure 26. The best fit line for the logarithmic L2-error has a slope of -5.13 which is close to the predicted O(4,4) behavior (-4). Snapshots at 1.00 s are plotted in Figures 27 and 28. The result for the O(2,4) scheme using a constant Courant number is shown in Figure 29. The best fit line has a slope of -1.54. Snapshots at 1.00 s are plotted in Figures 30 and 31. The result of the O(4,4) scheme tests is presented in Figure 32. The best fit line has a slope of -4.23, which is close to the expected (theoretically it should be -4). The snapshots at 1.00 s are plotted in Figures 33 and 34. The results for 2 and 5 grid-points/wavelength are poor for all the schemes. We conclude that our schemes converge to the analytical solution as predicted by theory.

DISPERSION AND STABILITY ANALYSES

Dispersion and stability analyses of finite difference schemes reveal behavior that otherwise may be obscure or difficult to understand. Viscoelastic media are intrinsically dispersive. The phase velocity increases with frequency as shown by *Futterman* [1962] and *Wuenschel* [1965]. This is evident in Figure 36. In addition to this finite difference methods for wave propagation introduce numerical dispersion due to the time and space discretization. Hence, we are studying dispersive media with dispersive methods. We must therefore assure that the influence of numerical dispersion is minimal.

We have already made some observations of dispersion and stability issues above under Implementation and Numerical Experiments. A more thoroughly study is however necessary in order to gain deeper understanding and to confirm our initial conclusions. For simplicity, in the following we will consider the case when we have one memory variable. The discrete finite difference schemes are Fourier (discrete) transformed to the frequency-wavenumber domain, where they are compared to the analytical dispersion of the viscoelastic medium. The numerical dispersion originates from two places in our schemes. First, unwanted dispersion might be introduced in the equation governing the memory variable, r. More familiar numerical dispersion is introduced through the part of the scheme governing the wave propagation. The dispersion relation for the viscoelastic schemes must be solved numerically, most convenient through an iterative method. Stability criteria were investigated using von Neumann analysis. The numerical scheme is Fourier transformed in space and Z transformed in time. The roots of the emerging polynomial equation yield information about the stability of the scheme. If the absolute value of all roots is less than one the scheme is stable.

Dispersion analysis

The discrete dispersion relations for the O(2,2) and O(2,4) schemes are the product of a term responsible for wave-propagation and another term responsible for viscoelastic damping and dispersion, originating from the memory variable equation. The relation for the O(4,4) scheme does not have the same form. We will start by investigating the equation for the memory variable, r, since the new part of the full dispersion relation is coming directly from that equation.

A conventional leapfrog scheme was used to update the stress and velocity equations. Since a dominating part of the numerical dispersion originate from the wave propagating part, O(2,4) and O(4,4) schemes were studied in addition to the O(2,2)

scheme. The O(2,2) and O(2,4) schemes will be covered in the same paragraph, since these have similar dispersion relations, in contrast to the O(4,4) scheme which is a compact scheme.

Due to the dependence on Q and the complicated analytical dispersion relations, it is not possible to come up with a simple rule of thumb for how many grid-points per wavelength that is needed in a simulation to assure sufficiently low effects from numerical dispersion.

1. The memory variable equation.

We chose to use an unconditionally stable scheme for the memory variable, since there is a possibility that for some models, the stability criteria might be violated for schemes like Euler forward and Adams-Bashforths method. To gain higher accuracy we chose the Crank-Nicholson above the Euler backward scheme. The damping of the two schemes are compared in Figure 35, where, not surprisingly, the Euler backward scheme does not yield enough damping at high frequencies. The dispersion relation for the Crank-Nicholson scheme is,

$$\frac{\omega^2}{\omega_0^2} = 1 + \left(\frac{\tau_\varepsilon}{\tau_\sigma} - 1\right)\frac{2\sin(\omega\Delta t/2)}{2\sin(\omega\Delta t/2) + \frac{i\Delta t}{\tau_\sigma}\cos(\omega\Delta t/2)} \tag{53}$$

The analytic expression for the dispersion can be found by taking the limit of infinitely small time steps $\Delta t \to 0$.

$$\frac{\omega^2}{\omega_0^2} = 1 + \left(\frac{\tau_\varepsilon}{\tau_\sigma} - 1\right)\frac{i\omega}{i\omega - \frac{1}{\tau_\sigma}} \tag{54}$$

where ω_0 is the angular frequency of a wave propagating in an elastic medium.

2. The O(2,2) and O(2,4) schemes.

The dispersion relations for the O(2,2) and O(2,4) schemes may be written as a factor for the numerical dispersion originating from an elastic scheme multiplied with a factor for the numerical dispersion from the equation for r. The dispersion relations for the elastic O(2,2) and O(2,4) schemes are,

$$\sin^2(\omega_0) = k^2 \sin^2(k_0), \text{ for the O(2,2)-scheme,} \tag{55}$$

and

$$\sin^2(\omega_0) = k^2 \sin^2(k_0)\left[\frac{4-\cos(k_0)}{3}\right]^2, \text{ for the O(2,4)-scheme,} \tag{56}$$

where $\omega_0 = \omega\Delta t$, $k_0 = k_w\Delta x$, and $k = c\,\Delta t/\Delta x$ is the Courant number. Here c is the velocity of the medium and k_w is the wavenumber. The dispersion relations for the viscoelastic schemes turns out to be as simple as relation (53) multiplied with either of relation (55) or (56), respectively. Hence, we obtain,

$$\sin^2(\omega_0) = k^2 \sin^2(k_0)(1+F(\omega_0, \Delta t, \tau_\sigma, \tau_\varepsilon)) \tag{57}$$

$$\sin^2(\omega_0) = k^2 \sin^2(k_0)\left[\frac{4-\cos(k_0)}{3}\right]^2 (1+F(\omega_0, \Delta t, \tau_\sigma, \tau_\varepsilon)) \tag{58}$$

where $F = \left(\omega^2/\omega_0^2\right) - 1$ is obtained from (53). Equations (57) and (58) yield that the maximum Courant number for a stable scheme is lowered, since (1+F) always is greater than 1. The stability limit (i.e. the maximum Courant number) is as a matter of fact decreased by approximately a factor 1/(1+1/Q), since F is almost proportional to 1/Q. The highest velocity in the medium is found at infinite frequency, $c_{\max} = \sqrt{\tau_\varepsilon M_r/\tau_\sigma \rho}$. Therefore, to determine the maximum Courant number this velocity has to be used. The dispersion curves for the O(2,2) and O(2,4) schemes are plotted in Figures 36 and 37. The damping curves for the schemes are plotted in Figures 38 and 39. The viscoelastic dispersion curves demonstrate the same characteristics as their elastic analogs. To model the velocity in the medium with sufficient accuracy, a large number of grid-points per wavelength is needed for the O(2,2) scheme. The velocity is always modeled too low. The O(2,4) scheme overestimates the velocity for high Courant numbers but does not, on the other hand, need as many grid-points per wavelength to accurately model the velocity. At high wavenumbers, the damping is underestimated by the O(2,2) scheme, whereas the O(2,4) underestimates the damping at small Courant numbers and overestimates the damping at large Courant numbers.

3. The O(4,4) scheme.

A higher order scheme as the O(4,4) scheme is useful since it models wave propagation accurately for a wide range of Courant numbers. This is an important property in simulations in heterogeneous media, since one often encounters large velocity variations within the area of simulation. The compact scheme is constructed by adding a correction term, to the O(2,4) scheme consisting of spatial derivatives, as was described above. Only the equations for stress and velocity are corrected for higher time derivatives. Hence, the scheme used for the memory variable equation is still Crank-Nicholson. Since the correction is not done through higher order time approximations the dispersion relation is no longer the product of a wave propagation term and a relation from the memory variable equation. The dispersion relation weights the remainders of the O(2,4) scheme more than the correction terms. For low Q, this results in a behavior in between the O(2,4) and O(4,4) schemes. The dispersion relation for the O(4,4) compact scheme is,

$$\sin^2(\omega_0) = \frac{1}{1+\frac{i}{6}\eta k^2 \tau_l (f_1 G\eta + \sin(k_0))\frac{\sin(k_0)}{\sin(\omega_0)}} \times$$

$$\times\left[f_1 f_4 (1+F) + \frac{1}{3}k^2 f_3 f_4 (1+\tau_l)^2 - \frac{1}{6}k^2 \tau_l (1+\tau_l)\eta G f_1 f_4 \sin^2(k_0) + \frac{1}{6}\eta^2 \tau_l f_4 (f_1 \eta G + \sin(k_0)\right] +$$

$$+\frac{i}{6}k^2 \tau_l \eta \sin^2(k_0)\sin(\omega_0) \tag{59}$$

where

$$F = \tau_l (1+\eta G)$$

$$G = \frac{1}{2}\frac{\cos(\omega_0/2)}{i\sin(\omega_0/2) - \frac{\Delta t}{2\tau_\sigma}\cos(\omega_0/2)}$$

$$f_4 = k^2 f_1 + \frac{1}{3}k^4 (1+\tau_l) f_3$$

$$f_1 = \sin(k_0)\frac{4-\cos(k_0)}{3}$$

$$f_3 = \sin(k_0)(\cos(k_0)-1)$$

$$\tau_l = \frac{\tau_\varepsilon}{\tau_\sigma} - 1$$

$$\eta = \frac{\Delta t}{\tau_\sigma}$$

At the elastic limit ($\tau_l \rightarrow 0$) the expression collapses to the elastic expression. This is,

$$\sin^2(\omega_0) = k^2(f_1 + \frac{1}{3}k^2 f_3)^2 \tag{60}$$

which is equivalent to,

$$\sin^2(\omega_0) = k^2 \sin^2(k_0)\left(\frac{4-\cos(k_0)+k^2(\cos(k_0)-1)}{3}\right)^2 \tag{61}$$

For the acoustic scheme the stability limit is k=1.0, and, as mentioned above, slightly lower for the viscoelastic scheme. Equation (59), yield that the term (1+F) weights f_1 terms more than f_3 terms. The f_1 terms correspond to the spatial relation for the O(2,4) scheme while the f_3 terms correspond to the correction terms in the O(4,4) compact scheme. For low Q and relatively large values of F, this leads to a behavior similar to that for the O(2,4) scheme. The dispersion curves for the O(4,4) scheme are plotted in Figure 40. The fit is very good up to 10 grid-points/wavelength. The difference between the theoretical and the numerical curve is less than 1%. The damping curves for the O(4,4) scheme are displayed in Figure 41. The damping is overestimated for large wave and Courant numbers.

The dispersion relation for the pseudo O(4,4) scheme is, as for the O(2,2) and O(2,4) schemes, almost the dispersion relation for an elastic scheme multiplied with a term from the memory variable equation. This is,

$$\sin^2(\omega_0) = k^2(f_1 + \frac{\tau_\varepsilon}{3\tau_\sigma}k^2 f_3)^2(1+\tau_l(1+\eta G)) \tag{62}$$

The dispersion curves for the O(4,4) and pseudo O(4,4) schemes are compared in Figure 42 and the damping curves are compared in Figure 43. The dispersion curves are virtually the same and the damping behavior of the pseudo O(4,4) scheme is actually slightly better than for the O(4,4) scheme. Since F and G in all above dispersion relations depend on ω_0 in a sometimes quite complex way, ω, as a function of k_w, is found through iteration. The value $\omega=ck_w$ serves as a good initial value in this procedure.

Stability analysis

We used von Neumann analysis to investigate stability for the O(2,2), O(2,4), and the O(4,4) schemes. This method consists of Fourier transforming the spatial difference approximations of the finite difference scheme. This yields a difference equation for each wavenumber. If the absolute values of the solutions to the difference equation are less than one the scheme is stable. The schemes were found to be intrinsically unstable. The poles of the modal equation, which have a negative real part, are shifted outside the unit circle, whereas the poles with positive real part are shifted inside. This should be regarded in contrast to a corresponding elastic scheme, were all the poles are on the unit circle. In Figure 44 we have plotted the poles for the O(2,4) scheme. The absolute values of the poles with negative real part are plotted in Figure 45. The instability remains, even if the spatial derivatives are computed with spectral accuracy. The poles for this pseudo-spectral scheme are plotted in Figure 46. Here, the poles with positive real part are found outside the unit circle. This is shown in Figure 47. Increasing the Courant number or decreasing Q increases the absolute values of the poles outside the unit circle. As a consequence, the effect of the instability is stronger in a simulation in these cases. A simple solution to overcome this problem is to add a dissipative term in one or both of the equations for the pressure and velocity. The term can be sufficiently small so that it has no effect on the accuracy. Equation (63) shows an example how to add the dissipative term in the equation for pressure.

$$p_t = -\frac{\tau_\varepsilon}{\tau_\sigma} v_x - r + \kappa p_{xx} \tag{63}$$

where the second derivative is approximated by,

$$p_{xx}(m\Delta x) \approx \frac{p_{m+1} + p_{m-1} - 2p_m}{\Delta x^2} \tag{64}$$

A spatial second derivative of the pressure is added to the equation to yield a dissipative (heat-equation) behavior. The parameter $\kappa(x)$ must be adjusted in accordance with the material properties of every grid-point. κ has to be large enough to yield a stable scheme and still not affect the modeling of viscoelastic waves. The second derivative must be taken in the (n-1):th time step in (39) to yield the desired stabilizing effect *Kreiss and Oliger* [1973]. The modal equation gives a few hints how to scale κ to achieve a stable scheme. Presently the size of κ is determined by a formula derived from the modal equation and through trial and error. Figure 48 demonstrates a case where a dissipative term has been added to the equation for the stress in the O(2,4) scheme. The term controls the instability as is illustrated in Figure 49, where the absolute values of the poles are less than or equal to one. The effect of the dissipative term on dispersion and damping is illustrated for the O(2,4) scheme in Figures 50 and 51, where these are plotted with and without the stability controlling dissipative term. At high wavenumbers and at the peak of the damping curve, the damping is slightly increased by the dissipative term. The dispersion curves are practically identical.

We found the schemes to model the viscoelastic equations well. The propagation of viscoelastic waves appears to be the most crucial issue, since the Crank-Nicholson scheme is sufficiently accurate for the memory variable equation. The use of leapfrog time stepping schemes seems to result in intrinsically unstable schemes. Fortunately, this problem is easy to overcome by adding a sufficiently small dissipative term which does not affect the solution. We are now ready to generalize our results to 2-D.

2-D VISCOELASTIC MODELING

The theory derived for the 1-D case above is easy to generalize to 2-D and the results from the 1-D experiments are applicable also in the 2-D case. In the 2-D viscoelastic case of 1 relaxation mechanism both for the P-waves and the SV-waves the analog to (33), (37), and (38) is a system of 9 first order linear partial differential equations. This is,

$$
\begin{cases}
\dfrac{\partial \sigma_{xy}}{\partial t} = \mu_0 \dfrac{\tau_\varepsilon^s}{\tau_\sigma^s}\left(\dfrac{\partial v_x}{\partial y} + \dfrac{\partial v_y}{\partial x}\right) + r \\[2ex]
\dfrac{\partial \sigma_{xx}}{\partial t} = \left(\pi_0 \dfrac{\tau_\varepsilon^p}{\tau_\sigma^p} - 2\mu_0 \dfrac{\tau_\varepsilon^s}{\tau_\sigma^s}\right)\dfrac{\partial v_y}{\partial y} + \pi_0 \dfrac{\tau_\varepsilon^p}{\tau_\sigma^p}\dfrac{\partial v_x}{\partial x} + p - 2q_1 \\[2ex]
\dfrac{\partial \sigma_{yy}}{\partial t} = \left(\pi_0 \dfrac{\tau_\varepsilon^p}{\tau_\sigma^p} - 2\mu_0 \dfrac{\tau_\varepsilon^s}{\tau_\sigma^s}\right)\dfrac{\partial v_x}{\partial x} + \pi_0 \dfrac{\tau_\varepsilon^p}{\tau_\sigma^p}\dfrac{\partial v_y}{\partial y} + p - 2q_2 \\[2ex]
\dfrac{\partial v_x}{\partial t} = \dfrac{1}{\rho}\left(\dfrac{\partial \sigma_{xx}}{\partial x} + \dfrac{\partial \sigma_{xy}}{\partial y}\right) \\[2ex]
\dfrac{\partial v_y}{\partial t} = \dfrac{1}{\rho}\left(\dfrac{\partial \sigma_{xy}}{\partial x} + \dfrac{\partial \sigma_{yy}}{\partial y}\right) \\[2ex]
\dfrac{\partial p}{\partial t} = -\dfrac{1}{\tau_\sigma^p} p + \pi_0 \dfrac{1}{\tau_\sigma^p}\left(1 - \dfrac{\tau_\varepsilon^p}{\tau_\sigma^p}\right)\left(\dfrac{\partial v_x}{\partial x} + \dfrac{\partial v_y}{\partial y}\right) \\[2ex]
\dfrac{\partial r}{\partial t} = -\dfrac{1}{\tau_\sigma^s} r + \mu_0 \dfrac{1}{\tau_\sigma^s}\left(1 - \dfrac{\tau_\varepsilon^s}{\tau_\sigma^s}\right)\left(\dfrac{\partial v_x}{\partial y} + \dfrac{\partial v_y}{\partial x}\right) \\[2ex]
\dfrac{\partial q_1}{\partial t} = -\dfrac{1}{\tau_\sigma^s} q_1 + \mu_0 \dfrac{1}{\tau_\sigma^s}\left(1 - \dfrac{\tau_\varepsilon^s}{\tau_\sigma^s}\right)\dfrac{\partial v_y}{\partial y} \\[2ex]
\dfrac{\partial q_2}{\partial t} = -\dfrac{1}{\tau_\sigma^s} q_2 + \mu_0 \dfrac{1}{\tau_\sigma^s}\left(1 - \dfrac{\tau_\varepsilon^s}{\tau_\sigma^s}\right)\dfrac{\partial v_x}{\partial x}
\end{cases}
\tag{65}
$$

σ_{ij} denotes the ij:th component of the symmetric stress tensor.

v_i denotes the i:th component of the velocity.

p, r, q_1, q_2 are the memory-variables (4 are needed for the simplest 2-D case with one relaxation mechanism each for the P-waves and the SV-waves.

τ_ε^p, τ_σ^p are the strain and stress relaxation times for the P-waves.

τ_ε^s, τ_σ^s are the strain and stress relaxation times for the SV-waves.

μ_0 is the relaxation modulus corresponding to SV-waves and is analog to the Lamé constant μ in the elastic case.

π_0 is the relaxation modulus corresponding to P-waves and is analog to the sum of the Lamé constant λ and 2 times the Lamé constant μ.

Here we have defined the relaxation functions so that these correspond to P- and SV-waves respectively. We are therefore able to derive the relaxation mechanisms directly from constraints on the quality factors for the P- and SV-waves separately, analogous to what was done in the 1-D case described above. This is why a relaxation modulus, π_0, not corresponding to a single Lamé constant is introduced.

In the simplest 1-D case when only one pair of relaxation mechanisms was used only one memory-variable was needed. In the 2-D case we need 4 memory-variables in the simplest case corresponding to one pair of relaxation mechanisms each for the P- and the SV-waves. This stems from the fact that different convolution terms arises in the equations governing the stress components.

Stability and accuracy issues are treated as was described above. The scheme has the same properties as the 1-D O(2,4) scheme. Leap-frog in time and 4:th order central differences in space are used for the equations governing velocity and stress components. Crank-Nicholson in time and 4:th order central differences in space are used for the equations governing the memory variables. The scheme is intrinsically unstable because it yields the 1-D O(2,4) scheme when applied to plane waves in the coordinate directions, which was shown to be unstable above. In most cases the instability appears to be very weak and the scheme can be used directly on the system of equations in (65).

The dispersion relation for the 2-D viscoelastic scheme has two solutions, one corresponding to P-wave velocity and one corresponding to S-wave velocity. This yields simple modeling of fluid-solid boundaries, since there is no coupling between P-waves and S-waves in a homogeneous medium. Dissipative terms have to be introduced, as shown above, in all equations for stress and velocity to yield a conditionally stable scheme with uncoupled P-wave and S-wave velocities, when this is necessary. The

stabilizing term is the same for both P-waves and S-waves, though. This means that if the S-waves are modeled in such a way that strong dissipation has to be introduced to keep the scheme stable, that the modeling of P-waves might be affected.

We believe that our viscoelastic code has applications in a diversity of fields. To demonstrate this we will next show two different marine environments, one continental shelf and one deep sea, where the negligence of anelastic effects seriously limits realistic analyses. In these cases the instability does not pose any problems and no stabilizing terms were therefore added. Close to the mid-oceanic ridges the seafloor is lineated parallel to the ridges (*Goff and Jordan*, 1988). The geometries of the environments in the two examples hence have symmetric characters along one axis, and a 2-D study is therefore suitable for sufficiently realistic analyses.

Numerical example 1. Realistic deep-sea seafloor scattering.

In mono-static seafloor scattering measurements the reverberation of acoustic energy of low incidence grazing angle on the seafloor is of particular interest. Fluid saturated and porous media, such as sedimented seafloor, are highly anelastic. This behavior can be well described by a viscoelastic model. In this example we show the importance of including viscoelastic effects in such a scattering simulation. The seafloor and the parameters used are typical for young (10-50 m.y. old) seafloor close to the northern mid-Atlantic ridge. The largest scale of the seafloor obey an exponential decaying solution of the heat equation as a function of the distance to the mid oceanic ridges. When modeling the seafloor, larger features may be regarded as deterministic, while a stochastic model may be applied to smaller features. *Goff and Jordan* [1988] present a new way of analyzing the stochastic component of the seafloor, assuming it is of fractal character. *Goff et al.* [1992] describe a method of generating realistic stochastic seafloor profiles with sediments added. We used a profile generated by them from data from the proximity of the mid-Atlantic ridge. The full length seafloor profile is 20 km long and is discretized down to 1 m. We chose a 1 km segment to use in our finite difference simulations. This is enclosed in Figure 52. We used material properties appropriate for seafloor of this age in the Atlantic ocean (e.g. *Hamilton et al.*, 1982). The sediments are characterized by a low Q (30-50 both for pressure and shear waves), pressure wave velocities close to that in water, low shear wave velocities (a few 100 m/s), and about 70% higher densities than that of water. This is typical for fluid saturated unconsolidated sediments. The material properties are listed in Table 4.

Our initial condition was a tapered amplitude modulated plane wave incident on the seafloor with 10 degrees grazing angle. The wave has a central frequency of 140 Hz and a bandwidth of approximately 50 Hz. The particular wave-form is similar to wave-forms used in many sonar systems. Since the bandwidth occupies less than one octave only one pair of relaxation mechanisms for each P- and SV-waves is needed. The plane wave was inserted in the water column in the grid as an initial condition. In the first time step the desired wave-front was chosen. The second time step was simply calculated from the first time step using D'Alemberts formula, the angle of incidence, and the velocity in the water. In Figure 53a we show the P-wave energy snapshot for the initial condition (the S-wave energy is of course 0 everywhere).

We chose a grid-spacing of 1 m in both spatial directions. The grid was 1100 m times 315 m with an additional 80 m wide frame for the absorbing boundary added around this grid, acting as a sponge filter. In this frame we used a very low Q (Q=6 both for P- and S-waves) and tuned the Lamé constants so that the dispersion relation yielded a constant velocity over the transition from the grid right inside the frame to its interior for the center frequency. Hence we were able to minimize reflections from impedance contrasts. Below we will present a suite of P- and SV-wave energy snapshots . We have cut away the absorbing frame in all of these. The time step was 0.1 ms which leads to a maximum Courant number of 0.26 which is well below the stability criterion and in accordance with the accuracy observations for the O(2,4) scheme. It should be emphasized that if we sacrifice accuracy it would be possible to run simulations at a significantly higher Courant number if a radiating boundary condition would be used instead of a low Q frame (*Higdon*, 1991), since the regions of the grid with the highest Courant number are within the absorbing frame. The number of grid-points per wavelength varies of course throughout the grid both with P- and S-wave velocities. The lowest number of grid-points per wavelength occurs for SV-waves in the sediments where we are down to 4, while it is 19 for the P-waves in the basement. We have done convergence tests at the particular material properties for denser sampled grids to confirm that the field is not under-sampled.

One has to keep in mind that a viscoelastic model not only introduce attenuative properties to the materials but also dispersive effects of realistic character (*Futterman*, 1962). In this example we can therefore expect to observe two different effects on the scattered field when comparing elastic and a viscoelastic simulations. Both attenuation of wave energy and changes in impedance's due to this dispersion will affect the scattered field. The velocities listed in Table 4 are the elastic velocities or the velocities for the 0 Hz limit in the viscoelastic case. At 140 Hz and these values of Q the velocity increases

about 1%. For instance, in the viscoelastic case at 140 Hz the velocity for the P-waves in the sediment layer increases from 1.54 to 1.55 km/s. We can expect the effects from these changes to be smaller than the effects from the attenuation, although these might be significant if we are close to transition from pre- to post-critical reflection.

In Figures 53a through g we show a series of energy snapshots. Figure 53a shows the initial condition. We present snapshots for P- and SV-wave energies at 0.3 s and 0.5 s in Figures 53b through e. At 0.3 s there is a strong headwave propagating through the basement ahead of the wave-front. A surfacewave develops in the interface between sediments and the basement. At 0.5 s this, as well as the SV-wave energy in the sediments, has been attenuated due to the viscoelastic properties of the seafloor. In Figures 53f and g we show the P-wave energy snapshot at 0.5 s for an elastic sedimented seafloor and for a bare seafloor. The surfacewave is much stronger in the elastic case than in the viscoelastic case. Hence, the viscoelastic character of the sediments leads to attenuation of the surfacewave, an important source of backscattered energy in low frequency elastic scattering simulations (e.g. *Dougherty and Stephen*, 1988). The leftmost crest shadows the trough in the bare seafloor experiment, while the sediment layer traps energy when an elastic sediment cover is present. Therefore the surfacewave is stronger when elastic sediments are present compared to the bare seafloor.

We have done several different experiments with numerous seafloor profiles which all show that anelastic properties play an important role in this kind of seafloor scattering experiments. It is beyond the scope of this paper to go into the details of these investigations but differences up to 15 dB between elastic and viscoelastic simulations are observed in the back-scattered direction.

Numerical example 2. Wave propagation in sediments in an incised valley on the continental shelf.

Common features on the continental shelf along the U. S. Gulf coast are incised valleys created by a variety of fluvial systems (ancient meandering rivers and deltas, etc.). During retrogradation such systems are back-filled with clastic sediments. These sediment fills are highly anelastic and moreover the properties changes with time as these are compressed by younger deposits. We chose a typical cross-section of such a system for a numerical simulation. This is enclosed in Figure 54 and the material properties are listed in Table 5. We chose not to model the water surface since multiple reflections from this would complicate a simple analysis of the differences between a viscoelastic and an

elastic simulation. Hence, we apply the same type of absorbing boundaries all around the grid as was used in the first example.

As a source we used an 80 Hz Ricker wavelet modeling an air-gun impulse. The 80 Hz Ricker wavelet is symmetric with respect to its radius and was inserted as a pressure pulse in the water column, constant in the first two time steps. A P-wave energy snapshot of this is enclosed in Figure 55. The Ricker wavelet spans over 3-4 octaves, and hence 3 to 4 relaxation mechanisms should be applied in order to assure a constant Q as a function of frequency over the full frequency interval to be in accordance with the algorithm discussed above. The fewer relaxation mechanisms that are used the less constant Q within the desired interval. It should however be emphasized that constant Q not is a universal truth for all earth materials but deviations from this rule of thumb is of course possible. The purpose of this example is to qualitatively demonstrate the difference between an elastic and viscoelastic simulation and hence we chose to use only one set of relaxation mechanisms. This leads to a very close to constant Q within 60 Hz to 120 Hz, which is where the main energy content of this Ricker wavelet is, and a fairly good approximation within the rest of the Ricker wavelet frequency band. This serves our purposes more than well. To further justify our decision we refer to the 1-D experiment discussed above, which is illustrated in Figure 19, where we compared snapshots for a Ricker wavelet propagating in media characterized by 1 and 3 relaxation mechanisms, respectively.

The model is 190 m in the vertical direction of which the upper 70 m are water (see Figure 54), and 640 m in the horizontal direction. We have also in this example cut out the absorbing frame in all energy snapshots in Figure 55, Figures 56a through h, and Figures 57a through h. 1 m grid-spacing was used in both spatial directions and the time step was 0.15 ms which leads to a maximum Courant number of 0.33 which is well below the stability limit for our scheme.

In Figures 56a through h we show P- and SV-wave energy snapshots of a viscoelastic simulation using the material properties in Table 5. In Figures 57 a through h we show snapshots from the analog experiment in the elastic limit where we have set all Q to 10,000 in Table 5. The SV-wave energy snapshots have been amplified three times more compared to the P-wave energy snapshots. In Figures 56a and b, and 57a and b, we show the P- and SV-wave energy snapshots at 0.05 s for the viscoelastic and the elastic simulation respectively. In the snapshots for the P-wave energy, reflections from the different sediment layers are clearly visible. There is a strong conversion of P-waves to SV-waves at the different boundaries. The initiation of SV-waves are found where the P-wave intersect the boundaries of the model. This gives the impression that the SV-waves

are following the boundaries between the different sediment layers. This effect is not equally prominent at the water-solid boundary. There is hardly any difference between the elastic and viscoelastic case. The energy from the waves is also well absorbed by the boundaries (no reflections are visible). Figures 56c and 57c are snapshots of the P-wave energy after 0.1 s of propagation, for the viscoelastic respectively the elastic model. The P-wave in the viscoelastic medium is slightly diminished compared to the P-wave in the elastic medium. The conversion of P-waves to SV-waves along the sediment boundaries continues as can be seen in Figures 56d and 57d, which are snapshots of the SV-wave energy at 0.1 s for the viscoelastic respectively the elastic medium. The SV-waves in the viscoelastic medium have clearly smaller amplitudes compared to the SV-waves in the elastic medium. Details are also more difficult to observe in the snapshot from the viscoelastic simulation. In Figures 56e and f, and 57e and f, we show the P- and SV-wave energy snapshots at 0.2 s. The amplitude of the P-headwave is significantly reduced from propagating through the viscoelastic sediments. The difference between the viscoelastic and the elastic simulations is even more striking in the SV-wave energy snapshots. Moreover, conversions from SV-to P-waves at the layer boundaries induce P-wave energy in the water column. This process is much weaker in the viscoelastic case compared to the elastic case (this is not clearly visible in the snapshots due to an amplitude threshold in the plotting program). In Figures 56g and h, and 57g and h, we show the P- and SV-wave energy snapshots at 0.3 s. From these plots it is evident that wave propagation in a medium like this is of viscoelastic nature. There is hardly any energy left in the viscoelastic simulation compared to the elastic simulation.

CONCLUSIONS

Viscoelasticity provides a powerful tool for modeling real earth media. The viscoelastic relaxation function can easily be tuned to resemble the attenuative and dispersive effects that real earth materials have on propagating waves. We conclude that it is fully possible to use finite difference methods to simulate wave propagation through dispersive and attenuative viscoelastic media. It is easy to choose simulation accuracy and the code is highly portable. We have done viscoelastic wave propagation simulations using our schemes and have achieved high performance on several different computers such as, the Stardent 2000, different SUN computers, the Cray YMP, and the hypercube i860.

The different schemes clearly converge towards the exact solution consistent with predicted accuracy. There are two different instabilities in the schemes. First there is the instability from the finite difference approximation of the elastic wave equation. This is possible to control and the stability limit is given in terms of the Courant number. The other instability is new and makes the schemes intrinsically unstable. For moderate simulation parameters and Q values, this tend not to be a problem. Generally the scheme is more unstable the lower Q is. An important observation is that low values of Q tend to occur where the velocity is low. Since the highest velocities in a model set the limit for the Courant number, the Courant number in low velocity zones will be relatively small and therefore also less unstable. In other cases, the instability can be controlled by adding a sufficiently small dissipative term which does not affect the accuracy of the scheme.

The O(2,4) scheme is less computationally expensive while the O(4,4) scheme has a 30% higher stability limit and is exact over a significantly larger Courant number interval, which is important in wave propagation simulations in heterogeneous media. Despite the advantages of the O(4,4) scheme, the computational expense in 2-D makes it impractical.

Through our numerical examples we have shown that anelastic effects must be considered in many situations and that our scheme accurately models wave propagation through viscoelastic media. Our examples also prove that viscoelastic simulations using finite difference grids of practical sizes are possible.

The code has primarily been developed to provide a useful tool for scattering and inversion projects. At present we are doing 2-D viscoelastic seafloor scattering experiments as well as Q-inversion studies.

ACKNOWLEDGMENTS

This work was supported by ONR grants N00014-89J-3015 and N00014-89J-1115. We wish to express our sincere gratitude to Dr. Alan R. Levander of the Department of Geology & Geophysics at Rice University for support and useful input during the work. During the development of the code we used the Cray YMP at San Diego Super Computer Center, the Stardent 2000, and the hypercube i860 at Rice University.

We also wish to thank Dr. John A. Goff of Woods Hole Oceanographic Institution, Dr. Thomas H. Jordan, and Helen F. Webb of the Department of Earth, Atmospheric, and Planetary Sciences at Massachusetts Institute of Technology for providing us with realistic synthetic seafloor profiles.

REFERENCES

Bland, D. R., 1960, The theory of linear viscoelasticity: Pergamon Press.

Bourbie, T., Coussy, O., Zinzner, B., 1987, Acoustics of porous media: Gulf Publishing Company.

Carcione, J. M., Kosloff, D., Kosloff, R., 1988, Wave propagation simulation in a linear viscoacoustic medium: Geophysical Journal, **93**, 393-407.

Christensen, R. M., 1982, Theory of viscoelasticity - An introduction: Academic Press, Inc.

Dablain, M. A., 1986, The application of high-order differencing to the scalar wave equation: Geophysics, **51**, 127-139.

Day, S. M., Minster, J. B., 1984, Numerical simmulation of attenuated wavefields using a Padé approximant method: Geophys. J. R. astr. Soc., **78**, 105-118.

Dougherty, M. E., Stephen, R. A., 1988, Seismic energy partitioning and scattering in laterally heterogeneous ocean crust: PAGEOPH, **128**, 195-229.

Futterman, W. I., 1962, Dispersive body waves: Journal of Geophysical Research, **67**, 5279-5291.

Goff, J. A., Jordan, T. H., 1988, Stochastic modeling of seafloor morphology: Inversion of sea beam data for second-order statistics: JGR, **93**, 13589-13608.

Goff, J. A., Webb, H. F., Jordan, T. H., 1992, Stochastic interpolation of a wide-beam bathymetric profile within the ONR-ARSRP acoustic reverberation corridor: ARSRP Technical Report 2.

Gurtin, M. E., 1981, An introduction to continuum mechanics: Academic Press, Inc.

Hamilton, E. L., Bachman, R. T., Berger, W. H., Johnson, T. C., Mayer, L. A., 1982, Acoustic and related properties of calcareous deep-sea sediments: Journal of Sedimentary Petrology, **52**, 733-753.

Higdon, R. L., 1991, Absorbing boundary conditions for elastic waves: Geophysics, **56**, 231-241.

Kreiss, H. O., Oliger, J., 1973, Methods for the approximate solution of time dependent problems: Garp publications series No. 10.

Levander, A. R., 1988, Fourth-order finite-difference P-SV seismograms: Geophysics, **53**, 1425-1436.

Liu, H. P., Anderson, D. L., Kanamori, H., 1976, Velocity dispersion due to anelasticity; implications for seismology and mantle composition: Geophys. J. Roy. Astr. Soc., **47**, 41-58.

Pipkin, A. C., 1986, Lectures on viscoelasticity theory: Springer Verlag.

Wuenschel, P. C., 1965, Dispersive body waves - an experimental study: Geophysics, **30**, 539-551.

Q	$\tau_\varepsilon(ms)$	$\tau_\sigma(ms)$
50	4.33	4.16
100	4.287	4.202
200	4.2654	4.2230
1,000	4.2484	4.2399
10,000	4.2446	4.2437

Table 1. The relaxation mechanisms used in the experiments to simmulate the Q in the left most column.

Pair	$\tau_\varepsilon(ms)$	$\tau_\sigma(ms)$
1	8.0186	7.9578
2	1.1565	1.1488
3	0.51773	0.51705

Table 2. Optimized relaxation mechanisms to yield a constant q of 200 between 20 and 80 Hz.

grid-points/wavelength	Δx (m)	Δt (ms)
50	1	0.40
25	2	0.80
10	5	2.00
5	10	4.00
2	25	10.0

Table 3a. Simulation parameters for the O(2,2) and O(4,4) scheme. Q=50 @ 40 Hz, velocity in medium is 2.0 km/s at 0 Hz.

grid-points/wavelength	Δx (m)	Δt (ms)
50	1	0.01
25	2	0.04
10	5	0.25
5	10	1.00
2	25	6.25

Table 3b. Simulation parameters for the O(2,4) scheme. Q=50 @ 40 Hz, velocity in medium is 2.0 km/s at 0 Hz.

grid-points/wavelentgth	Δx (m)	Δt (ms)
50	1	0.20
25	2	0.40
10	5	1.00
5	10	2.00
2	25	5.00

Table 3c. Simulation parameters for the O(2,4) scheme. Q=50 @ 40 Hz, velocity in medium is 2.0 km/s at 0 Hz. (constant Courant number = 0.4)

	Water	**Sediments**	**Basement**
v_p **(km/s)**	1.54	1.54	2.6
Q_p	10,000	50	450
v_s **(km/s)**	0	0.5	1.45
Q_s	0	35	225
ρ **(g/cm^3)**	1.05	1.7	2.8

Table 4. The average material properties used in the seafloor scattering experiment. v_p is the velocity of pressure waves and Q_p its quality factor, v_s is the shear wave velocity and Q_s its quality factor, ρ is the density.

	Water	**Layer 1**	**Layer 2**	**Layer 3**	**Layer 4**
v_p **(km/s)**	1.52	1.60	1.75	1.9	2.2
Q_p	10,000	40	50	50	100
v_s **(km/s)**	0	0.4	0.8	1.0	1.2
Q_s	0	30	35	45	70
ρ **(g/cm^3)**	1.05	1.3	1.5	1.5	2.0

Table 5. The average material properties used for the ensized valley model. v_p is the velocity of pressure waves and Q_p its quality factor, v_s is the shear wave velocity and Q_s its quality factor, ρ is the density. Layer 1, 2, 3, and 4 denotes the different sediment layers.

FIGURE CAPTIONS

Figure 1. Mechanical models of viscoelastic elements. The spring and the dashpot are illustrated in (**a**) while the standard linear solid is illustrated in (**b**).

Figure 2. Three optimized pairs of relaxation functions for a constant Q of 100 between 100 and 500 Hz. Solid: The desired function (between 100 and 500 Hz). Dashed: The optimized function using the approximation described in the text. Dotted: Exact Q using the optimized relaxation times.

Figure 3. Effects on Q by perturbations in the relaxation times. The case illustrated in Figure 1 was used as the unperturbed state. Solid: The desired function (between 100 and 500 Hz). Dashed: Q after increasing both the stress relaxation time and the strain relaxation time by 20%. Dotted: Q after increasing only the strain relaxation time by 20%.

Figure 4. Three optimized pairs of relaxation functions for a constant Q of 50 between 100 and 500 Hz. Solid: The desired function (between 100 and 500 Hz). Dashed: The optimized function using the approximation described in the text. Dotted: Exact Q using the optimized relaxation times.

Figure 5. The initial condition (the stress) in the numerical experiments is a Ricker wavelet with a center frequency at 35 Hz, traveling in a 2000 m long interval with periodic boundary conditions in the direction of increasing x with a velocity of 2000 m/s. The density is 2000 kg/m^3.

Figure 6. A case with severe numerical dispersion illustrating robust nature of the equation governing the memory variables. The same initial condition and material properties as in Figure 5 with a Q of 50 (relaxation times listed in Table 1) were used. The snapshot was taken at 2.25 s using a Courant number of 0.6 and a step size of 2m in the O(2,4) code. Solid: Crank-Nicholson used as the time stepping scheme in the equation governing the memory variables. Dashed: Fourth order Gear's method used as the time stepping scheme in the equation governing the memory variables.

Figure 7. A case with severe numerical dispersion illustrating robust nature of the equation governing the memory variables. The same initial condition and material properties as in Figure 5 with a Q of 10,000 (relaxation times listed in Table 1) were used. The snapshot was taken at 2.25 s using a Courant number of 0.6 and a step size of 2m in the O(2,4) code. Solid: Crank-Nicholson used as the time stepping scheme in the equation governing the memory variables. Dashed: Fourth order Gear's method used as the time stepping scheme in the equation governing the memory variables.

Figure 8. Snapshots at 2.25 s illustrating the dependence on Q using the O(2,2) code at a Courant number of 0.8 and a step size of 1m. The same initial condition and material properties as in Figure 5 were used. The relaxation times for the different values of Q are listed in Table 1. Solid: Q=50. Dashed: 200. Dotted: 10,000.

Figure 9. Snapshots at 2.25 s illustrating the dependence on Q using the O(2,4) code at a Courant number of 0.2 and a step size of 2m. The same initial condition and material properties as in Figure 5 were used. The relaxation times for the different values of Q are listed in Table 1. Solid: Q=50. Dashed: 200. Dotted: 10,000.

Figure 10. Snapshots at 2.25 s illustrating the dependence on the Courant number using the O(2,4) code at a step size of 2m. The same initial condition and material properties as in Figure 5 and a Q of 10,000 were used. The relaxation times for the different values of Q are listed in Table 1. Solid: Courant number = 0.6. Dashed: Courant number = 0.4. Dotted: Courant number = 0.2.

Figure 11. Snapshots at 2.25 s illustrating the dependence on the spatial step size using the O(2,4) code at a Courant number of 0.2. The same initial condition and material properties as in Figure 5 and a Q of 10,000 were used. The relaxation times for the different values of Q are listed in Table 1. Solid: Spatial step size = 1m. Dashed: Spatial step size = 2m. Dotted: Spatial step size = 3m.

Figure 12. Snapshot at 2.25 s illustrating the dependence on the Courant number using the O(4,4) code at a step size of 2m. The same initial condition and material properties as in Figure 5 and a Q of 10,000 were used. The relaxation times for the different values of Q are listed in Table 1. Solid: Courant number = 0.8. Dashed: Courant number = 0.4. Dotted: Courant number = 0.2.

Figure 13. Snapshots at 2.25 s illustrating the dependence on the spatial step size using the O(4,4) code at a Courant number of 0.8. The same initial condition and material properties as in Figure 5 and a Q of 10,000 were used. The relaxation times for the different values of Q are listed in Table 1. Solid: Spatial step size = 1m. Dashed: Spatial step size = 2m. Dotted: Spatial step size = 3m.

Figure 14. Snapshots at 2.25 s illustrating the dependence on Q using the O(4,4) code at a Courant number of 0.8 and a step size of 1m. The same initial condition and material properties as in Figure 5 were used. The relaxation times for the different values of Q are listed in Table 1. Solid: Q=50. Dashed: 200. Dotted: 10,000.

Figure 15. Snapshots at 2.25 s comparing the different schemes to each other using Q = 50 (see Table 1) and optimal choices of simulation parameters for the different schemes. The same initial condition and material properties as in Figure 5 were used. Solid: The O(4,4) scheme at a Courant number 0.8 and a spatial step size of 1m. Dashed: The O(2,4) scheme at a Courant number of 0.2 and a spatial step size of 2m. Dotted: The O(2,2) scheme at a Courant number of 0.8 and a spatial step size of 1m.

Figure 16. Snapshots at 2.25 s comparing the different schemes to each other using Q = 10,000 (see Table 1) and optimal choices of simulation parameters for the different schemes. The same initial condition and material properties as in Figure 5 were used. Solid: The O(4,4) scheme at a Courant number 0.8 and a spatial step size of 1m. Dashed: The O(2,4) scheme at a Courant number of 0.2 and a spatial step size of 2m. Dotted: The O(2,2) scheme at a Courant number of 0.8 and a spatial step size of 1m.

Figure 17. Seismogram at x=500 between 2.0 and 2.5 s comparing the O(4,4) scheme to an analytical solution to the solution from the O(4,4) scheme. Q = 10,000 (see Table 1) and the material properties are the same as in Figure 5. The initial condition is a narrow band amplitude modulated 50 Hz harmonic wave. Solid: Analytical solution from *Bland* [1960]. Dashed: Solution from the O(4,4) scheme using a Courant number of 0.8 and a spatial step size of 1m.

Figure 18. Seismogram at x=500 between 2.0 and 2.5 s comparing the O(4,4) scheme to an analytical solution to the solution from the O(4,4) scheme. Q = 200 (see Table 1) and the material properties are the same as in Figure 5. The initial condition is a narrow band amplitude modulated 50 Hz harmonic wave. Solid: Analytical solution from *Bland* [1960]. Dashed: Solution from the O(4,4) scheme using a Courant number of 0.8 and a spatial step size of 1m.

Figure 19. Snapshots at 2.25 s comparing experiments with a constant Q of 200 and three relaxation mechanisms (listed in Table 2) to one with one relaxation mechanism (listed in Table 1) using the O(2,4) scheme at a Courant number of 0.2 and a spatial step size of 2m. The same initial condition and material properties as in Figure 5 were used. Solid: Three pairs of relaxation mechanisms. Dashed: One pair of relaxation mechanisms.

Figure 20. Snapshots at 2.25 s comparing the memory variables in an experiment with a constant Q of 200 and three relaxation mechanisms (listed in Table 2) using the O(2,4) scheme at a Courant number of 0.2 and a spatial step size of 2m. The same initial condition and material properties as in Figure 5 were used. Solid: The memory variable corresponding to pair 1 of the relaxation mechanisms in Table 2. Dashed: The memory variable corresponding to pair 2 of the relaxation mechanisms in Table 2. Dotted: The memory variable corresponding to pair 3 of the relaxation mechanisms in Table 2.

Figure 21. Snapshots at 2.25 s comparing memory variables from experiments with a constant Q of 200 and three relaxation mechanisms (listed in Table 2) to one with one relaxation mechanism (listed in Table 1) using the O(2,4) scheme at a Courant number of 0.2 and a spatial step size of 2m. The same initial condition and material properties as in Figure 5 were used. Solid: The memory variable corresponding to pair 1 of the relaxation mechanisms in Table 2 from the experiment with three pairs of relaxation mechanisms. Dashed: The memory variable from the experiment using one pair of relaxation mechanisms (listed in Table 1).

Figure 22. Snapshots at 1.25 s and 2.25 s using the O(2,4) code at a Courant number of 0.2, a step size of 2m. The same initial condition and material properties as in Figure 5 were used with a constant Q of 200 using 3 pairs of relaxation mechanisms (listed in Table 2). Solid: Snapshot a 1.25 s. Dashed: Snapshot at 2.25 s.

Figure 23. Logarithmic L2 error for the O(2,2) scheme as a function of logarithm of grid-points/wavelength. The best fit line for the logarithmic L2 error decreases as -2.23, close to the theoretical value -2. Solid: Best fit line. Stars: L2 error

Figure 24. Snapshot of propagating sinusoid after 1.00 s for the O(2,2) scheme (velocity 2.0 km/s in medium). Solid: Analytic solution. Dashed: Numerical result 5 grid-points/wavelength. Dotted: Numerical result 2 grid-points/wavelength.

Figure 25. Snapshot of propagating sinusoid after 1.00 s for the O(2,2) scheme (velocity 2.0 km/s in medium). Solid: Analytic solution. Dashed: Numerical result 50 grid-points/wavelength. Dotted: Numerical result 25 grid-points/wavelength. Dash-dotted: Numerical result 10 grid-points/wavelength.

Figure 26. Logarithmic L2 error for the O(2,4) scheme as a function of logarithm of grid-points/wavelength. The best fit line for the logarithmic L2 error decreases as -5.13, close to the theoretical value -4. Solid: Best fit line. Stars: L2 error

Figure 27. Snapshot of propagating sinusoid after 1.00 s for the O(2,4) scheme (velocity 2.0 km/s in medium). Solid: Analytic solution. Dashed: Numerical result 5 grid-points/wavelength. Dotted: Numerical result 2 grid-points/wavelength.

Figure 28. Snapshot of propagating sinusoid after 1.00 s for the O(2,4) scheme (velocity 2.0 km/s in medium). Solid: Analytic solution. Dashed: Numerical result 50 grid-points/wavelength. Dotted: Numerical result 25 grid-points/wavelength. Dash-dotted: Numerical result 10 grid-points/wavelength.

Figure 29. Logarithmic L2 error for the O(2,4) scheme as a function of logarithm of grid-points/wavelength (constant Courant number=0.4). The best fit line for the logarithmic L2 error decreases as -1.54. The good fit at low number of grid-points/wavelength depends on the large damping of the sinusoid. Solid: Best fit line. Stars: L2 error

Figure 30. Snapshot of propagating sinusoid after 1.00 s for the O(2,4) scheme (constant Courant number, velocity 2.0 km/s in medium). Solid: Analytic solution. Dashed: Numerical result 5 grid-points/wavelength. Dotted: Numerical result 2 grid-points/wavelength.

Figure 31. Snapshot of propagating sinusoid after 1.00 s for the O(2,4) scheme (constant Courant number, velocity 2.0 km/s in medium). Solid: Analytic solution. Dashed: Numerical result 50 grid-points/wavelength. Dotted: Numerical result 25 grid-points/wavelength. Dash-dotted: Numerical result 10 grid-points/wavelength.

Figure 32. Logarithmic L2 error for the O(4,4) scheme as a function of logarithm of grid-points/wavelength. The best fit line for the logarithmic L2 error decreases as -5.13, close to the theoretical value -4. Solid: Best fit line. Stars: L2 error

Figure 33. Snapshot of propagating sinusoid after 1.00 s for the O(4,4) scheme (velocity 2.0 km/s in medium). Solid: Analytic solution. Dashed: Numerical result 5 grid-points/wavelength. Dotted: Numerical result 2 grid-points/wavelength.

Figure 34. Snapshot of propagating sinusoid after 1.00 s for the O(4,4) scheme (velocity 2.0 km/s in medium). Solid: Analytic solution. Dashed: Numerical result 50 grid-points/wavelength. Dotted: Numerical result 25 grid-points/wavelength. Dash-dotted: Numerical result 10 grid-points/wavelength.

Figure 35. Damping for Crank-Nicholson and Euler backward schemes in the equation for the memory variable. The curve for the Crank-Nicholson scheme is close to the theoretical curve at all frequencies. The Euler backward scheme underestimates the damping at high wavenumbers. Q=50 @ 40 Hz, $\Delta t/\tau_\sigma$=0.24. This ratio between the relaxation time and the time step is very large and will seldom be encountered due to the stability criterion and dispersion properties for a full scheme. Solid: Theoretical curve. Dashed: Crank-Nicholson. Dotted: Euler backward.

Figure 36. Dispersion for the O(2,2) and O(2,4) schemes. The Courant number increases from 0.05,0.2 to 0.4 for both schemes. The O(2,4) scheme overestimates the velocity for a Courant number of 0.4. The O(2,4) curve approximates the theoretical curve considerably better than the O(2,2) curve. Maximum frequency 500 Hz. Q=50 @ 7.5 Hz. Solid: Theoretical curve. Dashed: O(2,4). Dotted: O(2,2).

Figure 37. Dispersion for the O(2,2) and O(2,4) schemes. The Courant number increases from 0.6 to 0.7 for both schemes. The O(2,4) scheme overestimates the velocity for these Courant numbers. The fit of the O(2,2) is still poor. Maximum

frequency 500 Hz. Q=50 @ 37.5 Hz. Solid: Theoretical curve. Dashed: O(2,4). Dotted: O(2,2).

Figure 38. Damping for the O(2,2) scheme. The Courant number varies from 0.4, 0.7 to 0.9 . The damping is underestimated for all Courant numbers. Maximum frequency 500 Hz. Q=50 @ 37.5 Hz. Solid: Theoretical curve. Dashed: O(2,2) C=0.4 . Dotted: O(2,2) C=0.7 . Dash-dotted: O(2,2) C=0.9 .

Figure 39. Damping for the O(2,4) scheme. The Courant number varies from 0.05, 0.4 to 0.7 . The damping is underestimated for Courant number=0.05, 0.4 and overestimated for Courant number=0.7 . Maximum frequency 500 Hz. Q=50 @ 37.5 Hz. Solid: Theoretical curve. Dashed: O(2,4) C=0.05 . Dotted: O(2,4) C=0.4 . Dash-dotted: O(2,4) C=0.7 .

Figure 40. Dispersion for the O(4,4) scheme. The Courant number varies from 0.2, 0.4, 0.6, 0.8 to 0.9 . The O(4,4) aligns very well to the theoretical curve. Maximum frequency 500 Hz. Q=50 @ 37.5 Hz. Solid (top): Theoretical curve. Dashed (bottom): O(4,4) C=0.2 . Dotted: O(4,4) C=0.4 . Dash-dotted: O(4,4) C=0.6 . Solid (bottom): O(4,4) C=0.8 . Dashed (top): O(4,4) C=0.9 .

Figure 41. Damping for the O(4,4) scheme. The damping is overestimated for large Courant numbers and slightly underestimated for Courant number=0.2. Solid (bottom): Theoretical curve. Dashed (bottom): O(4,4) C=0.2 . Dotted: O(4,4) C=0.4 . Dash-dotted: O(4,4) C=0.6 . Solid (top): O(4,4) C=0.8 . Dashed (top): O(4,4) C=0.9 .

Figure 42. Dispersion for the O(4,4) scheme and the pseudo O(4,4) scheme for a Courant number = 0.8 . The dispersion for the two schemes is virtually identical. Solid: Theoretical curve. Dashed: O(4,4) scheme. Dotted: pseudo O(4,4) scheme.

Figure 43. Damping for the O(4,4) scheme and the pseudo O(4,4) scheme for a Courant number = 0.8 . The pseudo O(4,4) scheme overestimates the damping slightly at the point of maximum damping, but it aligns better to the theoretical curve, for high wavenumbers, than the O(4,4) scheme. Solid: Theoretical curve. Dashed: O(4,4) scheme. Dotted: pseudo O(4,4) scheme.

Figure 44. Poles of the modal equation for the O(2,4) scheme. The poles with negative real part lies outside the unit circle. Poles located on the positive real axis inside the unit circle originates from the memory variable equation. Solid: Unit circle. Stars: Pole locations.

Figure 45. The absolute values minus one for the poles with negative real part for the O(2,4) scheme. The poles corresponding to half the Nyquist frequency have the largest absolute values. Courant number=0.4, Q=50 @ 37.5 Hz. Solid: Absolute value of poles.

Figure 46. Poles of the modal equation for a scheme with spectral accuracy for spatial derivatives. The poles with positive real part lies outside the unit circle. Q=50 @ 37.5 Hz. Solid: Unit circle. Stars and crosses: Pole locations.

Figure 47. The absolute values minus one for the poles with positive real part for the spectral scheme. Q=50 @ 37.5 Hz. Solid: Absolute values of poles.

Figure 48. Poles of the modal equation for the O(2,4) scheme. Dissipation introduced in p equation. All poles are on or inside the unit circle. Courant number=0.4, Q=50 @ 37.5 Hz. Solid: Unit circle. Stars: pole locations.

Figure 49. The absolute values minus one for the poles with negative real part for the O(2,4) scheme after dissipative term has been added to the p equation. The poles corresponding to half the Nyquist frequency have the smallest absolute values. Courant number=0.4, Q=50 @ 37.5 Hz. Solid: Absolute value of poles.

Figure 50. Dispersion for the O(2,4) scheme with and without dissipative term. The dispersion curve for the scheme with dissipative term completely coincides with the dispersion curve for the scheme without a dissipative term. Courant number =0.4, Q=50 @ 37.5 Hz. Solid: Theoretical curve. Dashed: Dispersion curve for O(2,4) with dissipative term. Dotted: Dispersion curve for O(2,4) without dissipative term.

Figure 51. Damping for the O(2,4) scheme with and without dissipative term. The curve for the O(2,4) with dissipative overestimates the damping for high wavenumbers and at the peak of the damping curve. Courant number=0.4, Q=50 @ 37.5 Hz. Solid: Theoretical curve. Dashed: Damping curve for O(2,4) with dissipative term. Dotted: Damping curve for O(2,4) without dissipative term.

Figure 52. The sedimented seafloor profile used in the seafloor scattering experiment (6.2 km-7.2 km from profile v2602c, *Goff et al.*, 1992). Solid: Basement profile. Dashed: Sediment profile.

Figure 53. Initial condition (a) and snapshots of the scattered energy from viscoelastic sedimented (b-e), elastic sedimented (f), and bare seafloors (g). The tapered amplitude modulated plane wave of 140 Hz is incident at 10 degrees grazing angle. The material properties are listed in Table 4.
The absorbing boundaries are cut out from the snapshots. The unit of the scales on the axes are meters and are relative to the upper left corner in the grid when the absorbing boundaries are included.

a. Initial condition, P-wave energy (S-wave energy is 0).
b. P-wave energy for a viscoelastic sedimented seafloor at 0.2 s.
c. S-wave energy for a viscoelastic sedimented seafloor at 0.2 s.
d. P-wave energy for a viscoelastic sedimented seafloor at 0.4 s.
e. S-wave energy for a viscoelastic sedimented seafloor at 0.4 s.
f. P-wave energy for an elastic sedimented seafloor at 0.4 s.
g. P-wave energy for a bare seafloor at 0.4 s.

Figure 54. The model used in the incised valley experiment. The area above the solid line is water. The area between the solid and the dashed line represents Holocene transgressive marine deposits. The area between the dashed and the dotted line represents transgressive marine overlying transgressive estuarine deposits. The area between the dotted and the dash-dotted line represent regressive fluvial deposits. The dotted line indicates the bay line, the boundary between the regressive and transgressive sequences. The area below the solid line and above the dash-dotted line are late Pleistocene to Holocene deposits. The area below the dash-dotted line represents early Wisconsinian regressive deposits. The star shows the position of the source.

Figure 55. Initial condition, P-wave energy (S-wave energy is 0). The absorbing boundaries are cut out from the snapshots. The unit of the scales on the axes are meters and are relative to the upper left corner in the grid when the absorbing boundaries are included.

Figure 56. Snapshots of P-wave energy (a, c, e, g) and SV-wave energy (b, d, f, h) for the viscoelastic incised valley model. Material properties are listed in Table 5. The absorbing boundaries are cut out from the snapshots. The unit of the scales on the axes are meters and are relative to the upper left corner in the grid when the absorbing boundaries are included.

a. P-wave energy for the viscoelastic model at 0.05 s.
b. SV-wave energy for the viscoelastic model at 0.05 s.
c. P-wave energy for the viscoelastic model at 0.1 s.
d. SV-wave energy for the viscoelastic model at 0.1 s.
e. P-wave energy for the viscoelastic model at 0.2 s.
f. SV-wave energy for the viscoelastic model at 0.2 s.
g. P-wave energy for the viscoelastic model at 0.3 s.
h. SV-wave energy for the viscoelastic model at 0.3 s.

Figure 57. Snapshots of P-wave energy (a, c, e, g) and SV-wave energy (b, d, f, h) for the elastic incised valley model. Material properties are listed in Table 5. The absorbing boundaries are cut out from the snapshots. The unit of the scales on the axes are meters and are relative to the upper left corner in the grid when the absorbing boundaries are included.

a. P-wave energy for the elastic model at 0.05 s.
b. SV-wave energy for the elastic model at 0.05 s.
c. P-wave energy for the elastic model at 0.1 s.
d. SV-wave energy for the elastic model at 0.1 s.
e. P-wave energy for the elastic model at 0.2 s.
f. SV-wave energy for the elastic model at 0.2 s.
g. P-wave energy for the elastic model at 0.3 s.
h. SV-wave energy for the elastic model at 0.3 s.

The spring

The dashpot

(a)

Standard linear solid

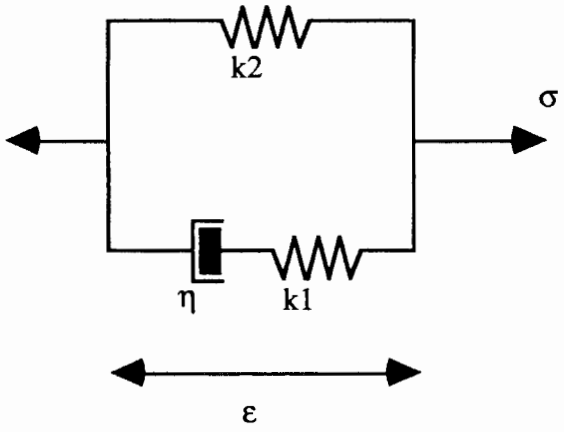

(b)

Figure 1. Illustration of the spring and the dashpot (a) and the standard linear solid (b).

The spring

The dashpot

(a)

Standard linear solid

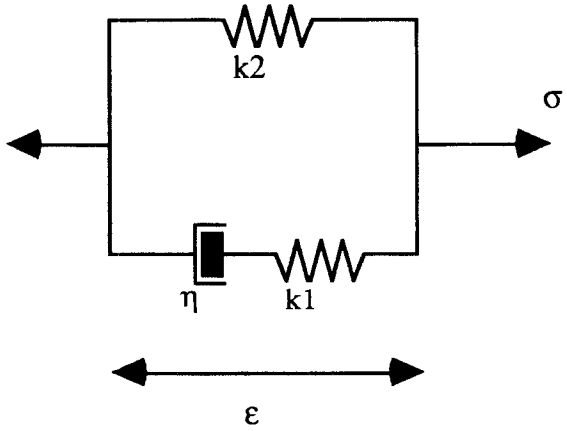

(b)

Figure 1.

Figure 2.

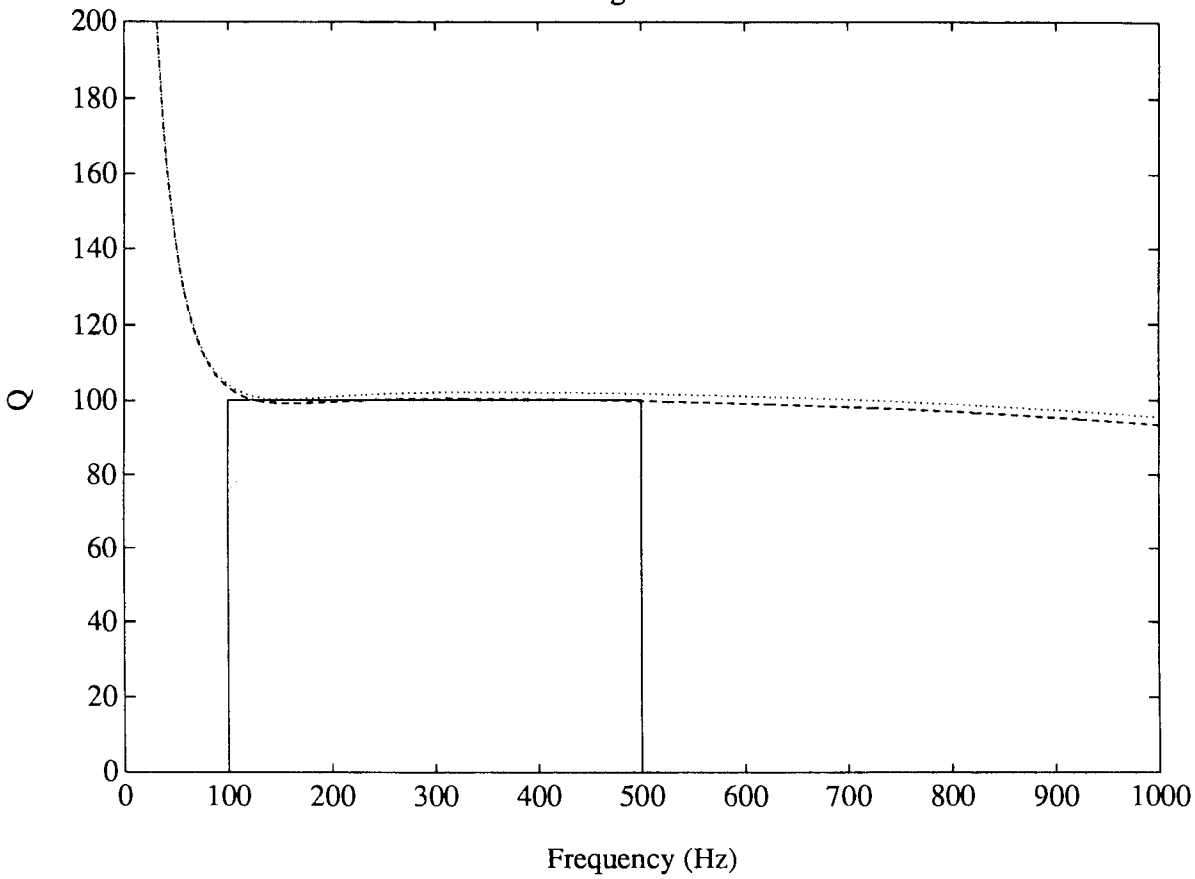
200
180
160
140
120
100
80
60
40
20
0
Q
0
100
200
300
400
500
600
700
800
900
1000
Frequency (Hz)

Figure 3.

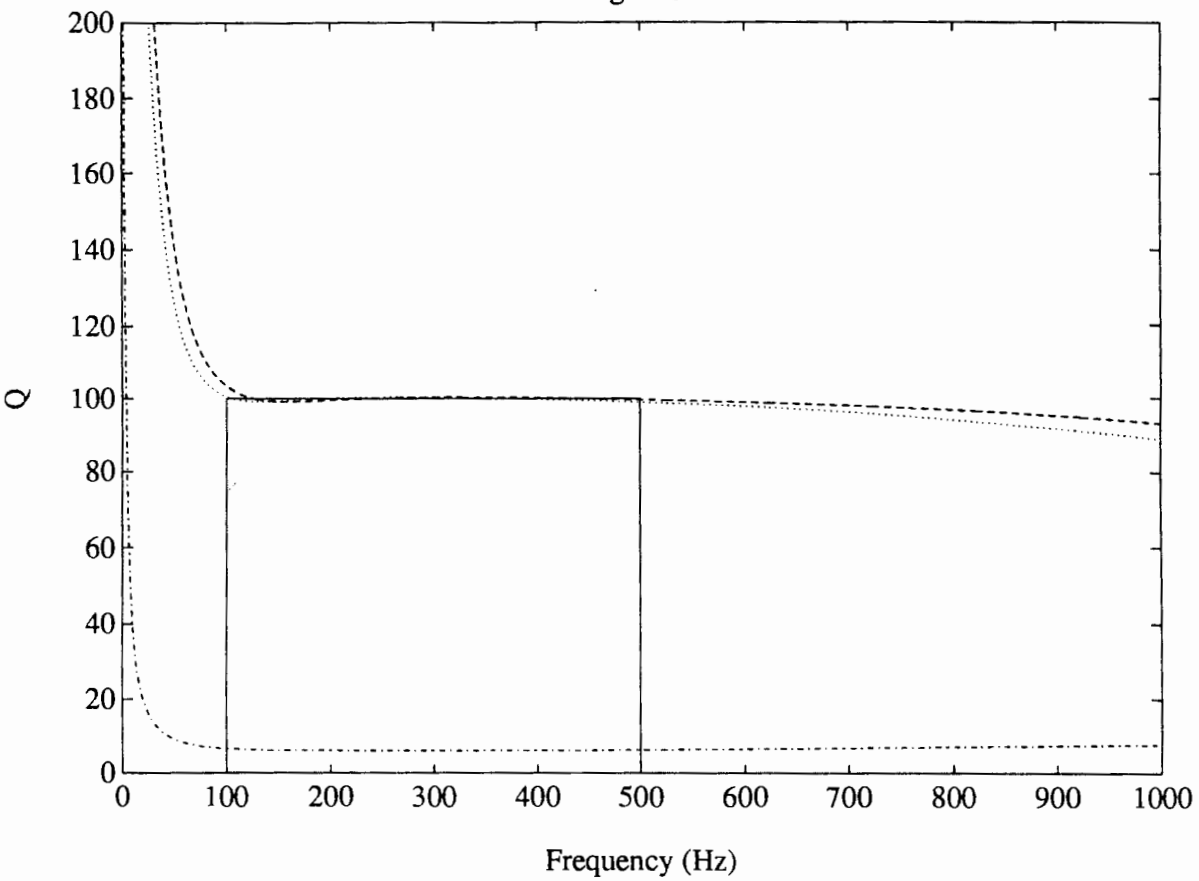
200
180
160
140
120
100
80
60
40
20
0
Q
0
100
200
300
400
500
600
700
800
900
1000
Frequency (Hz)

Figure 4.

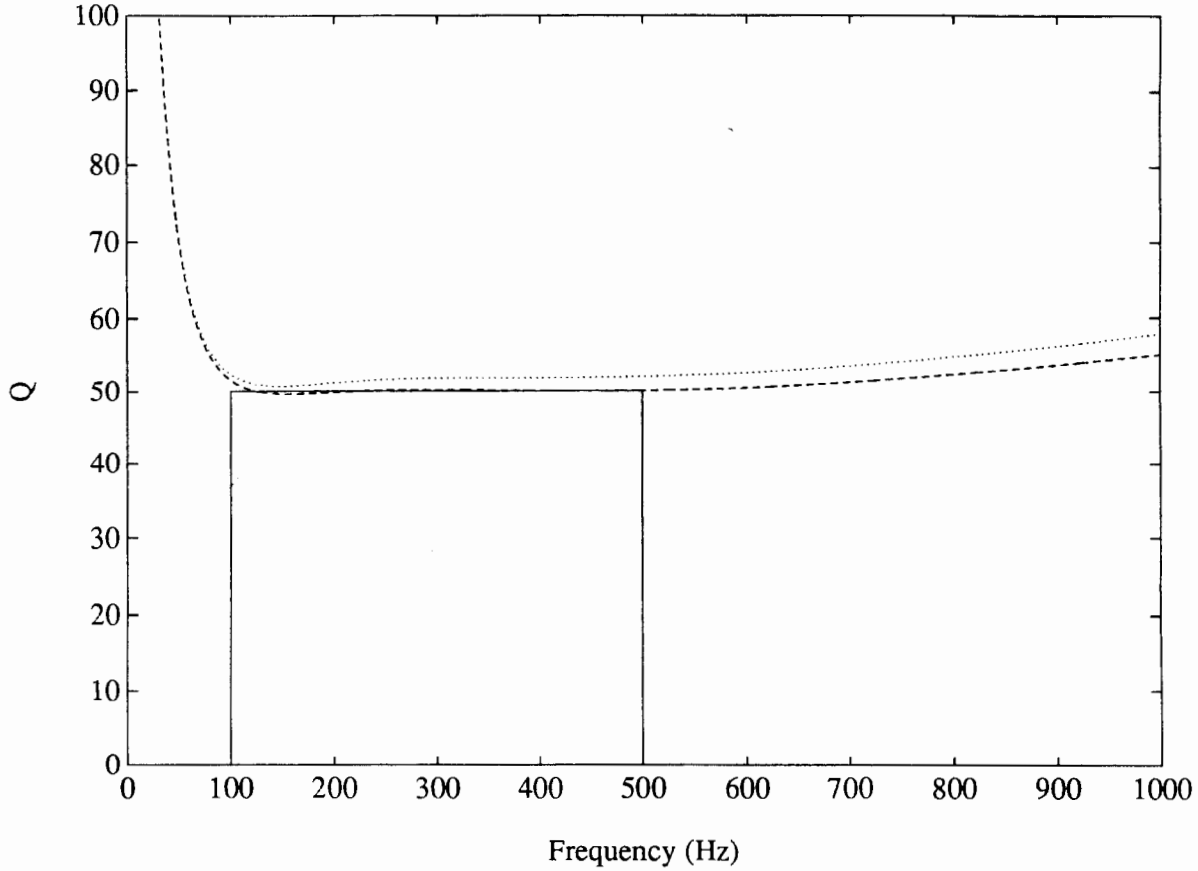
100
90
80
70
60
50
40
30
20
10
0
Q
0
100
200
300
400
500
600
700
800
900
1000
Frequency (Hz)

Figure 5.

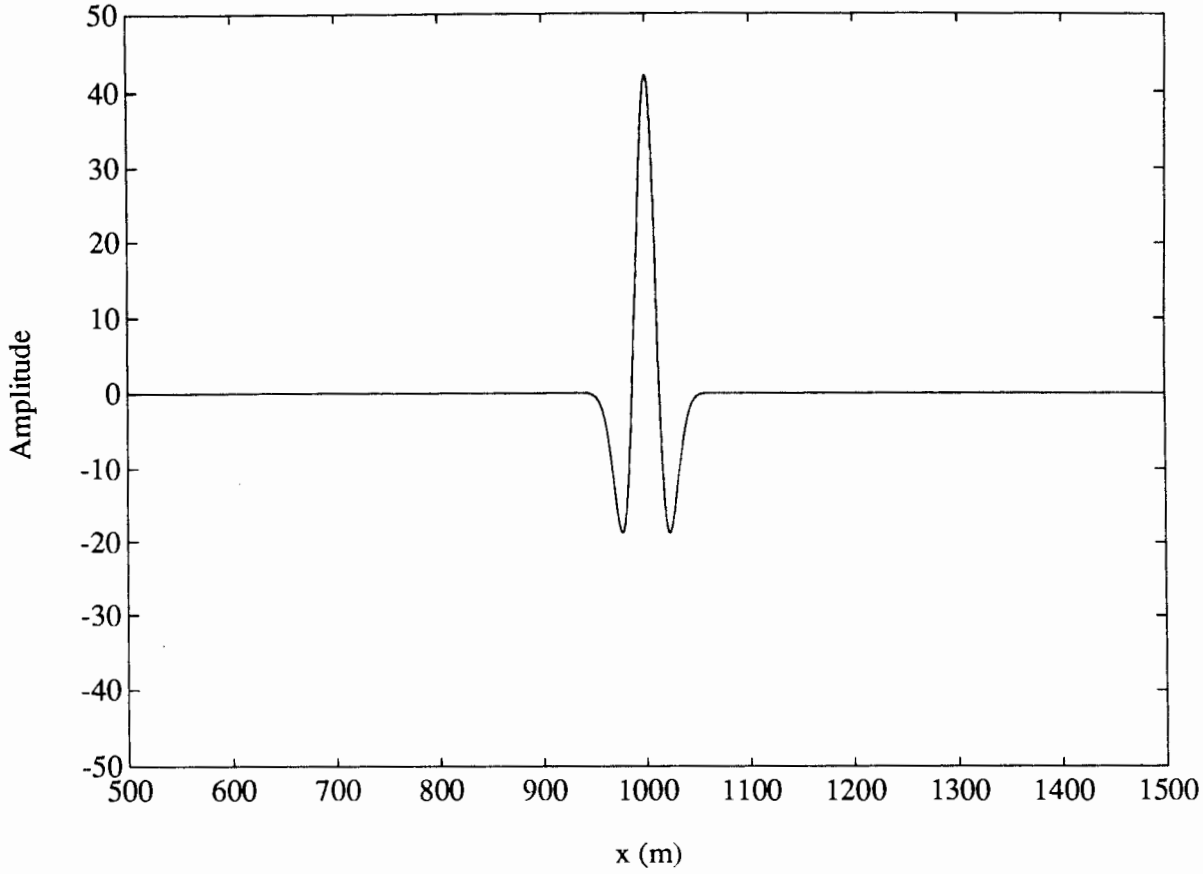
50
40
30
20
10
0
-10
-20
-30
-40
-50
Amplitude
500
600
700
800
900
1000
1100
1200
1300
1400
1500
x (m)

Figure 6.

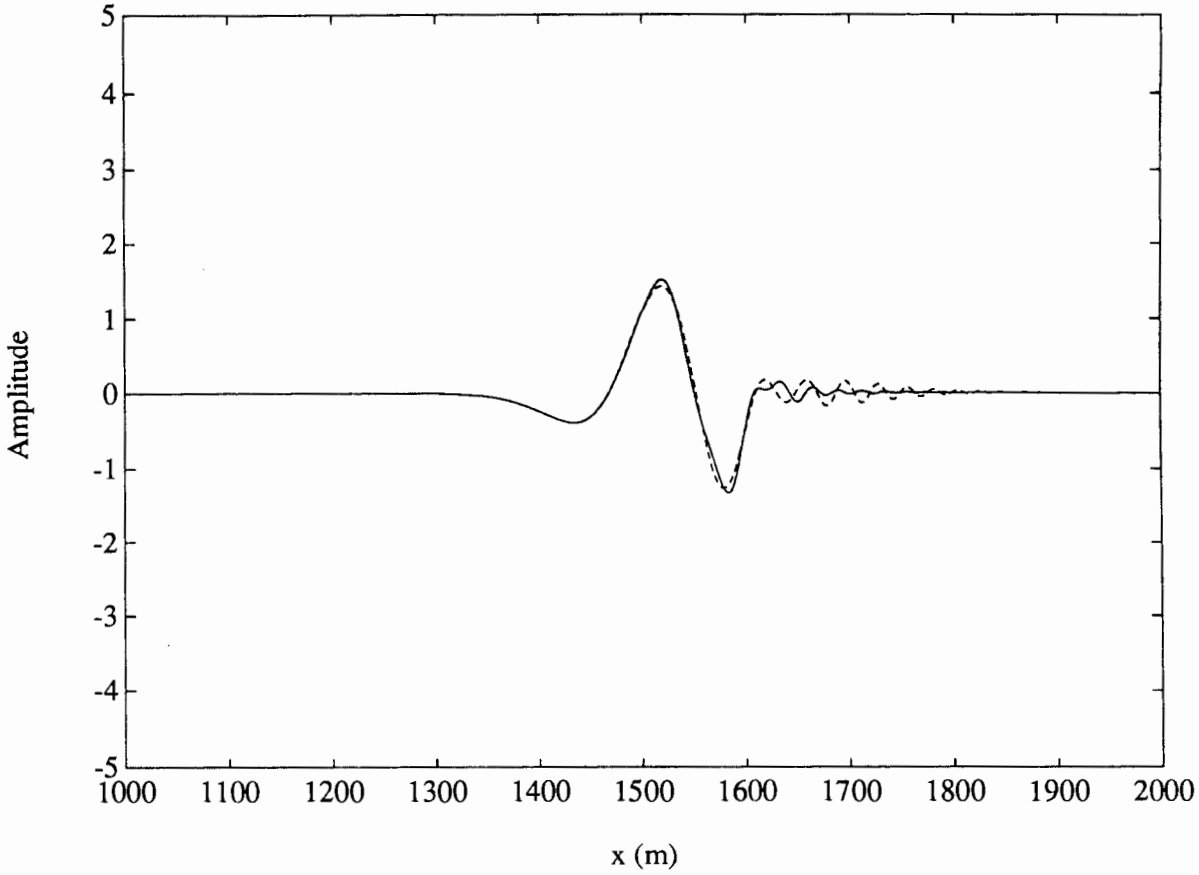
5
4
3
2
1
0
-1
-2
-3
-4
-5
Amplitude
1000
1100
1200
1300
1400
1500
1600
1700
1800
1900
2000
x (m)

Figure 7.

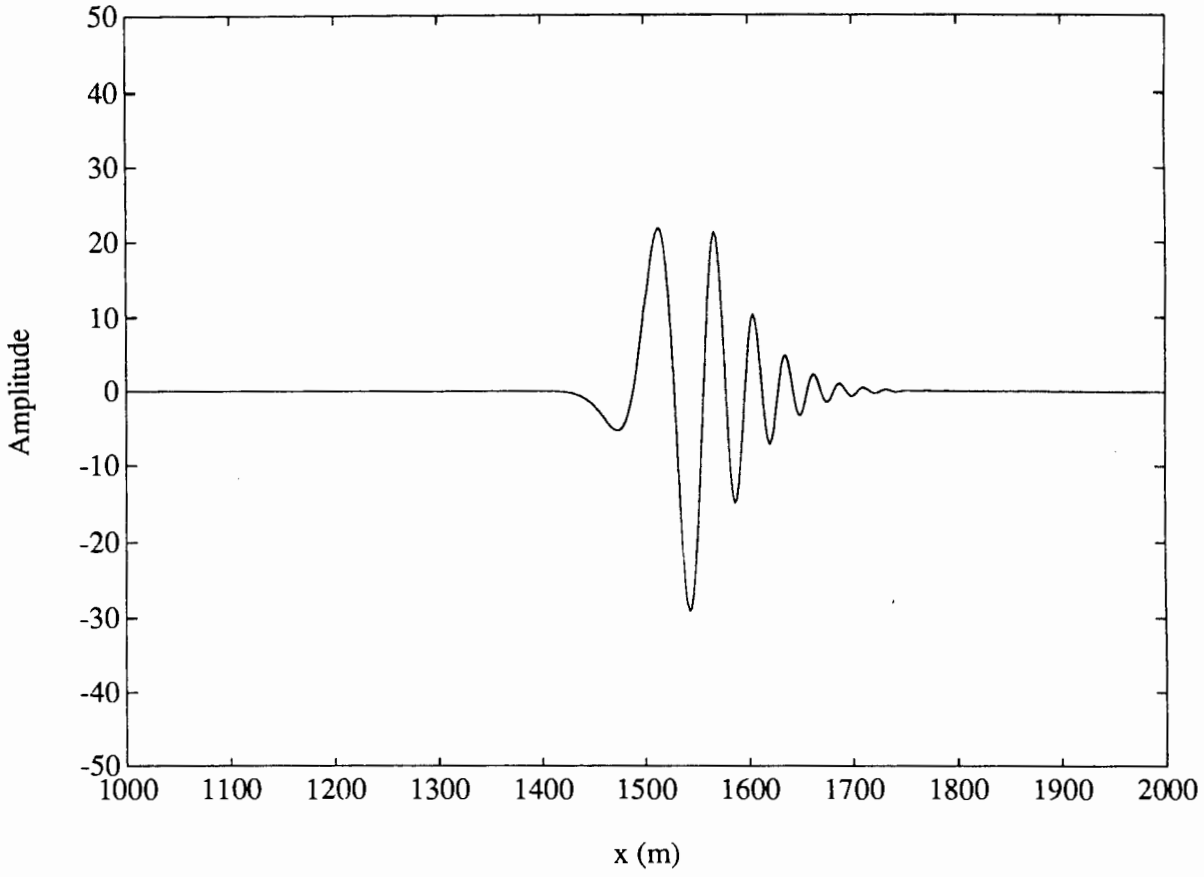
50
40
30
20
10
0
-10
-20
-30
-40
-50
Amplitude
1000
1100
1200
1300
1400
1500
1600
1700
1800
1900
2000
x (m)

Figure 8.

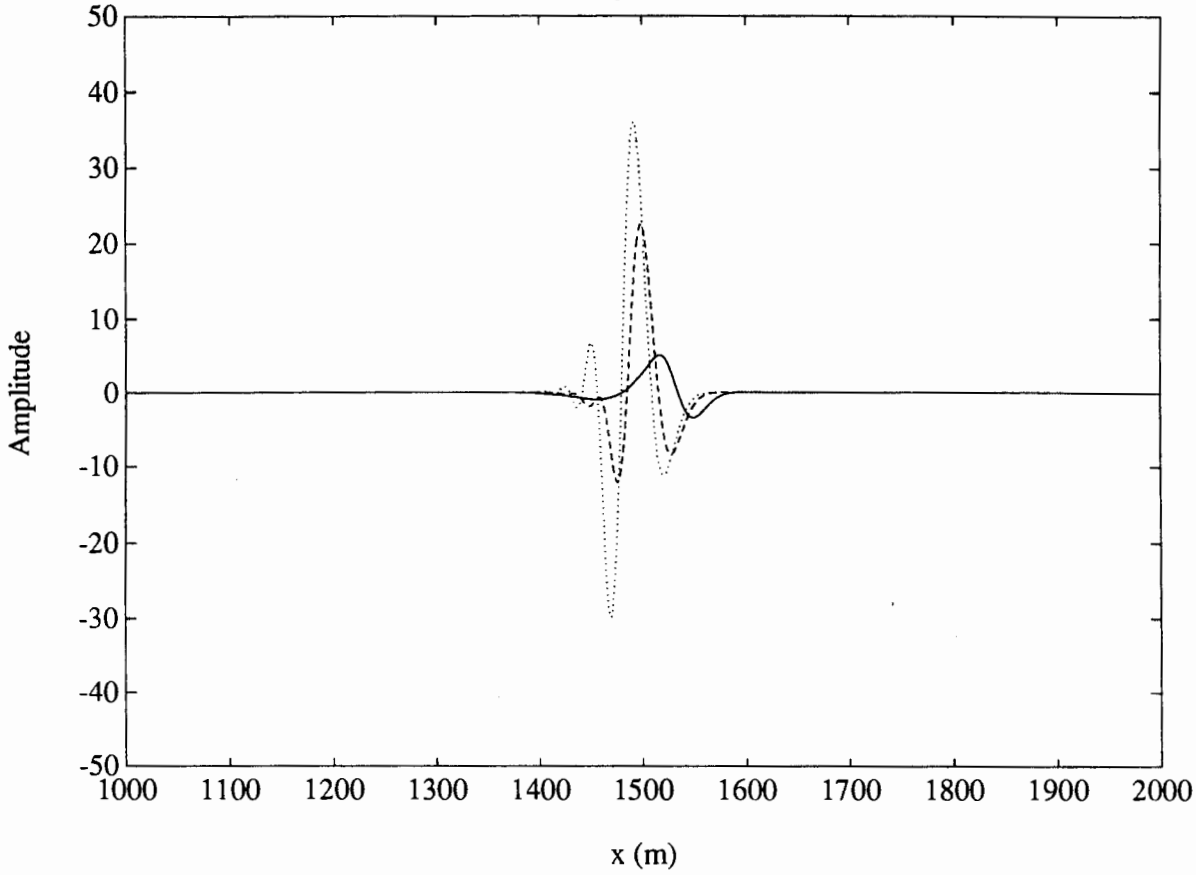
50
40
30
20
10
0
-10
-20
-30
-40
-50
Amplitude
1000
1100
1200
1300
1400
1500
1600
1700
1800
1900
2000
x (m)

Figure 9.

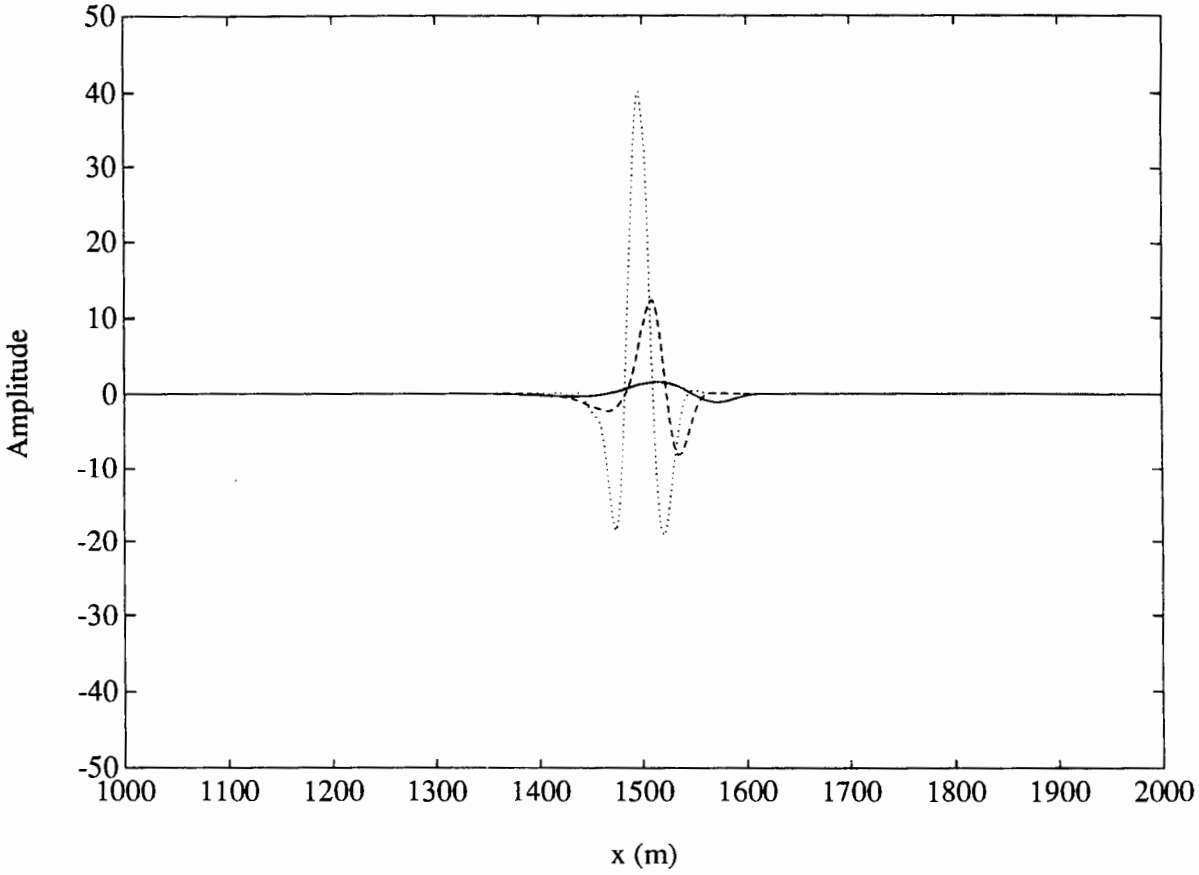
50
40
30
20
10
0
-10
-20
-30
-40
-50
Amplitude
1000
1100
1200
1300
1400
1500
1600
1700
1800
1900
2000
x (m)

Figure 10.

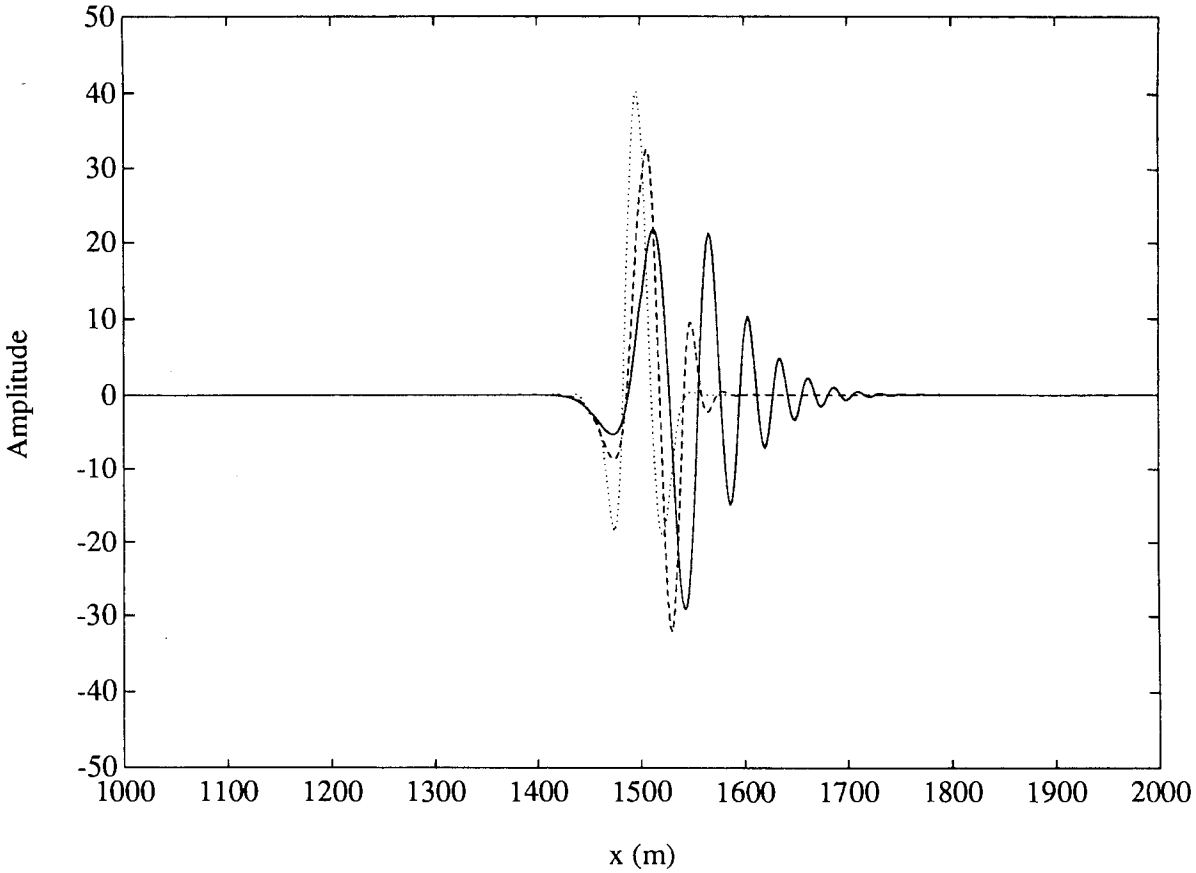
50
40
30
20
10
0
-10
-20
-30
-40
-50
Amplitude
1000
1100
1200
1300
1400
1500
1600
1700
1800
1900
2000
x (m)

Figure 11.

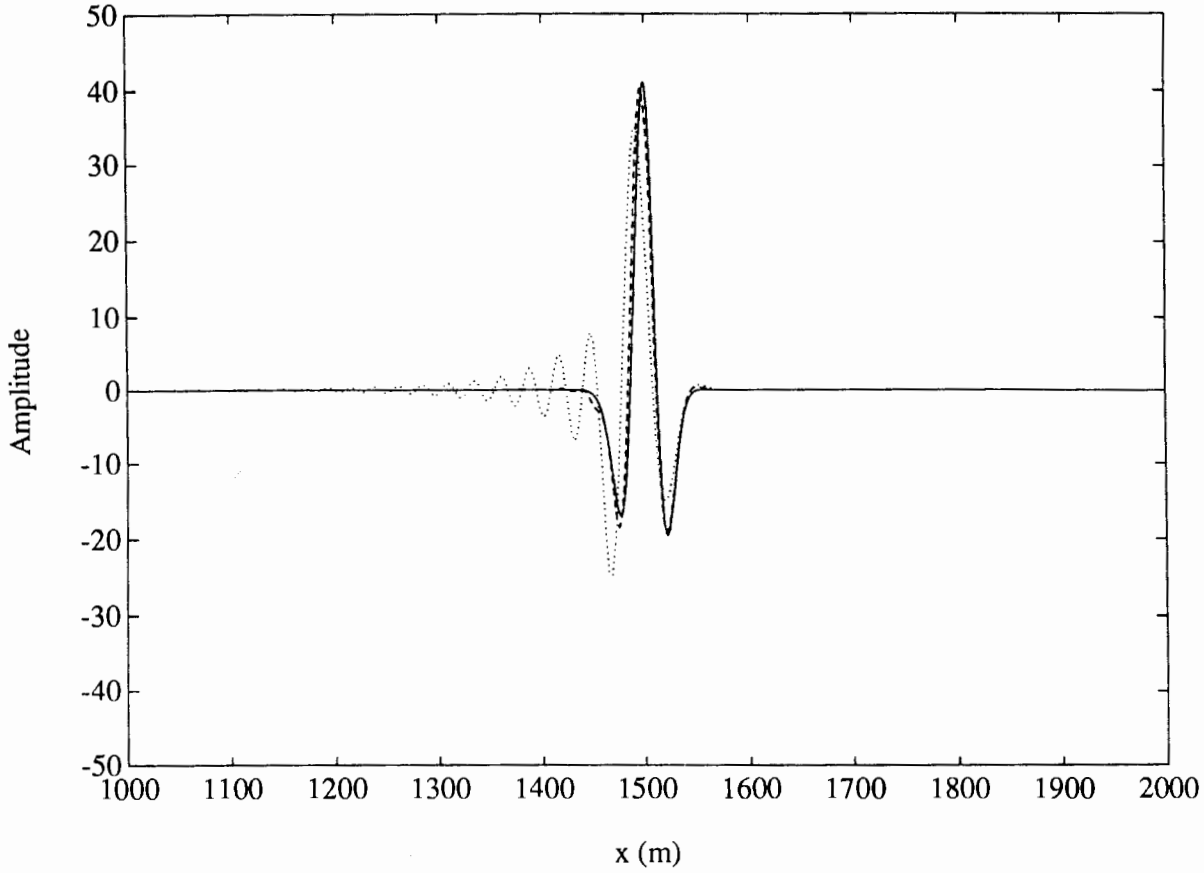
50
40
30
20
10
0
-10
-20
-30
-40
-50
Amplitude
1000
1100
1200
1300
1400
1500
1600
1700
1800
1900
2000
x (m)

Figure 12.

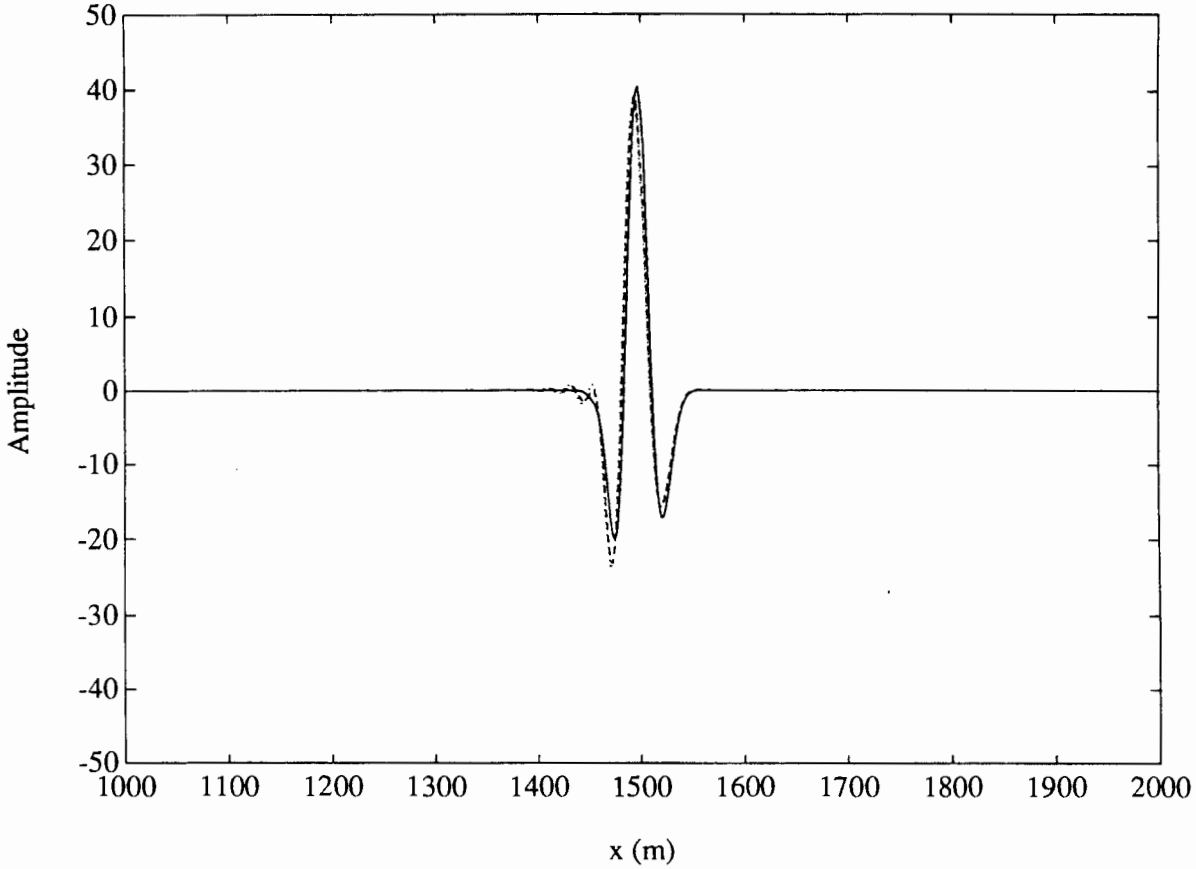
50
40
30
20
10
0
-10
-20
-30
-40
-50
Amplitude
1000
1100
1200
1300
1400
1500
1600
1700
1800
1900
2000
x (m)

Figure 13.

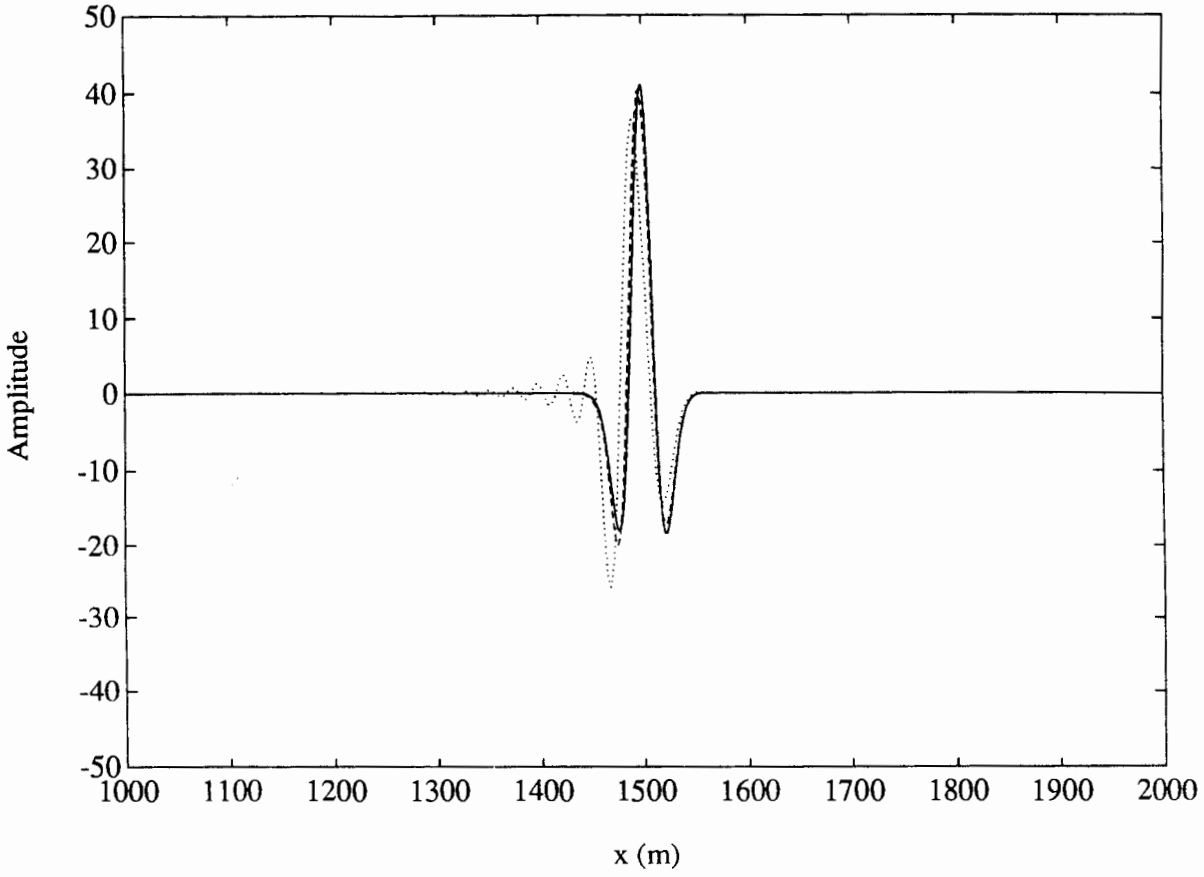
50
40
30
20
10
0
-10
-20
-30
-40
-50
Amplitude
1000
1100
1200
1300
1400
1500
1600
1700
1800
1900
2000
x (m)

Figure 14.

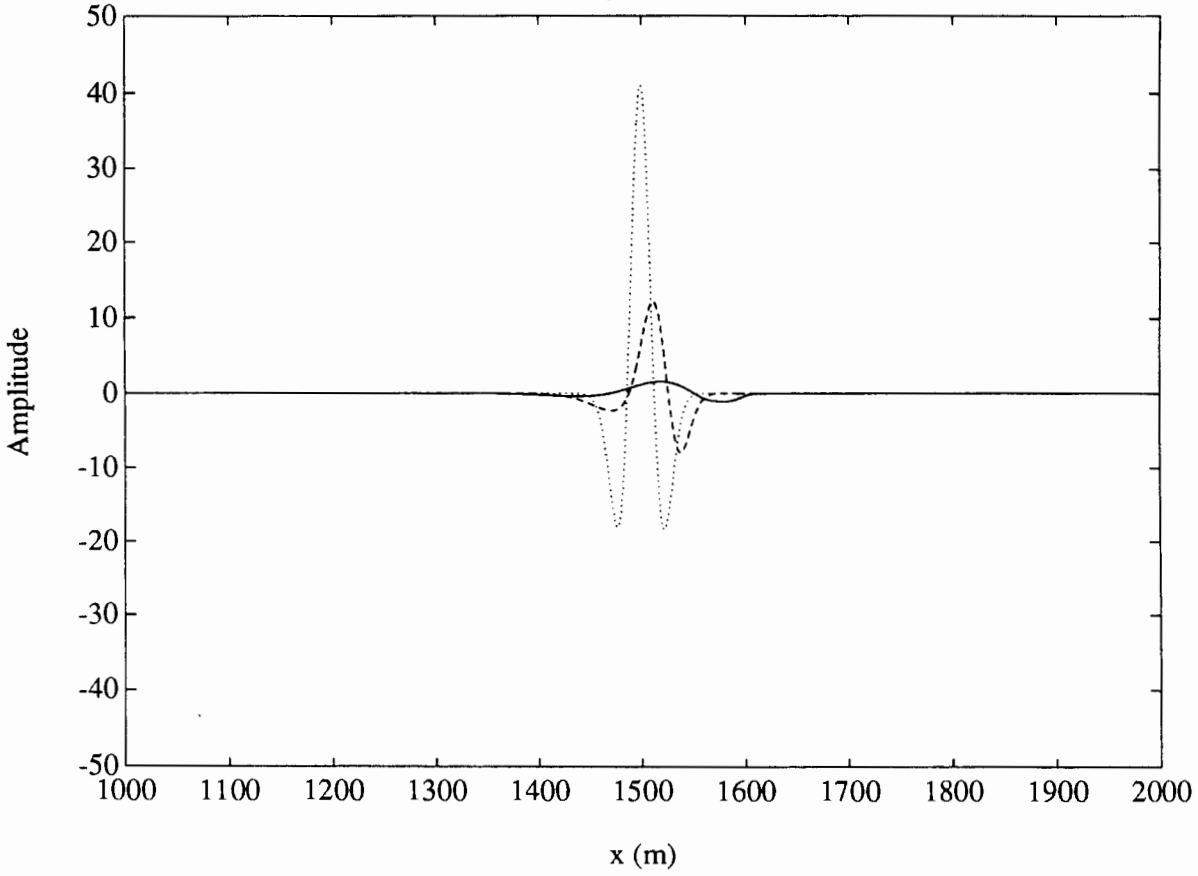
50
40
30
20
10
0
-10
-20
-30
-40
-50
Amplitude
1000
1100
1200
1300
1400
1500
1600
1700
1800
1900
2000
x (m)

Figure 15.

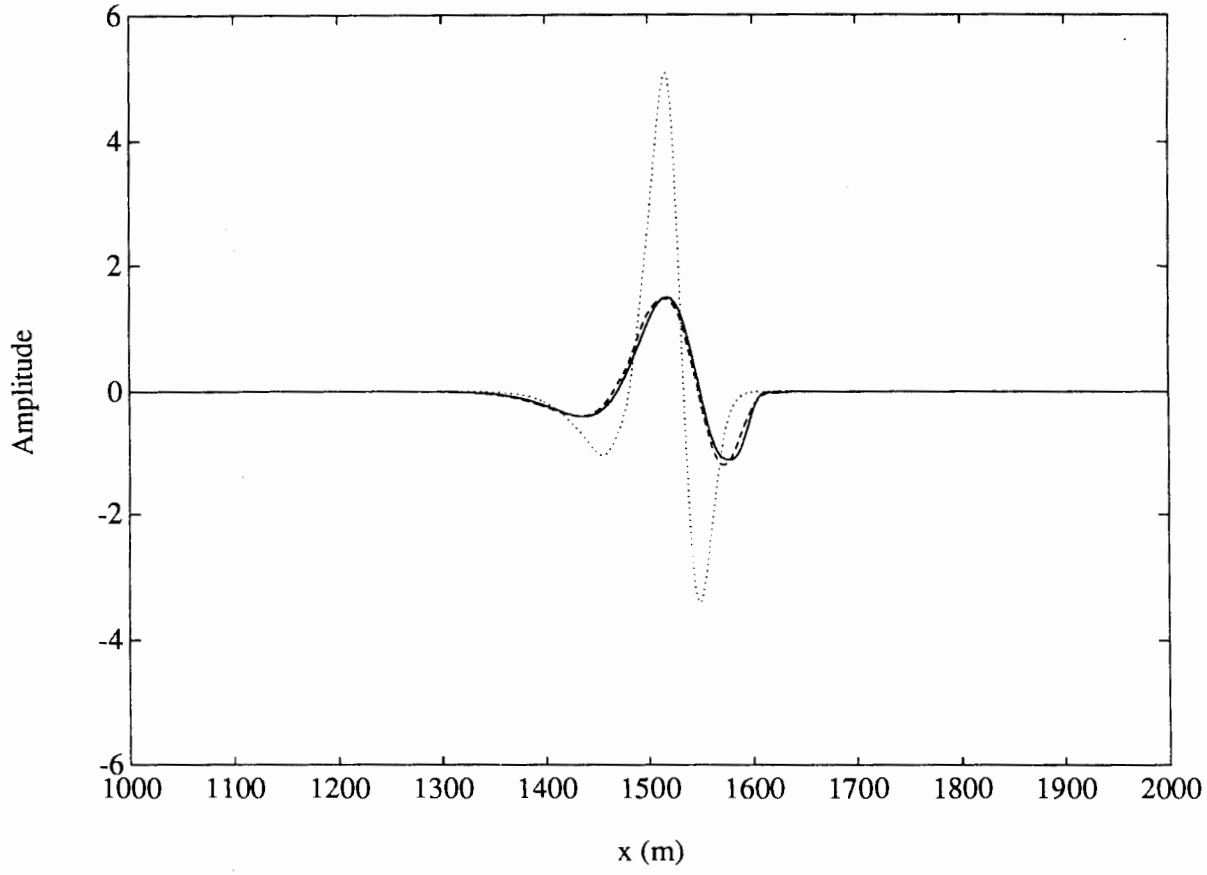
6
4
2
0
-2
-4
-6
Amplitude
1000
1100
1200
1300
1400
1500
1600
1700
1800
1900
2000
x (m)

Figure 16.

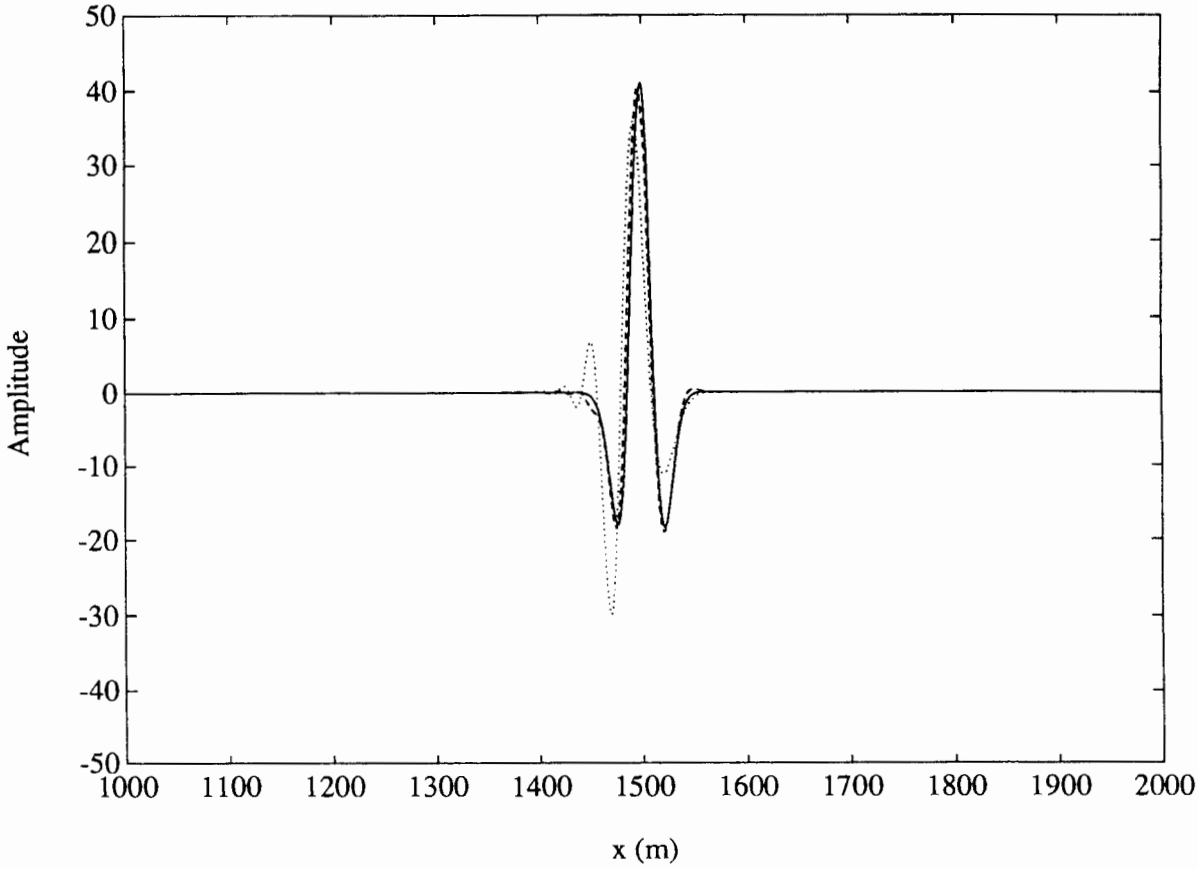
50
40
30
20
10
0
-10
-20
-30
-40
-50
Amplitude
1000
1100
1200
1300
1400
1500
1600
1700
1800
1900
2000
x (m)

Figure 17.

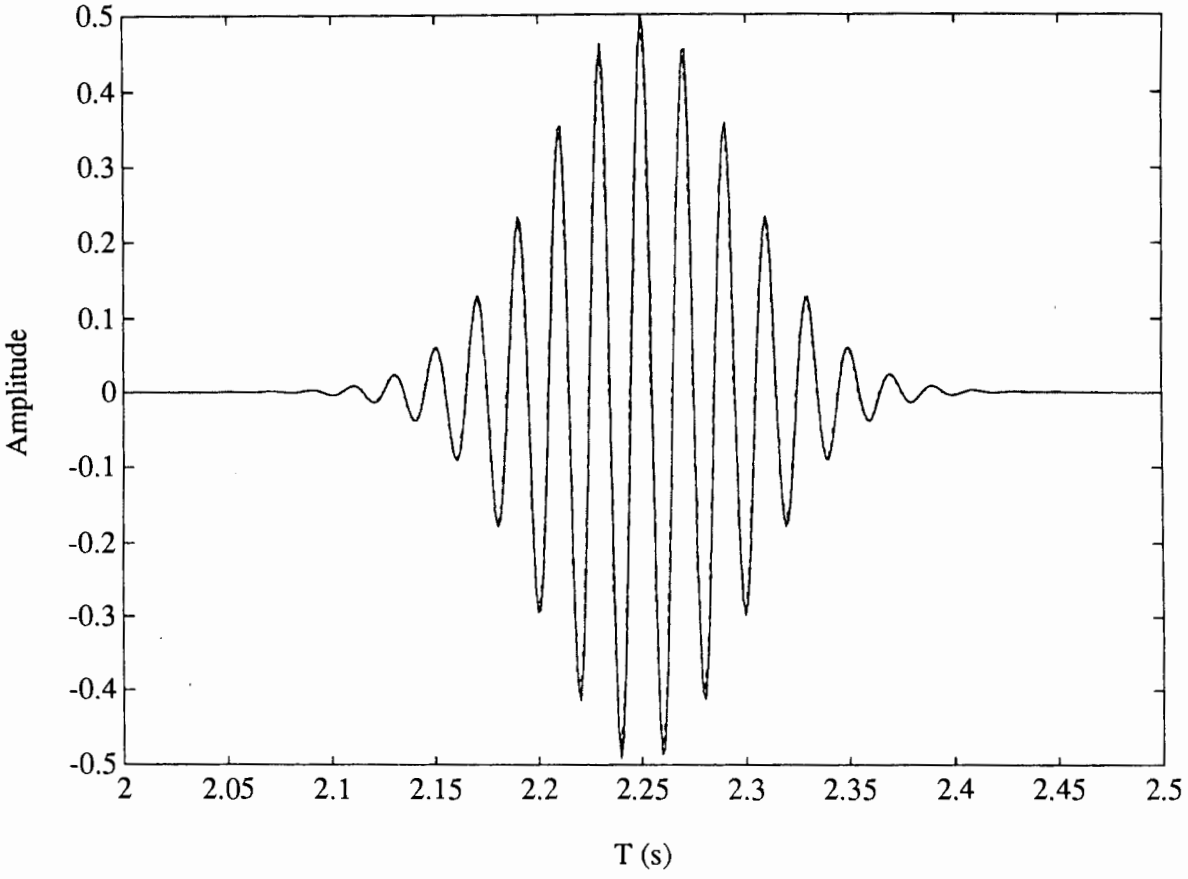
0.5
0.4
0.3
0.2
0.1
0
-0.1
-0.2
-0.3
-0.4
-0.5
Amplitude
2
2.05
2.1
2.15
2.2
2.25
2.3
2.35
2.4
2.45
2.5
T (s)

Figure 18.

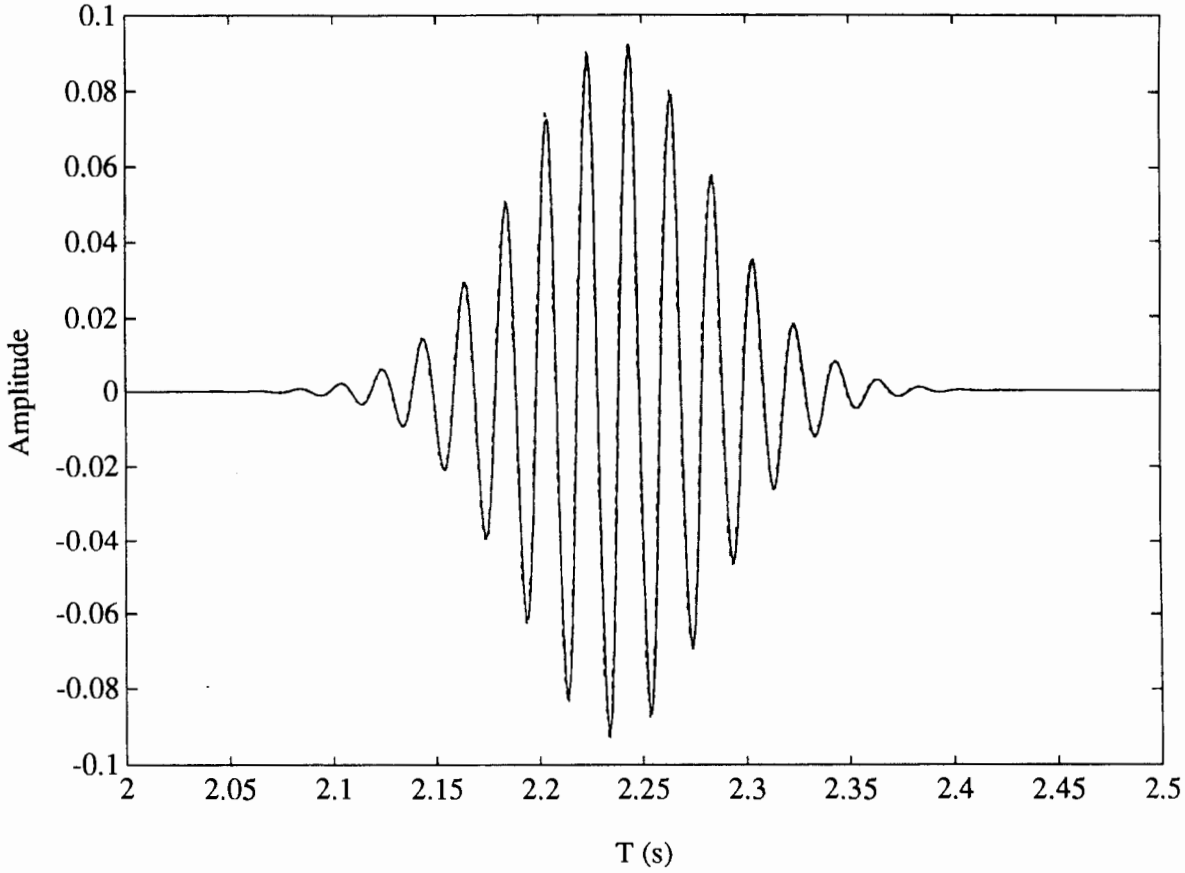
0.1
0.08
0.06
0.04
0.02
0
-0.02
-0.04
-0.06
-0.08
-0.1
Amplitude
2
2.05
2.1
2.15
2.2
2.25
2.3
2.35
2.4
2.45
2.5
T (s)

Figure 19.

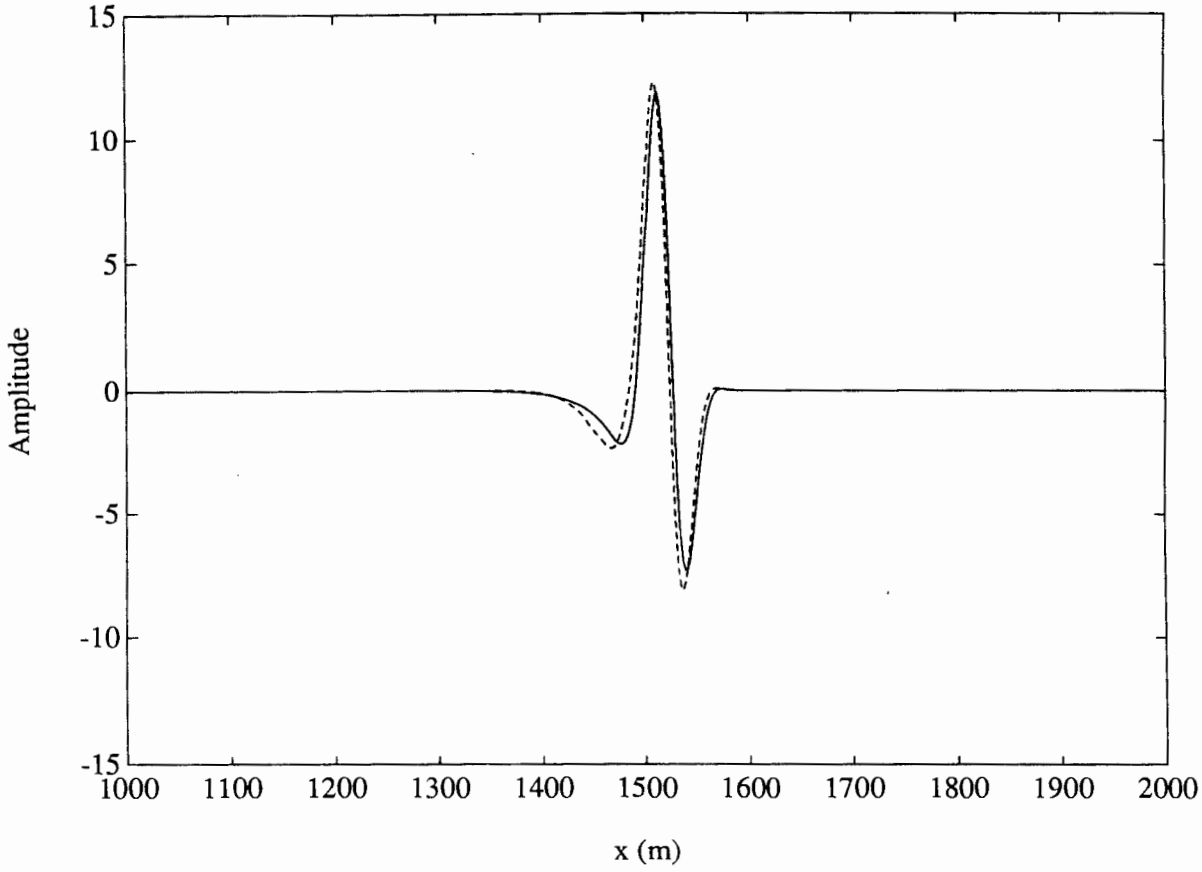
15
10
5
0
-5
-10
-15
Amplitude
1000
1100
1200
1300
1400
1500
1600
1700
1800
1900
2000
x (m)

Figure 20.

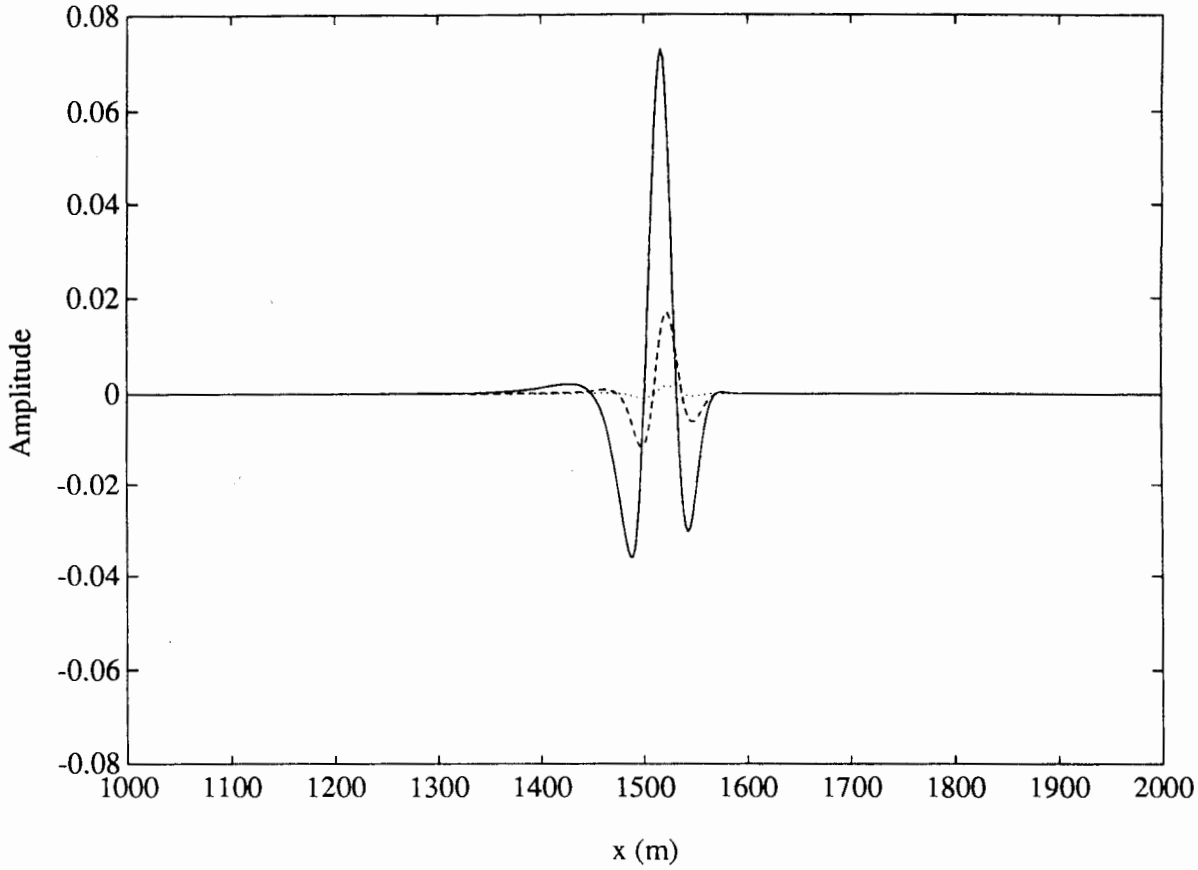
0.08
0.06
0.04
0.02
0
-0.02
-0.04
-0.06
-0.08
Amplitude
1000
1100
1200
1300
1400
1500
1600
1700
1800
1900
2000
x (m)

Figure 21.

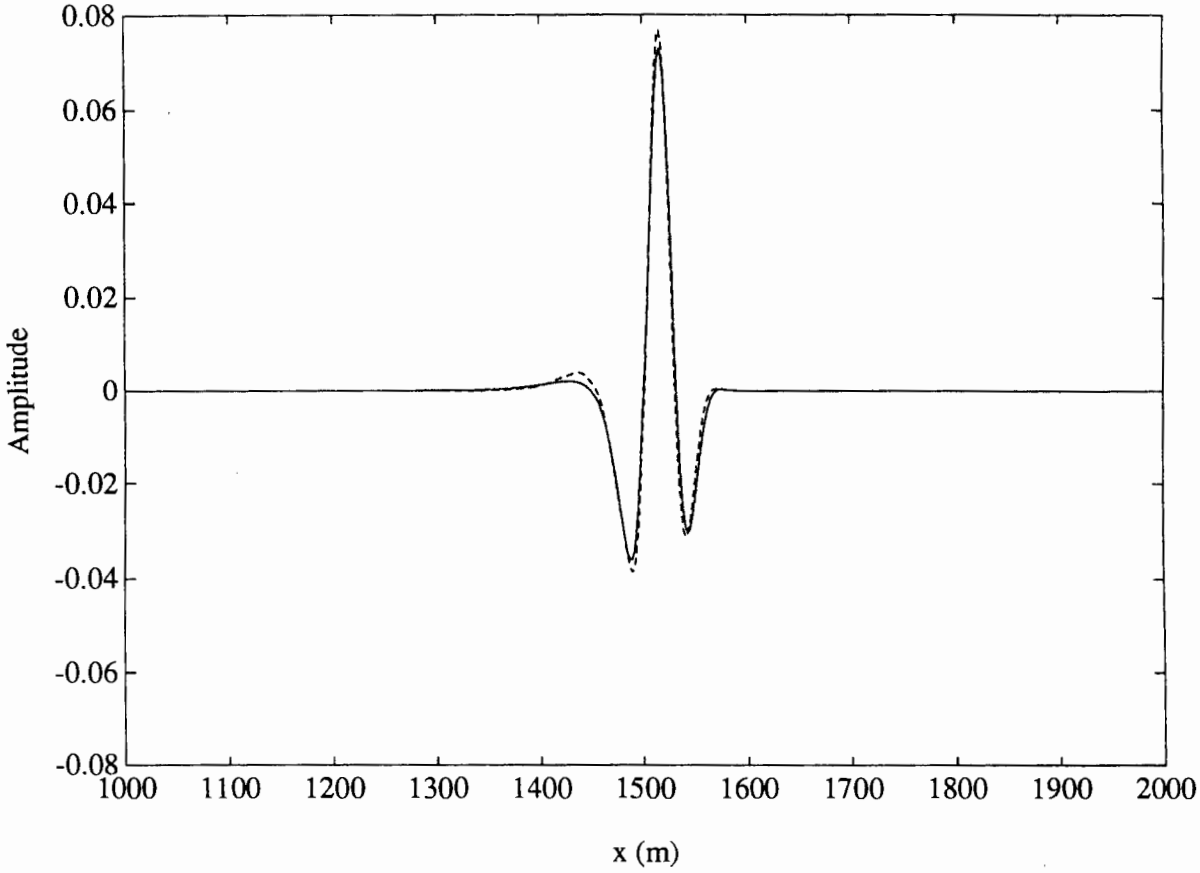
0.08
0.06
0.04
0.02
0
-0.02
-0.04
-0.06
-0.08
Amplitude
1000
1100
1200
1300
1400
1500
1600
1700
1800
1900
2000
x (m)

Figure 22.

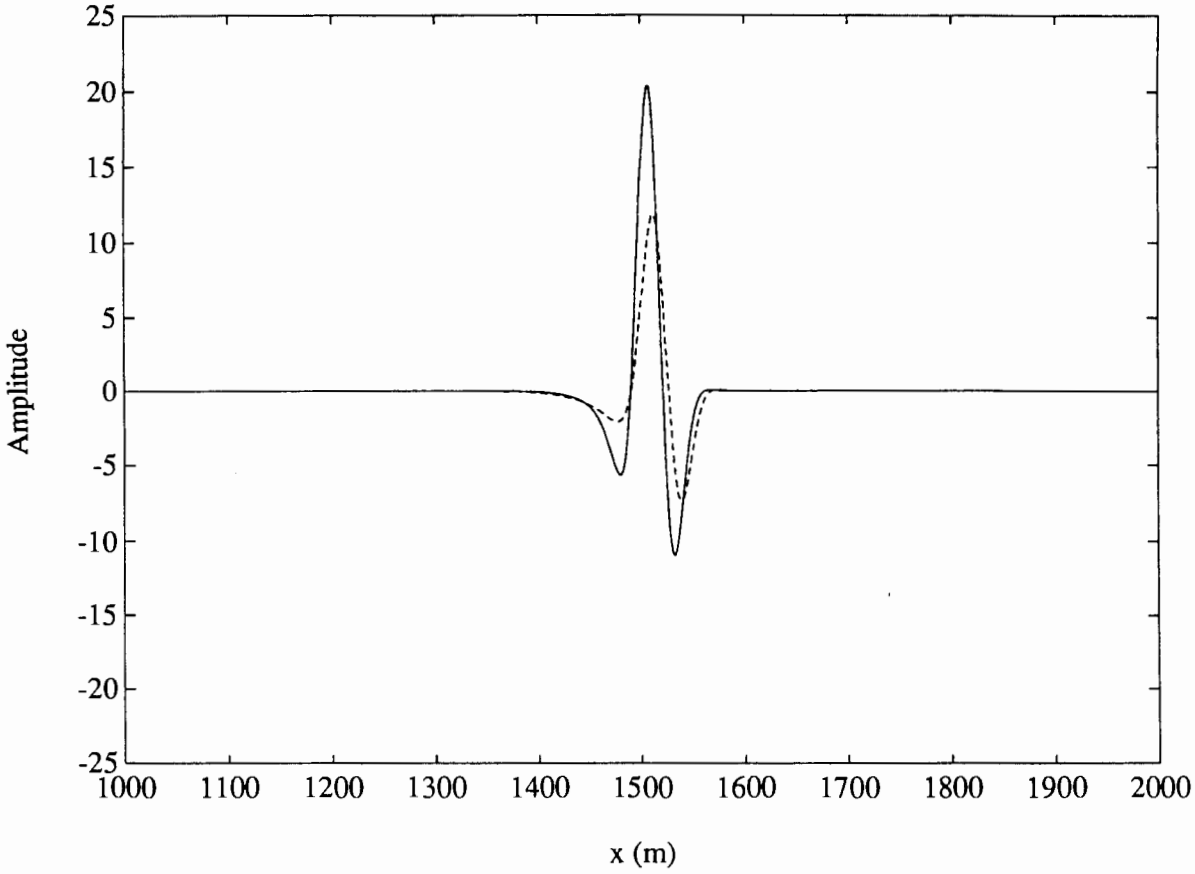
25
20
15
10
5
0
-5
-10
-15
-20
-25
Amplitude
1000
1100
1200
1300
1400
1500
1600
1700
1800
1900
2000
x (m)

Figure 23.

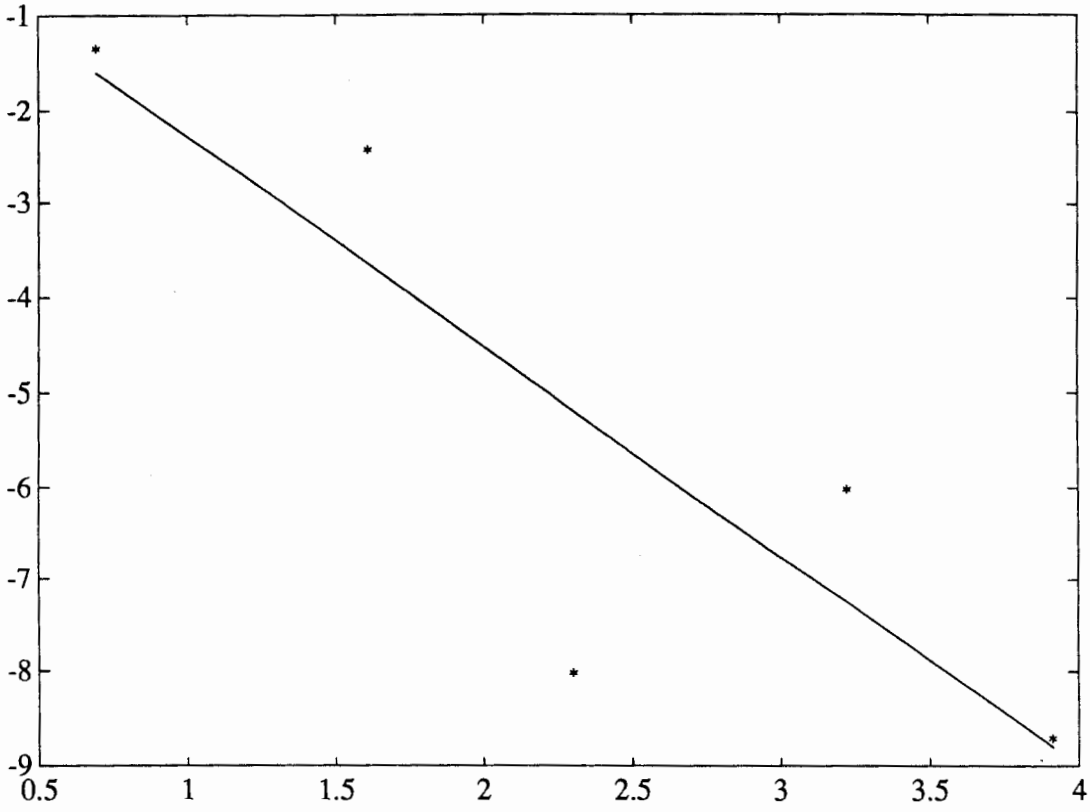
-1
-2
-3
-4
-5
-6
-7
-8
-9
0.5
1
1.5
2
2.5
3
3.5
4
Logarithm of gridpoints/wavelength

Figure 24.

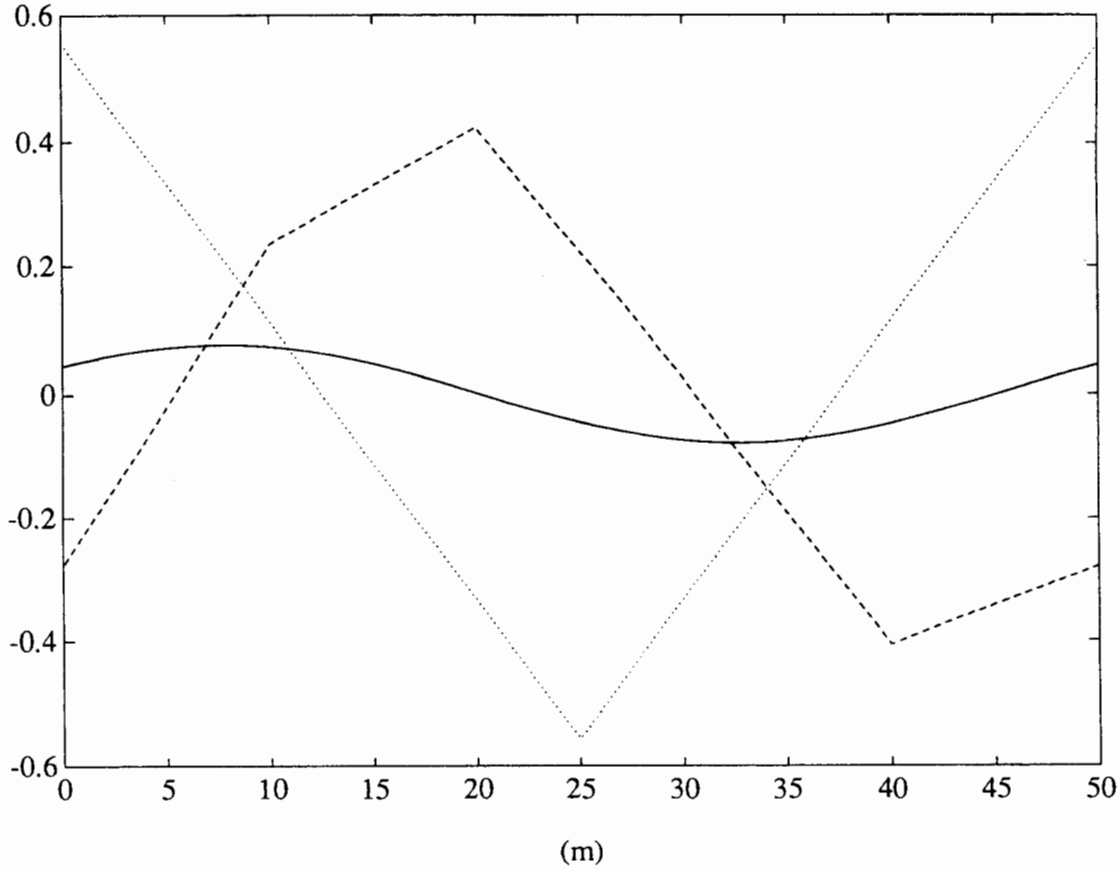

Figure 25.

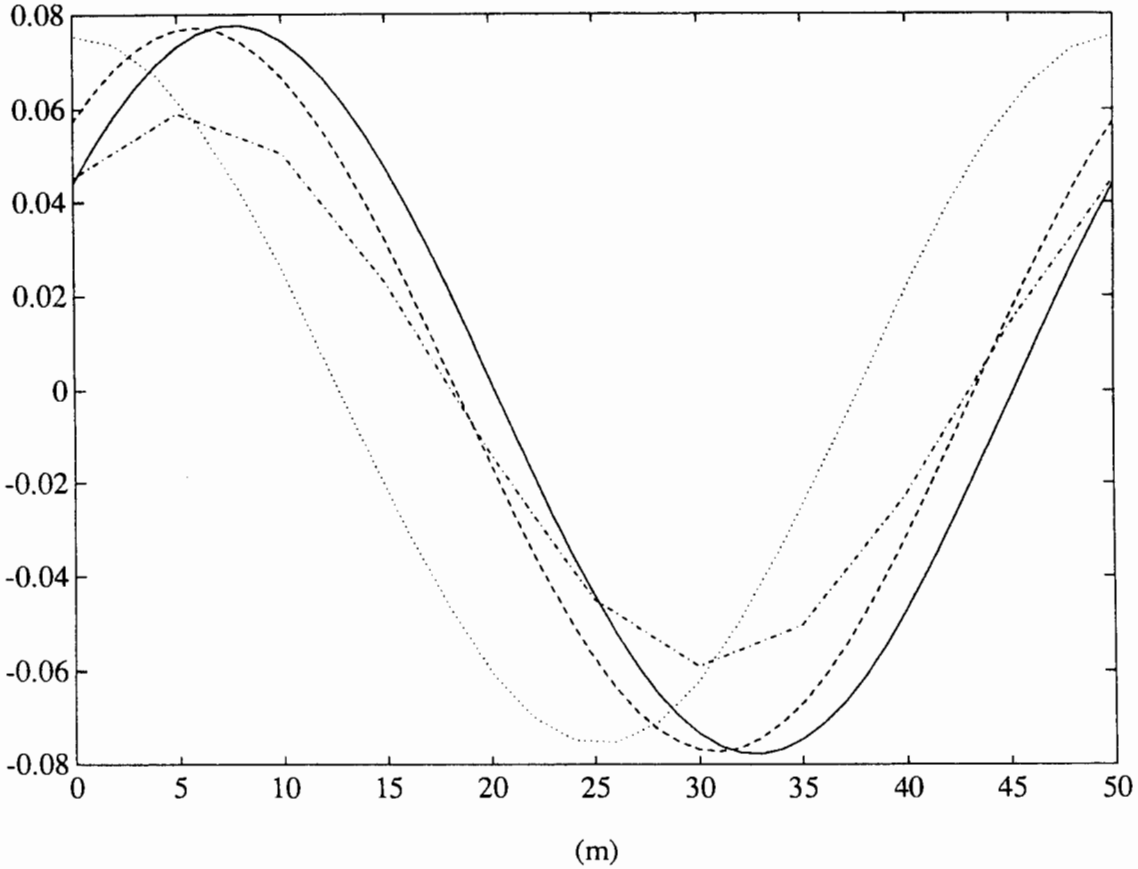

Figure 26.

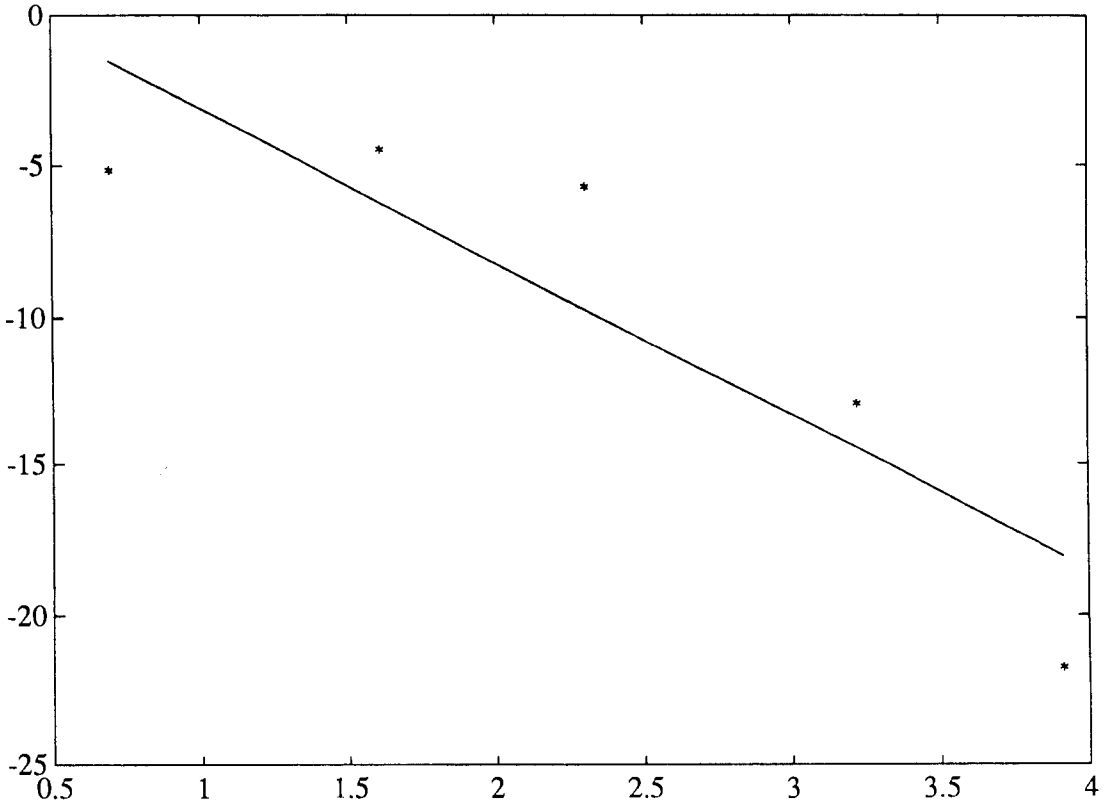
0
-5
-10
-15
-20
-25
0.5
1
1.5
2
2.5
3
3.5
4
Logarithm of gridpoints/wavelength

Figure 27.

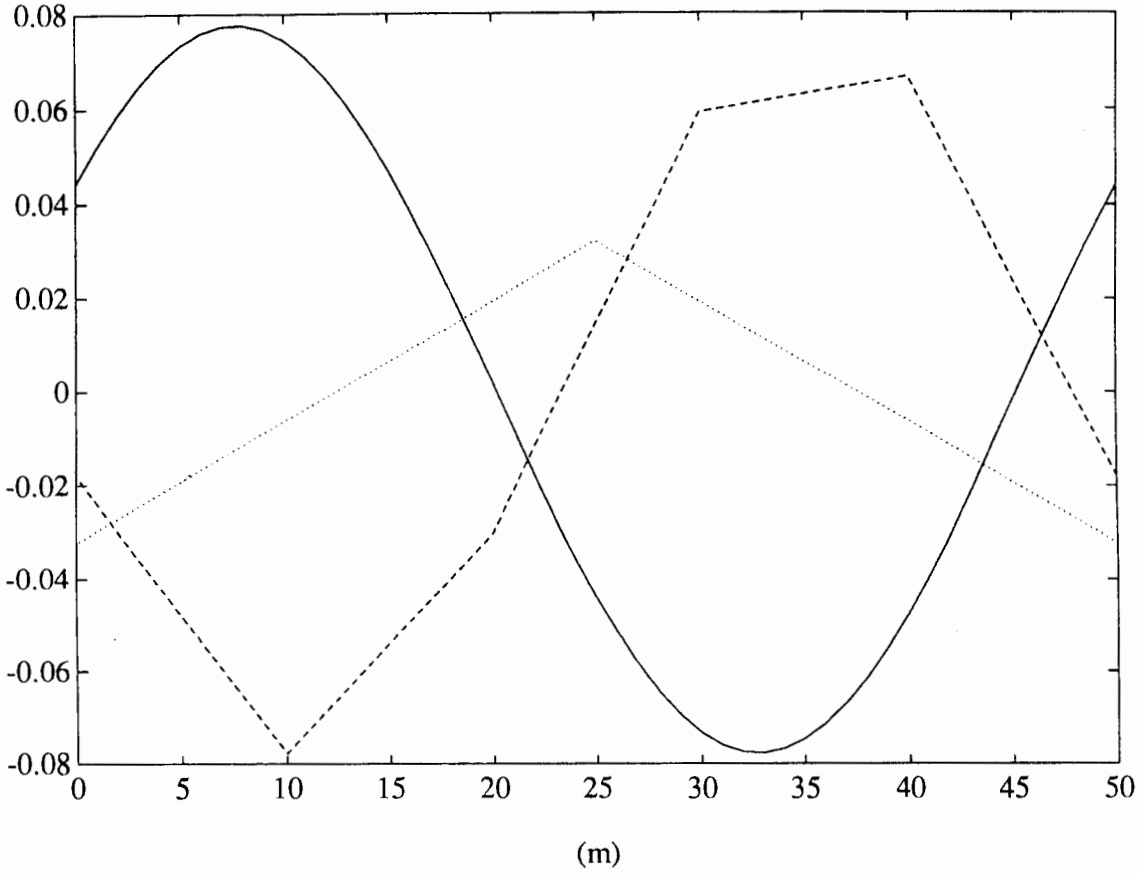

Figure 28.

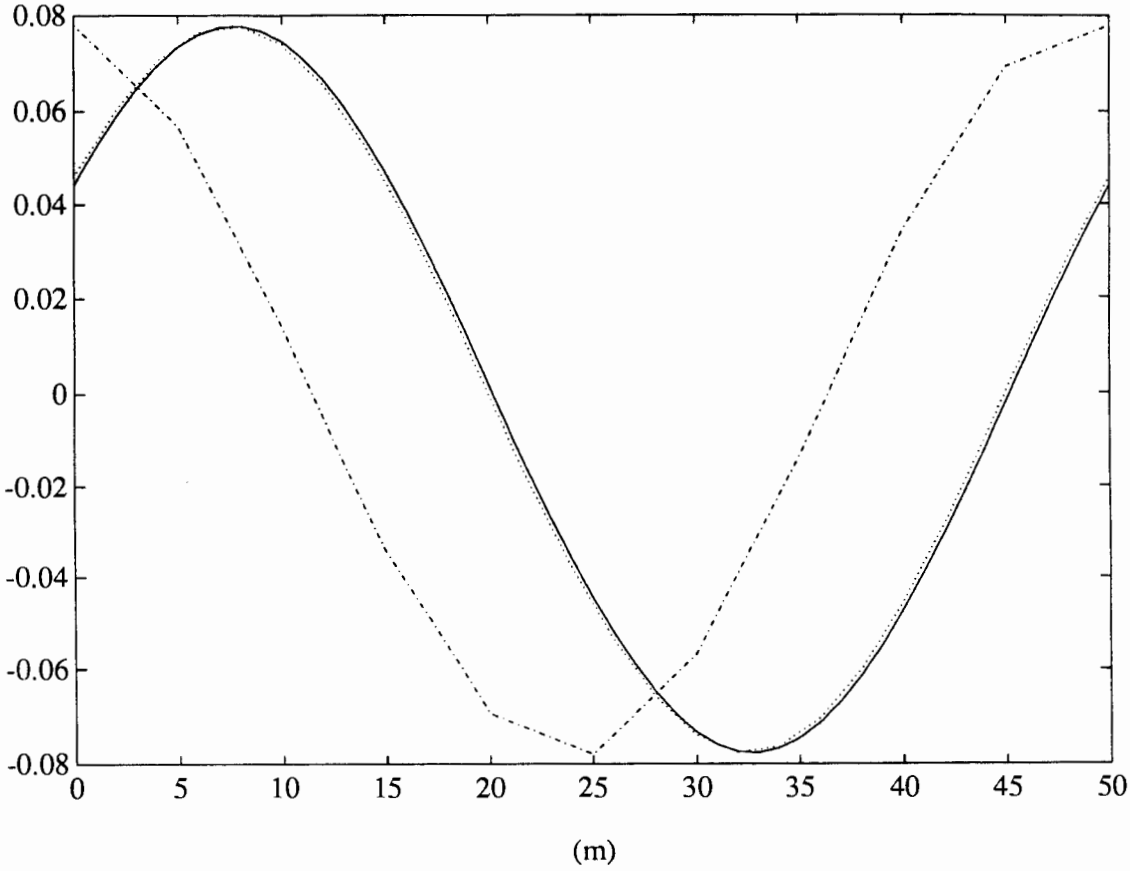

Figure 29.

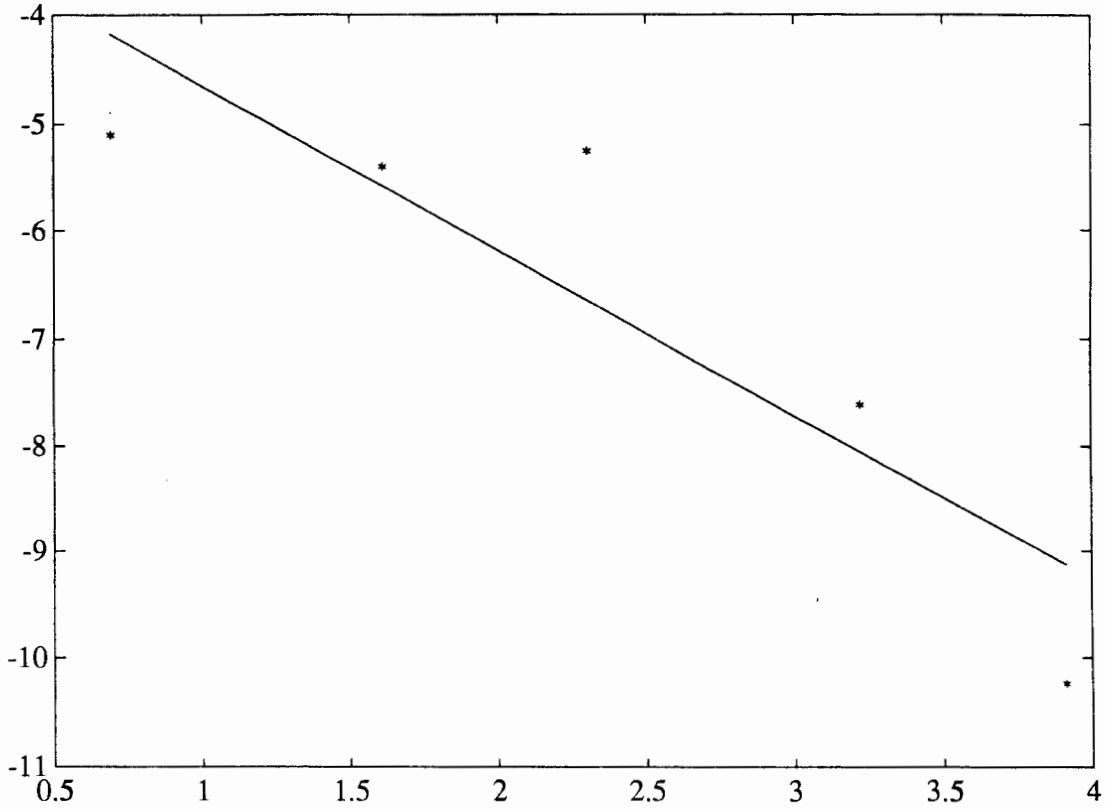
-4
-5
-6
-7
-8
-9
-10
-11
0.5
1
1.5
2
2.5
3
3.5
4
Logarithm of gridpoints/wavelength

Figure 30.

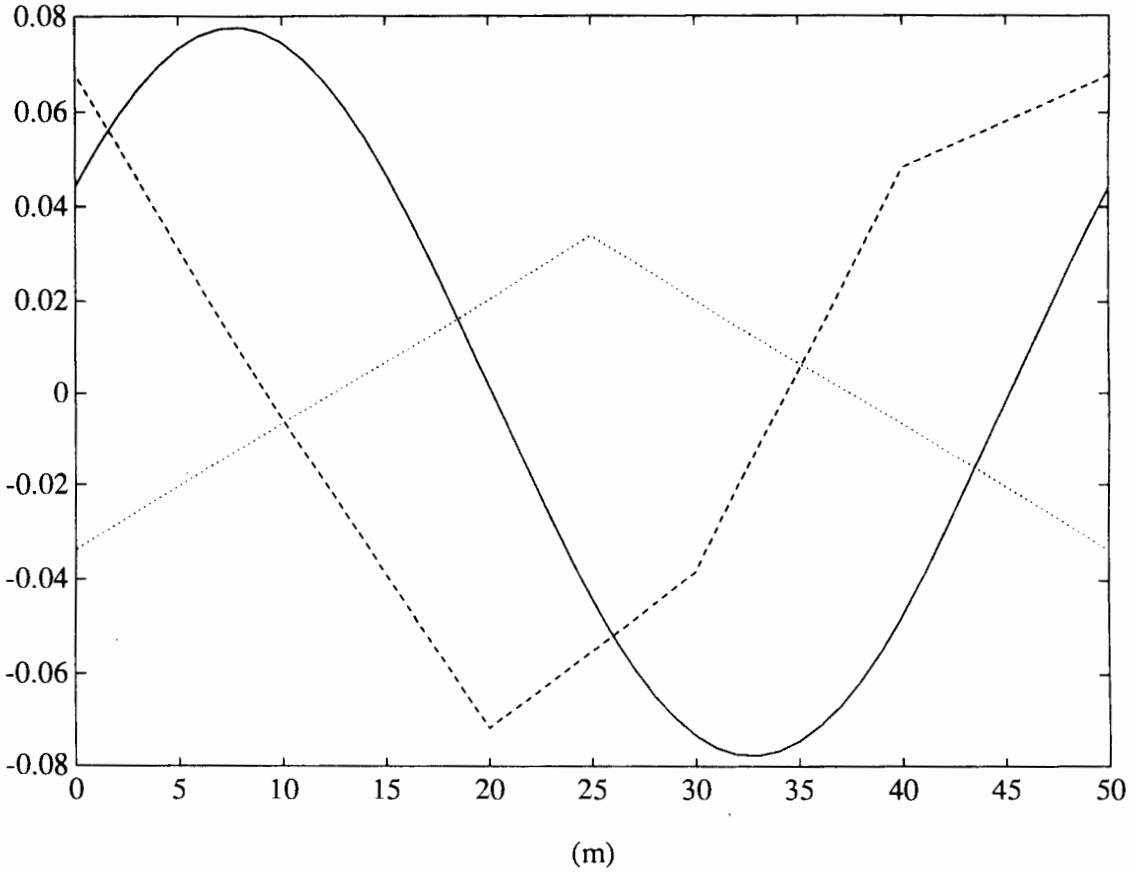

Figure 31.

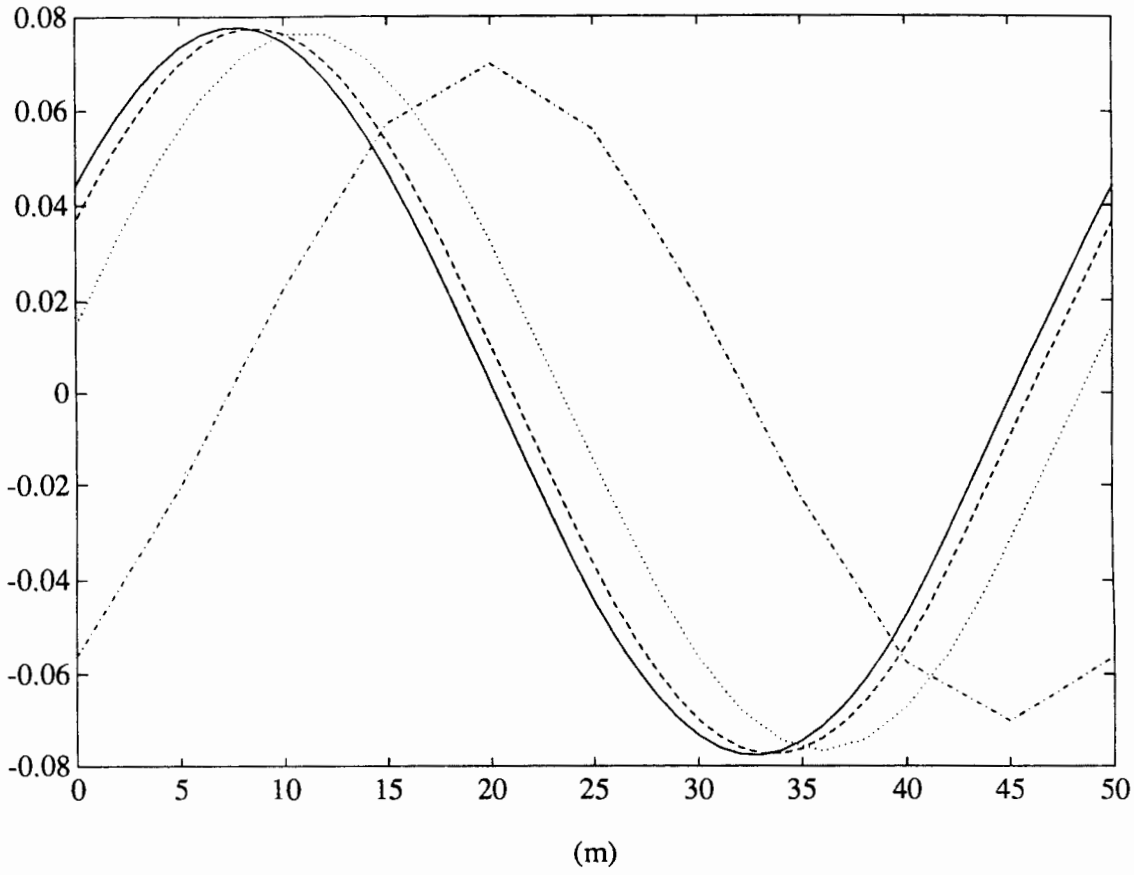

Figure 32.

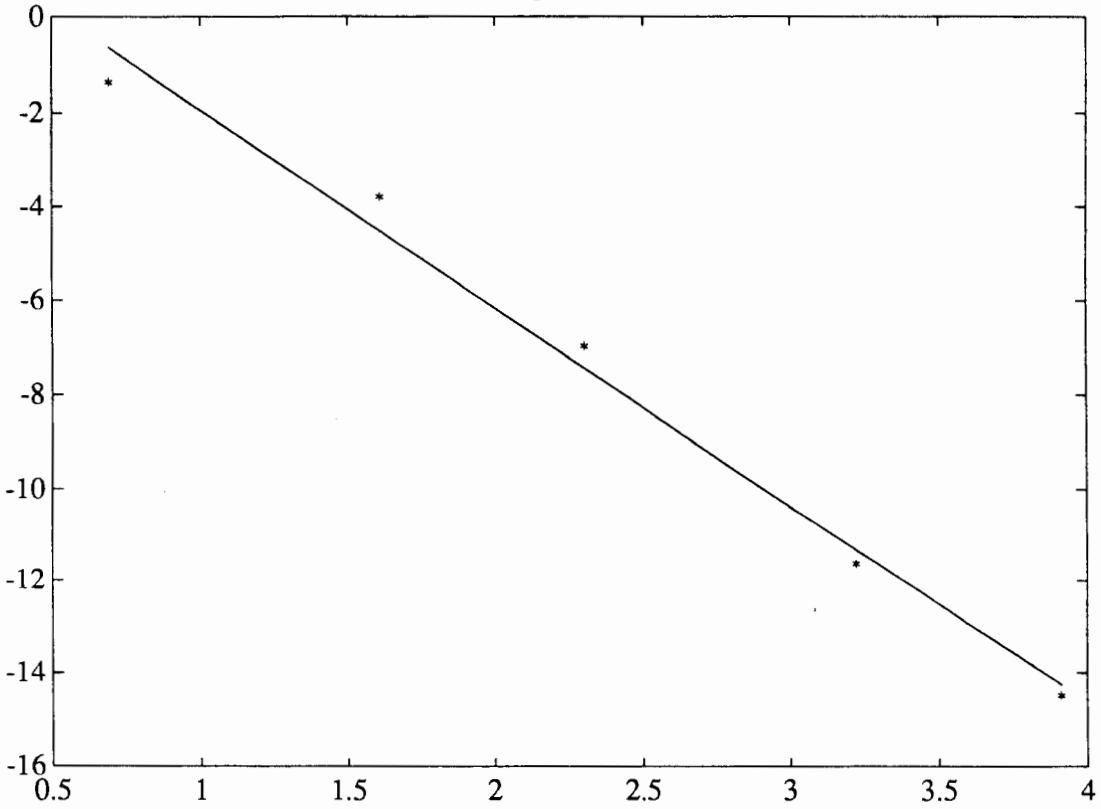
0
-2
-4
-6
-8
-10
-12
-14
-16
0.5
1
1.5
2
2.5
3
3.5
4
Logarithm of gridpoints/wavelength

Figure 33.

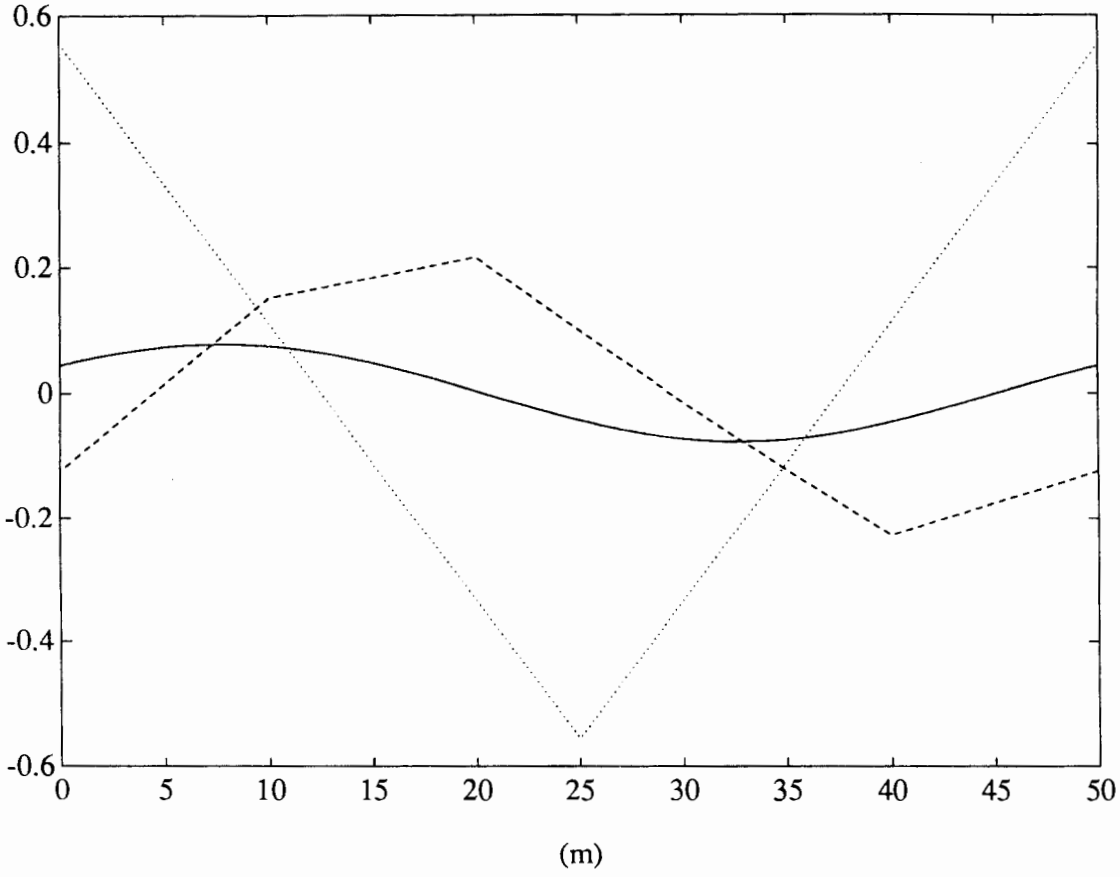

Figure 34.

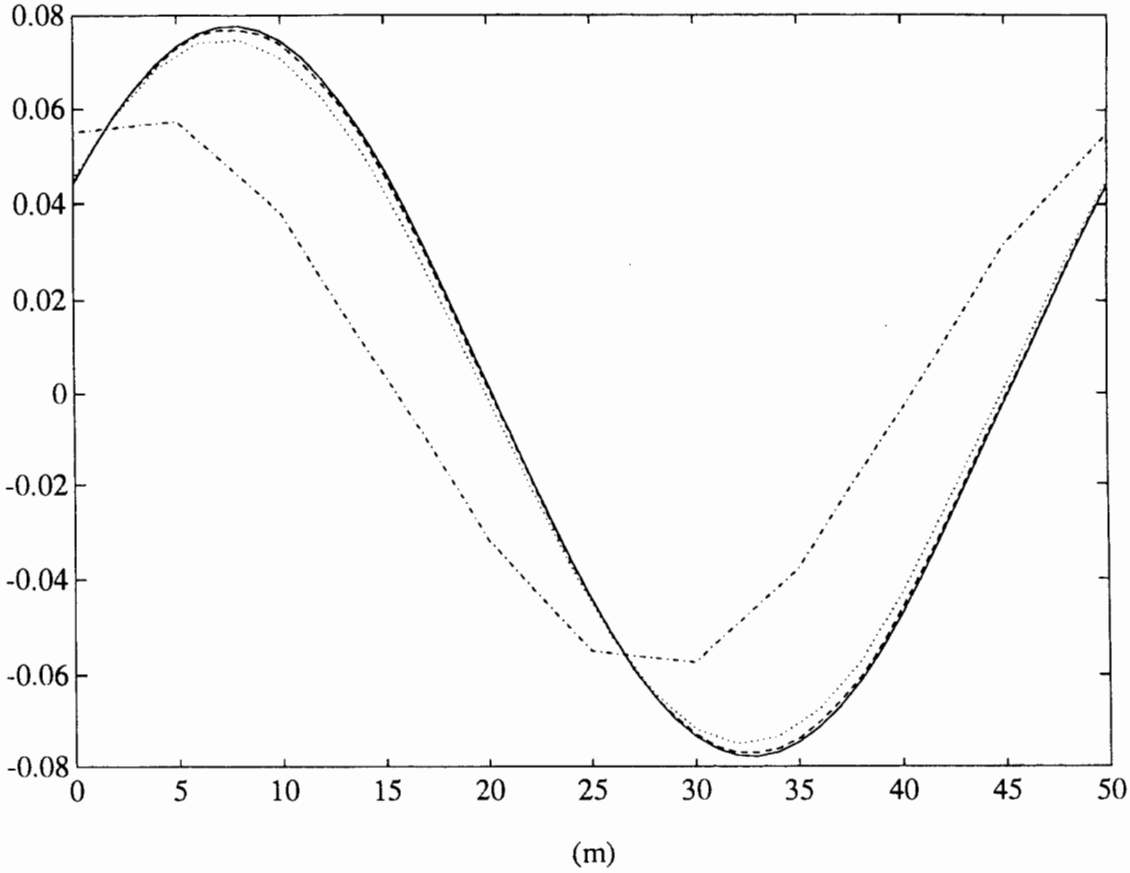

Figure 35.

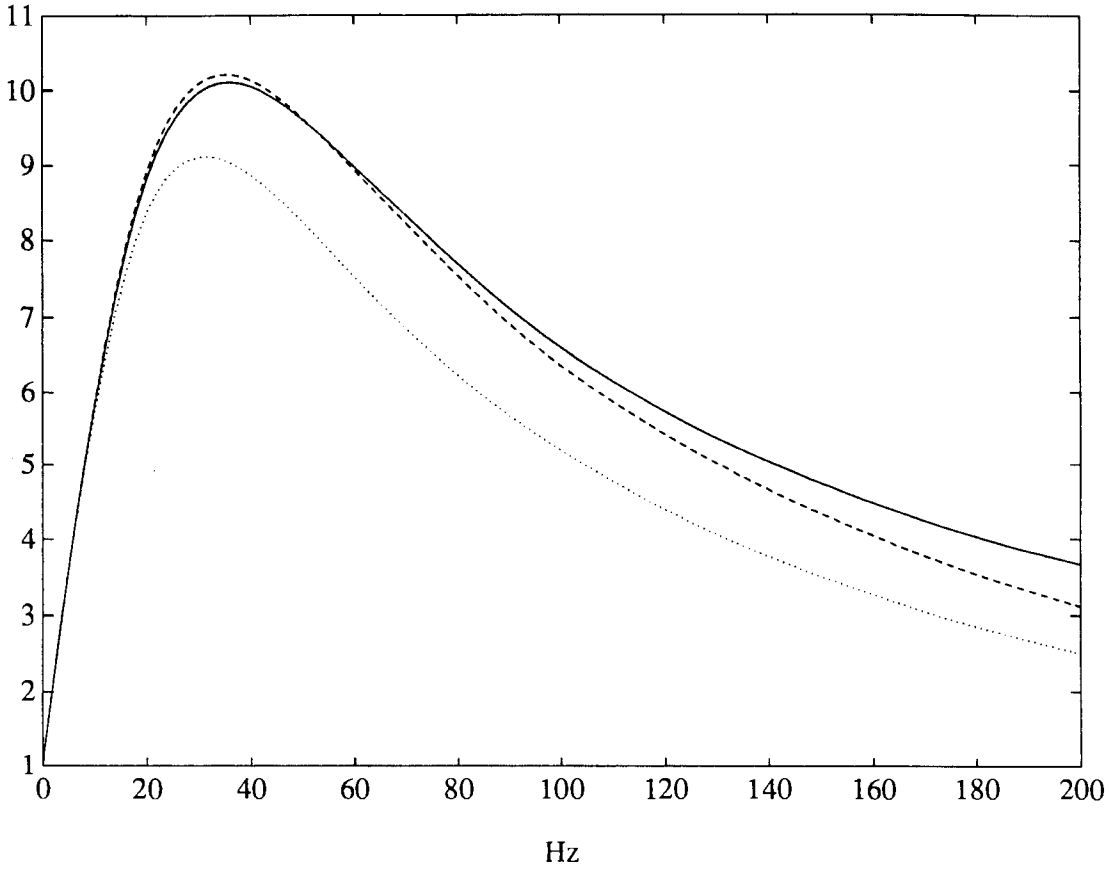

Figure 36.

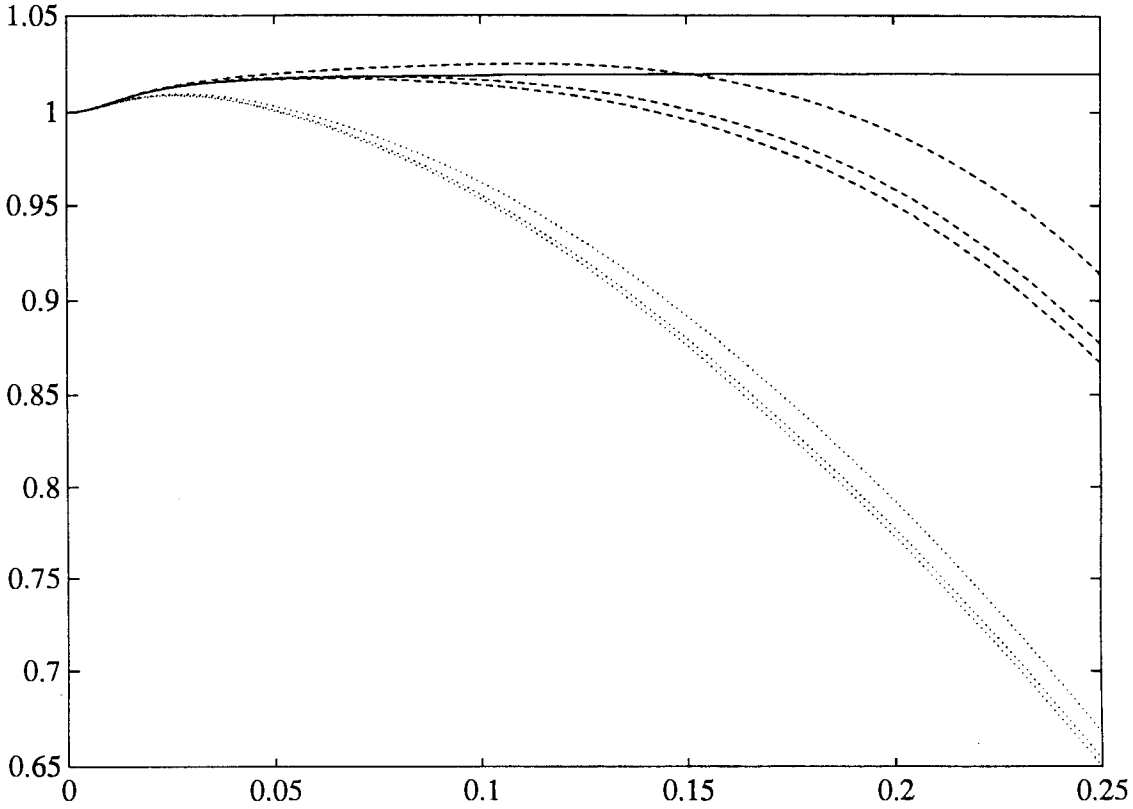

Inverse of gridpoints/wavelength, 0.25 <=> 500 Hz

Figure 37.

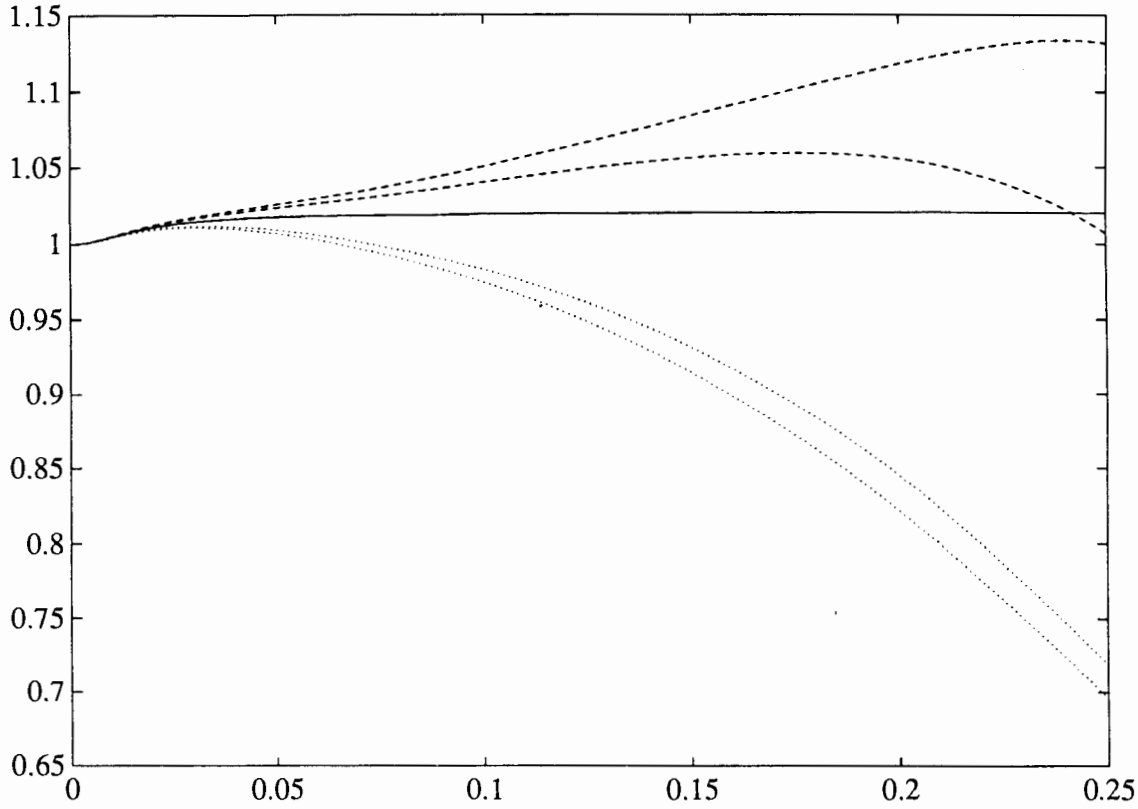

Inverse of gridpoints/wavelength, 0.25 <=> 500 Hz

Figure 38.

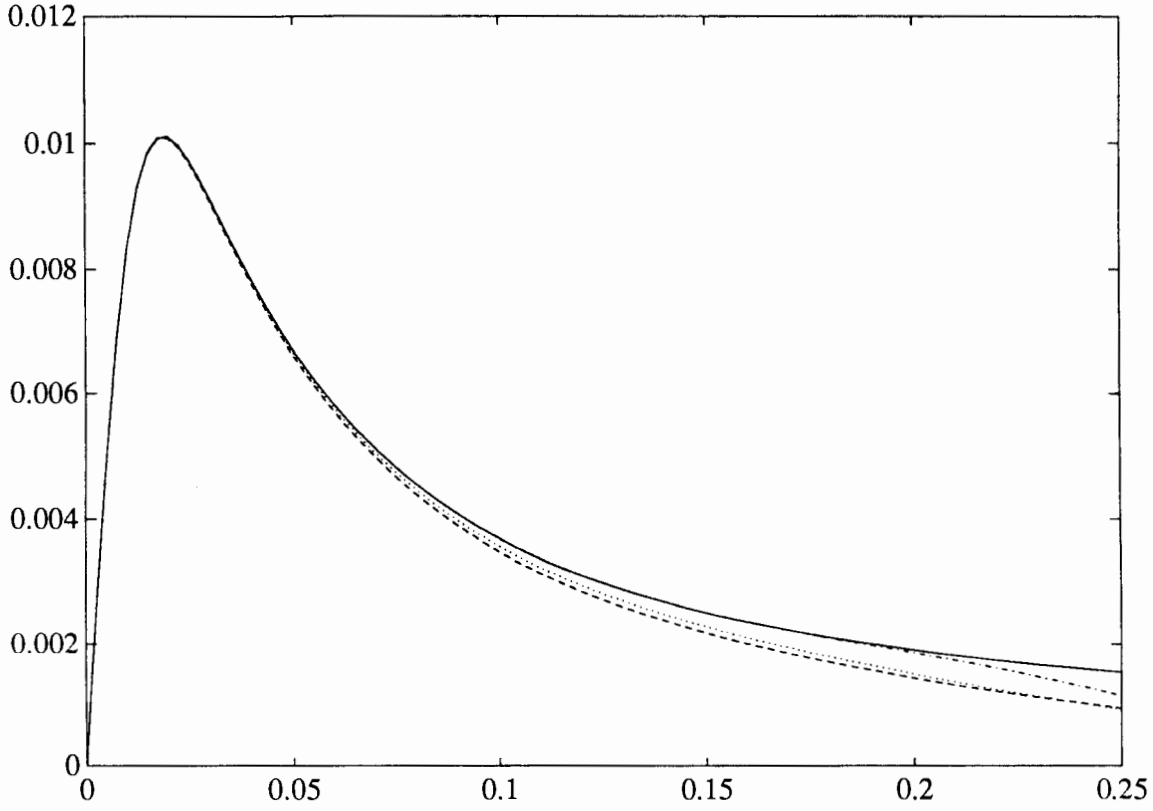

Inverse of gridpoints/wavelength, 0.25 <=> 500 Hz

Figure 39.

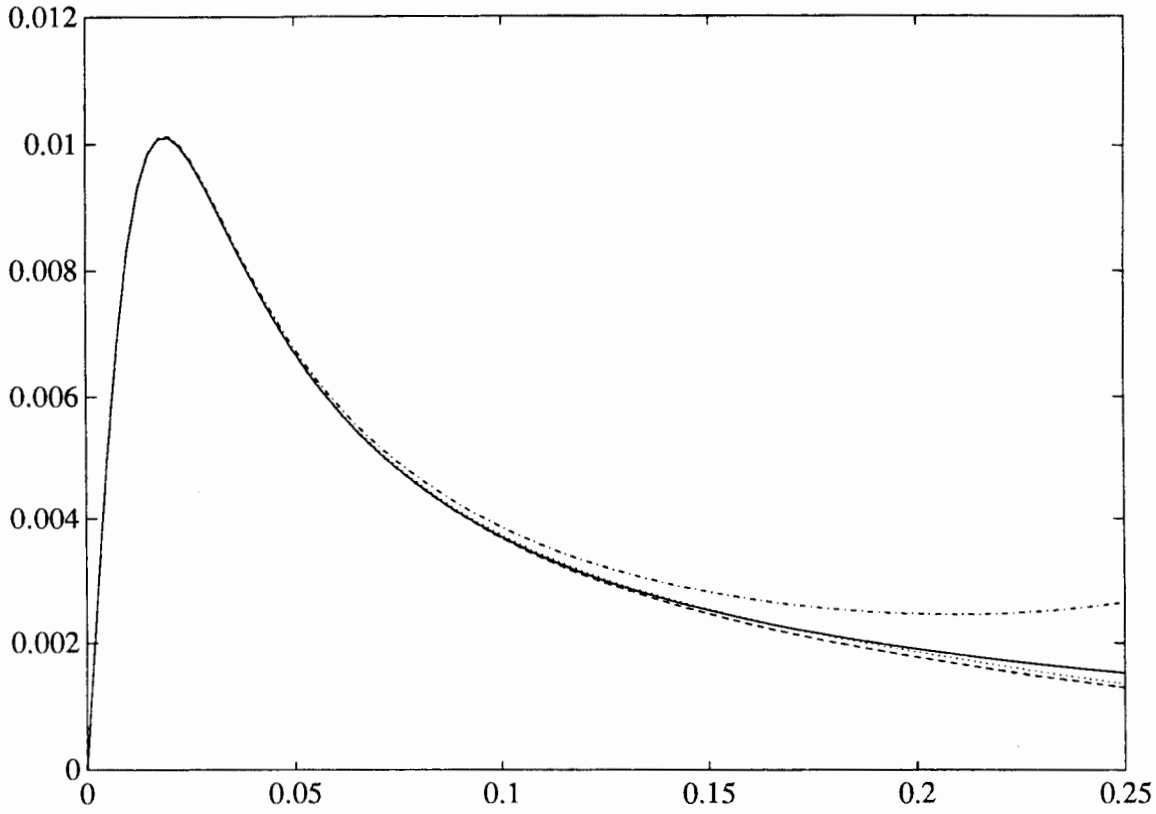

Inverse of gridpoints/wavelength, 0.25 <=> 500 Hz

Figure 40.

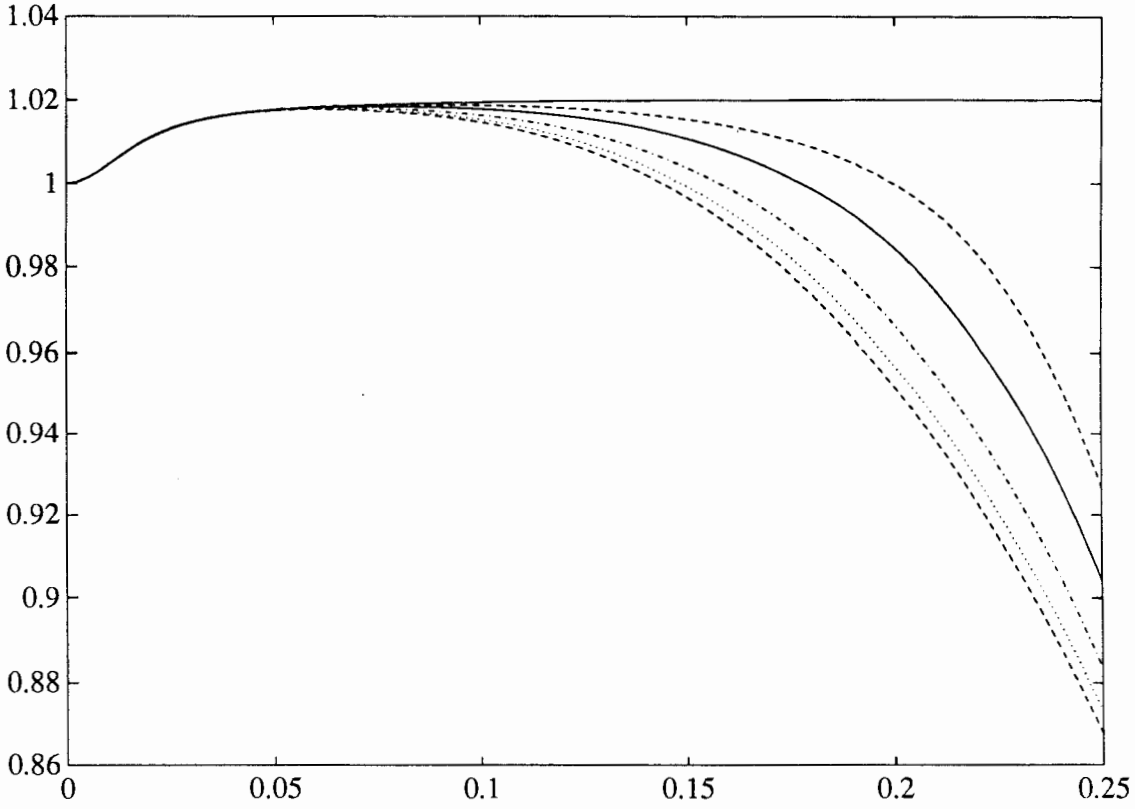

Inverse of gridpoints/wavelength, 0.25 <=> 500 Hz

Figure 41.

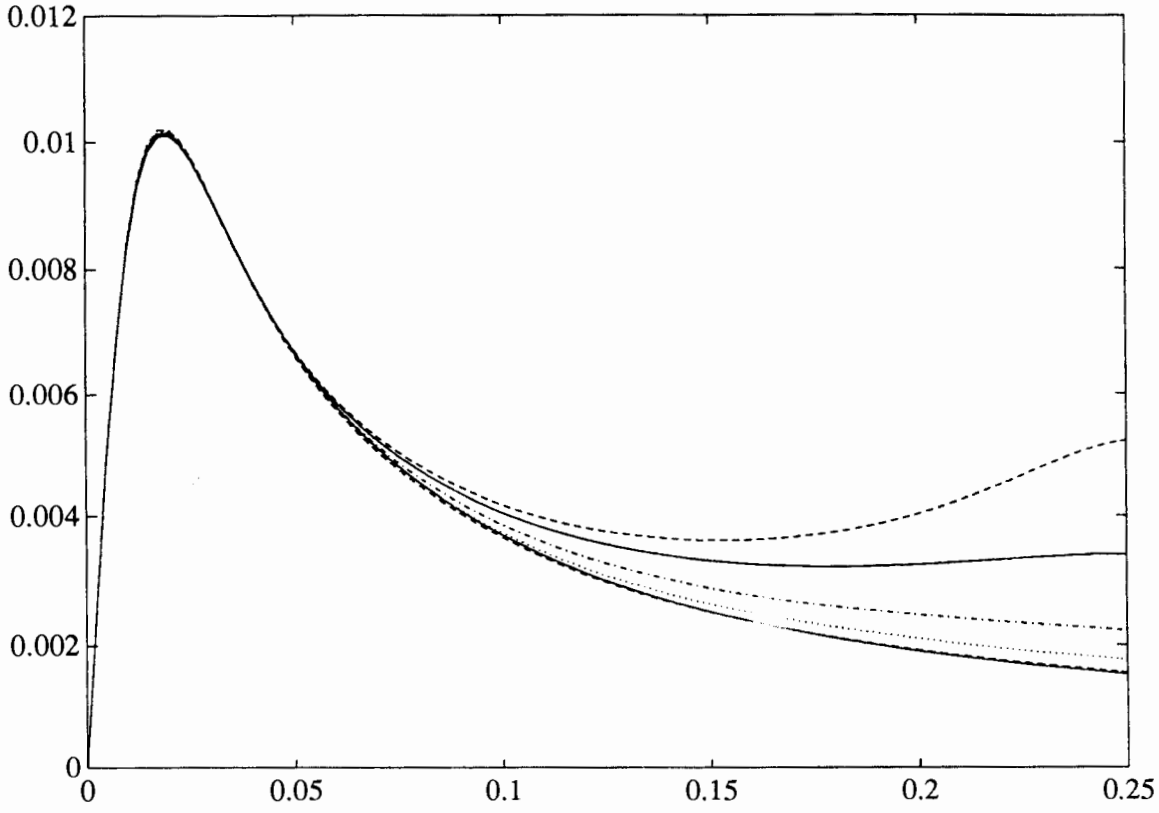

Inverse of gridpoints/wavelength, 0.25 <=> 500 Hz

Figure 42.

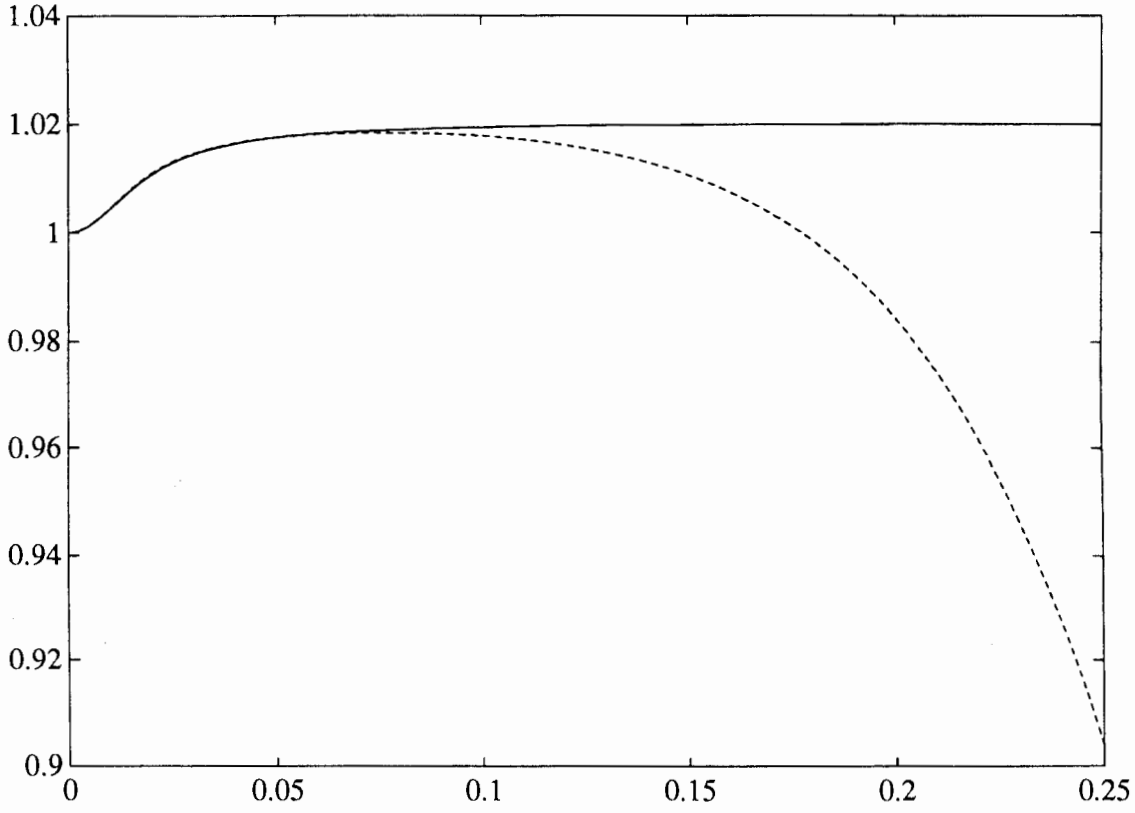

Inverse of gridpoints/wavelength, 0.25 <=> 500 Hz

Figure 43.

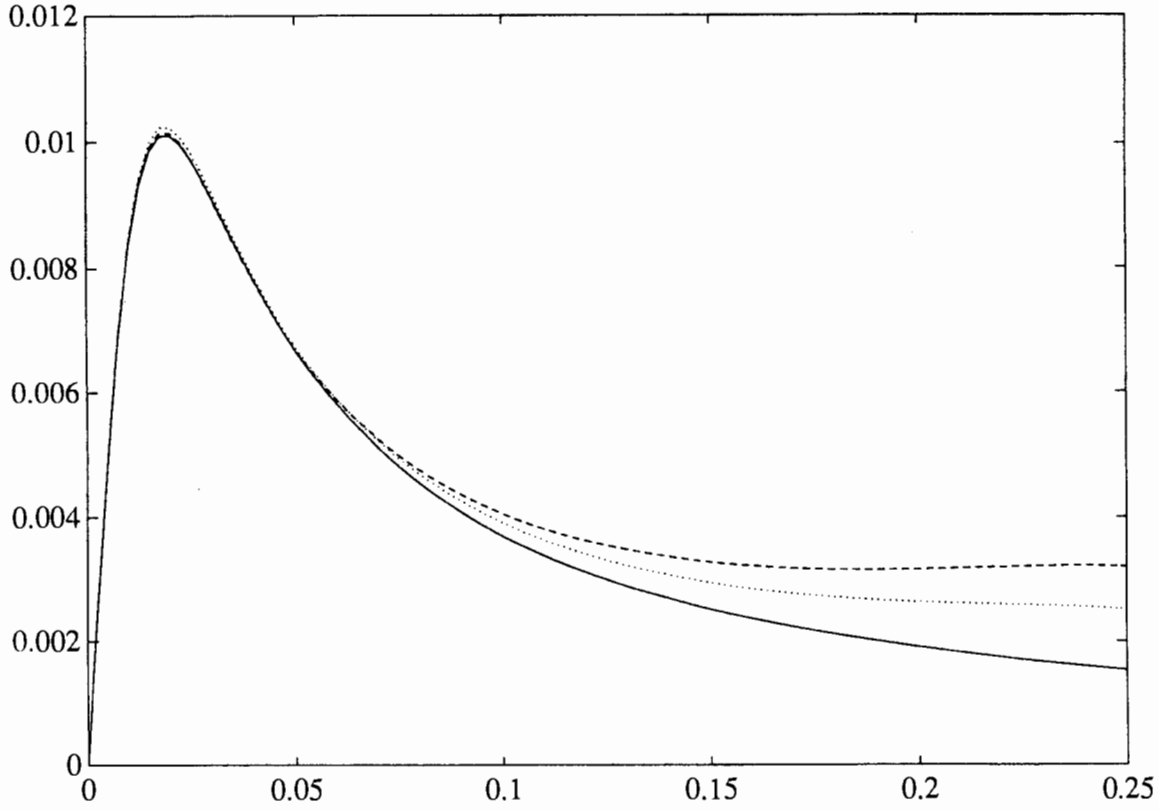

Inverse of gridpoints/wavelength, 0.25 <=> 500 Hz

Figure 44.

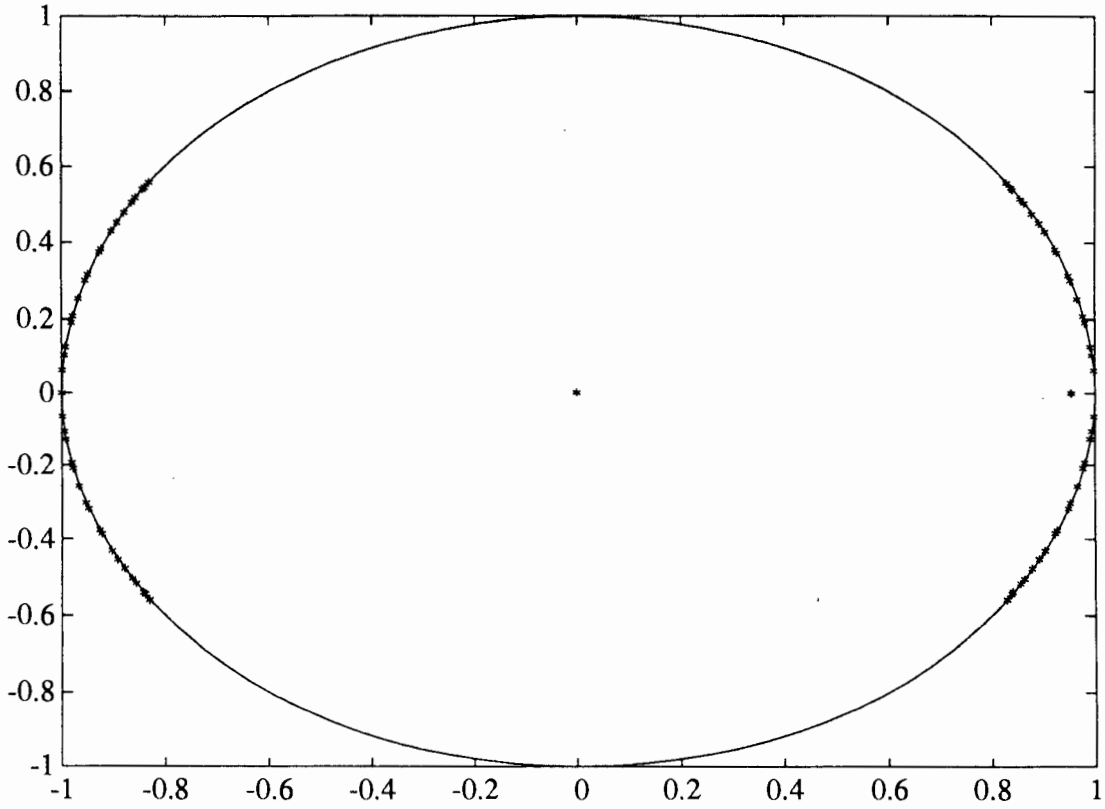

Figure 45.

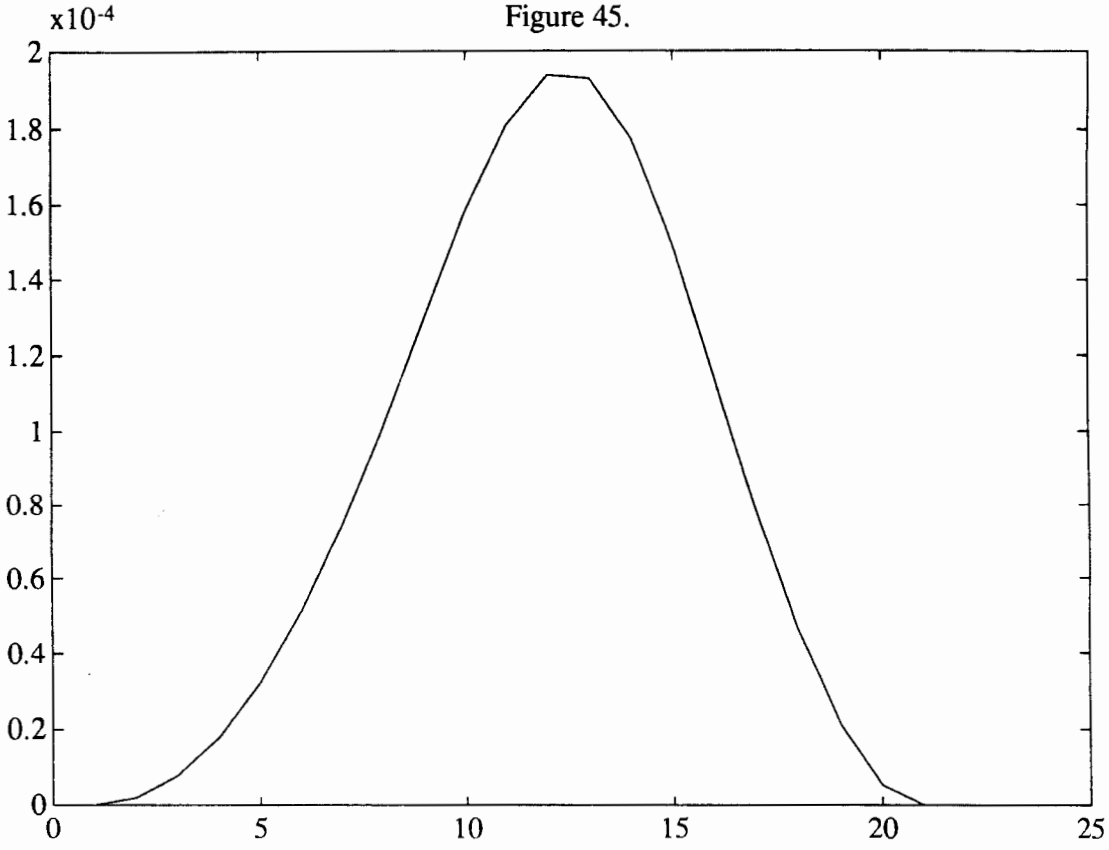

Figure 46.

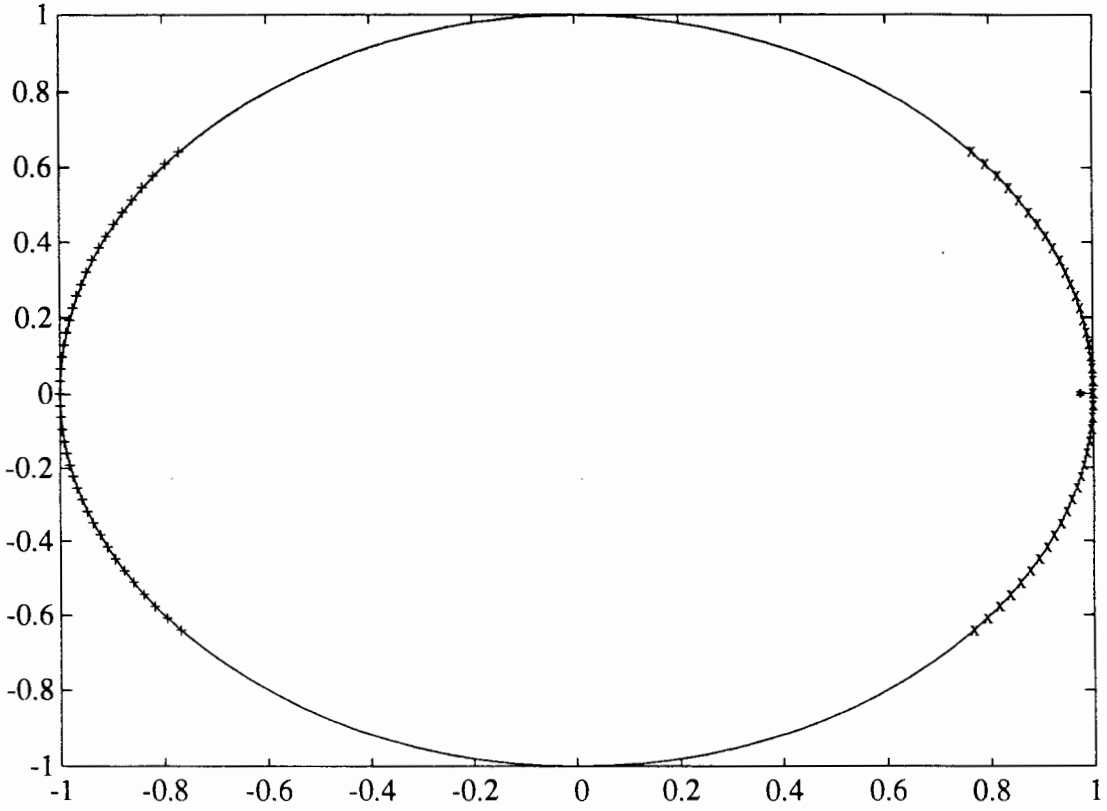

Figure 47.

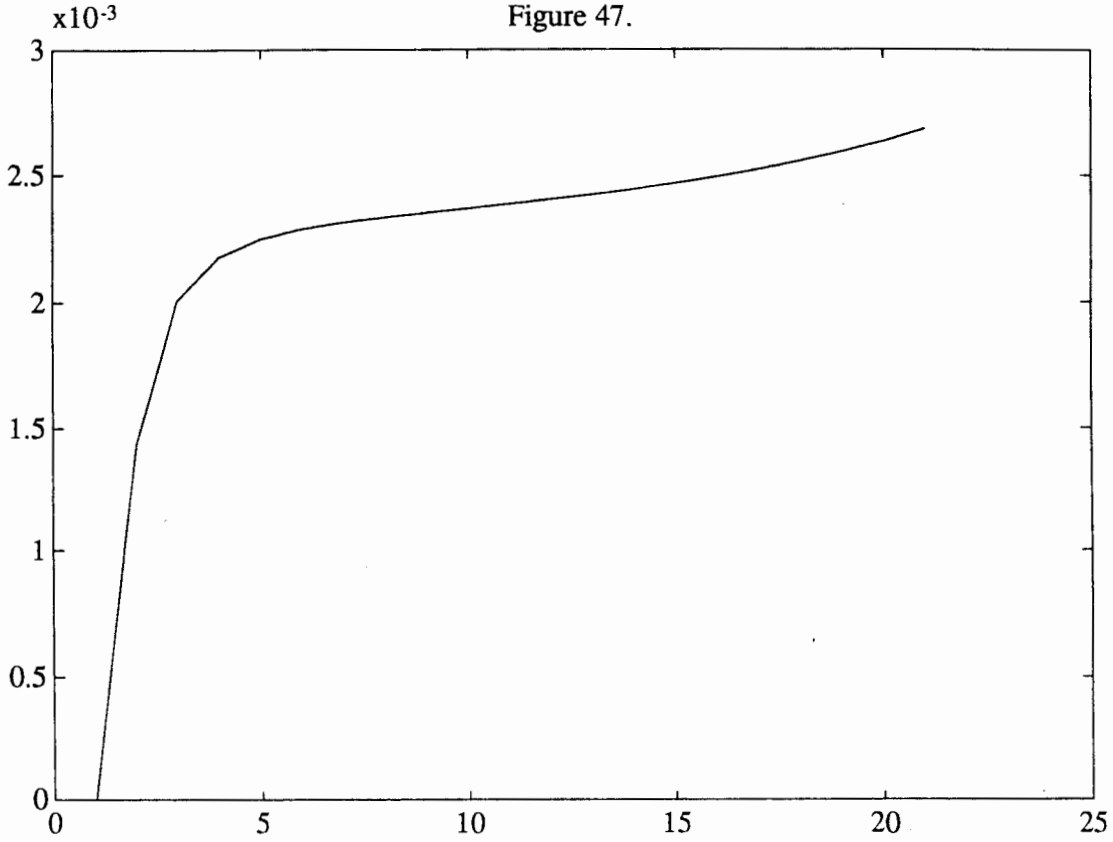

Figure 48.

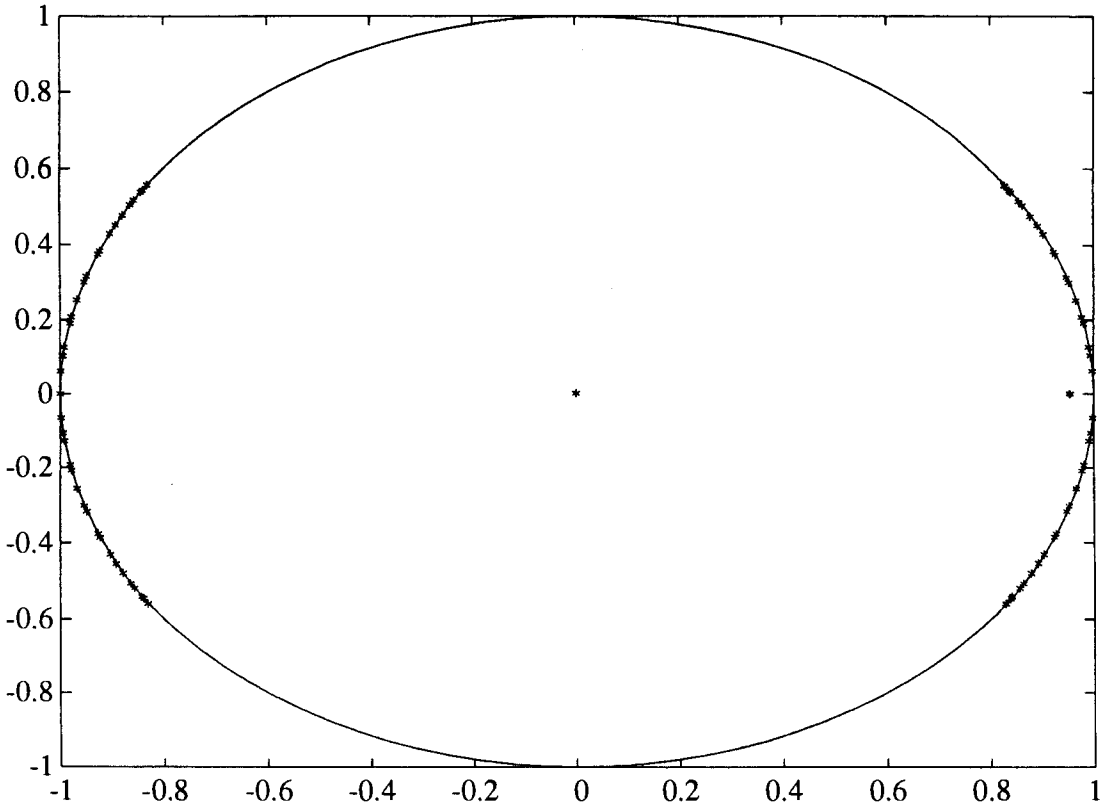

Figure 49.

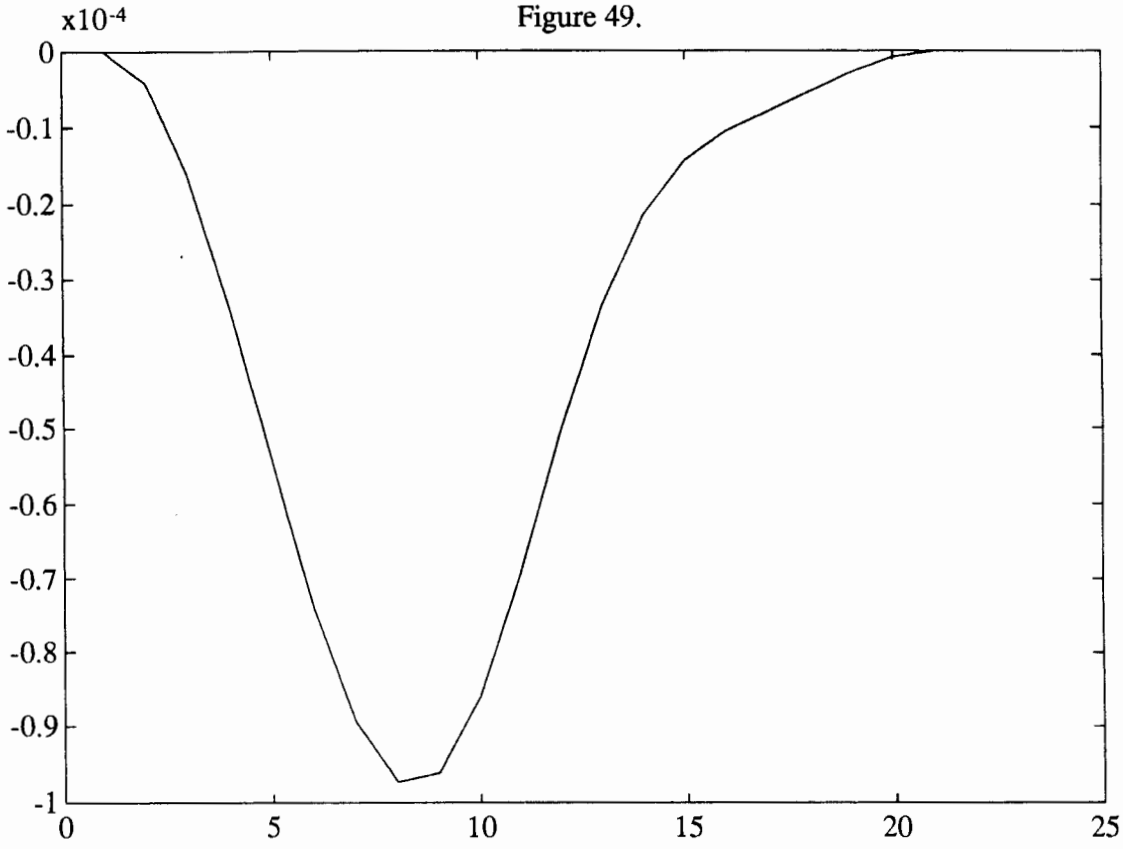

Figure 50.

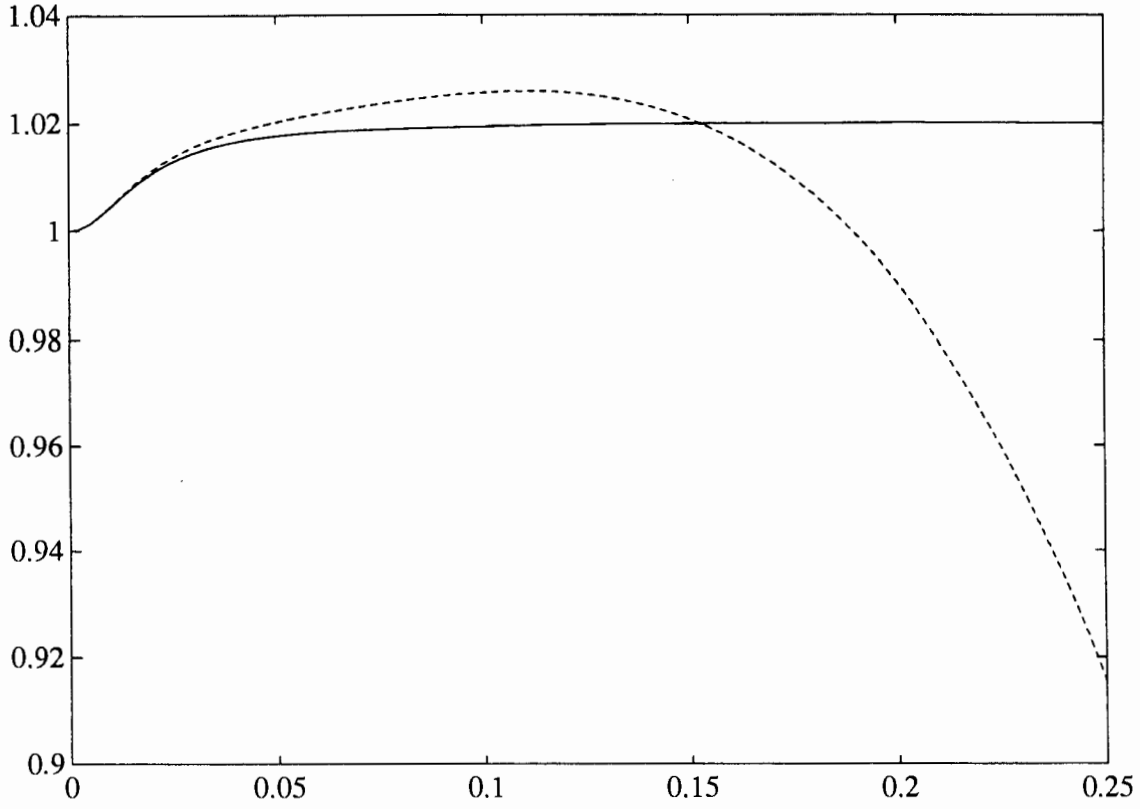

Inverse of gridpoints/wavelength, 0.25 <=> 500 Hz

Figure 51.

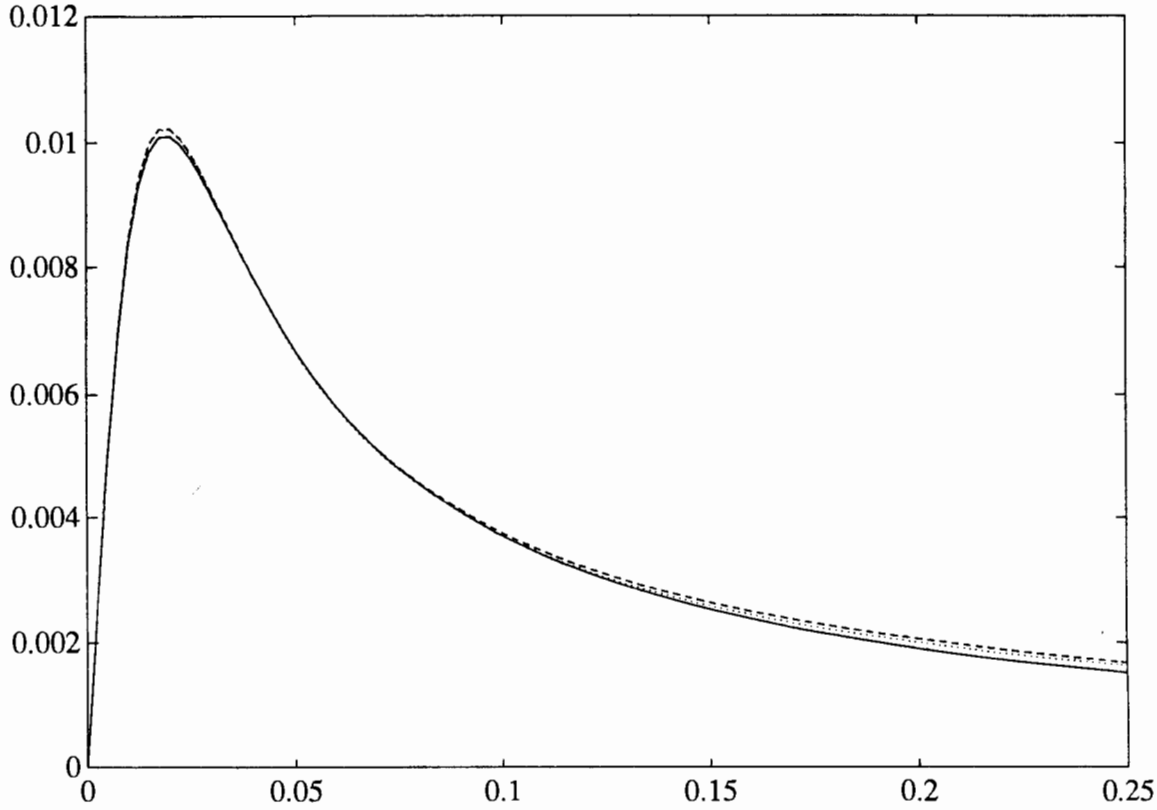

Inverse of gridpoints/wavelength, 0.25 <=> 500 Hz

Figure 52.

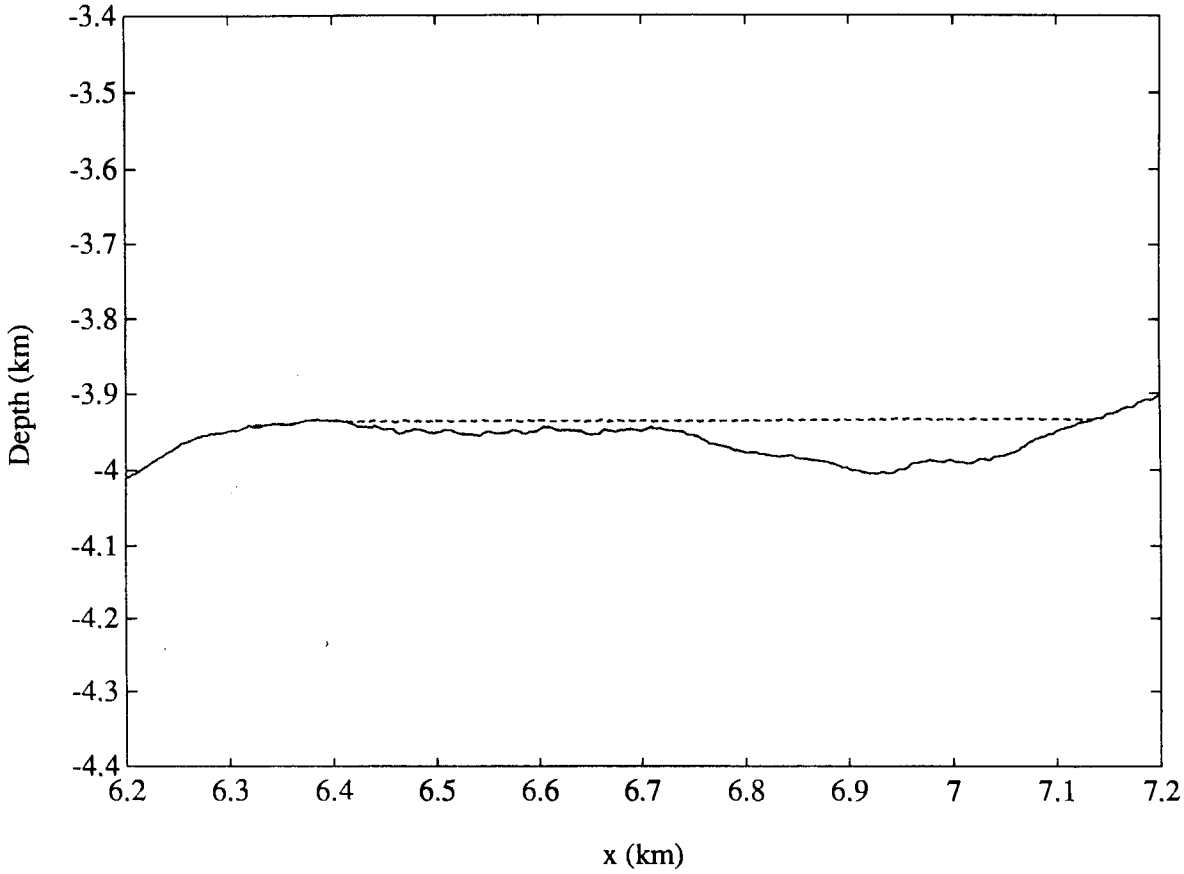
-3.4
-3.5
-3.6
-3.7
-3.8
-3.9
-4
-4.1
-4.2
-4.3
-4.4
Depth (km)
6.2
6.3
6.4
6.5
6.6
6.7
6.8
6.9
7
7.1
7.2
x (km)

Figure 53 a.

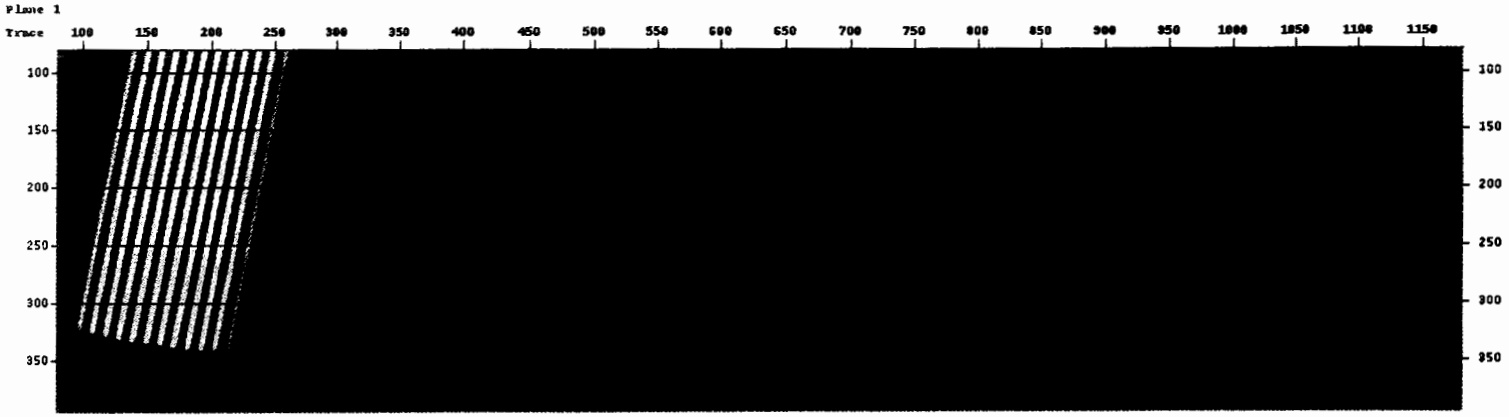
Plane 1
Trace
100
150
200
250
300
350
400
450
500
550
600
650
700
750
800
850
900
950
1000
1050
1100
1150
100
150
200
250
300
350

Figure 53 b.

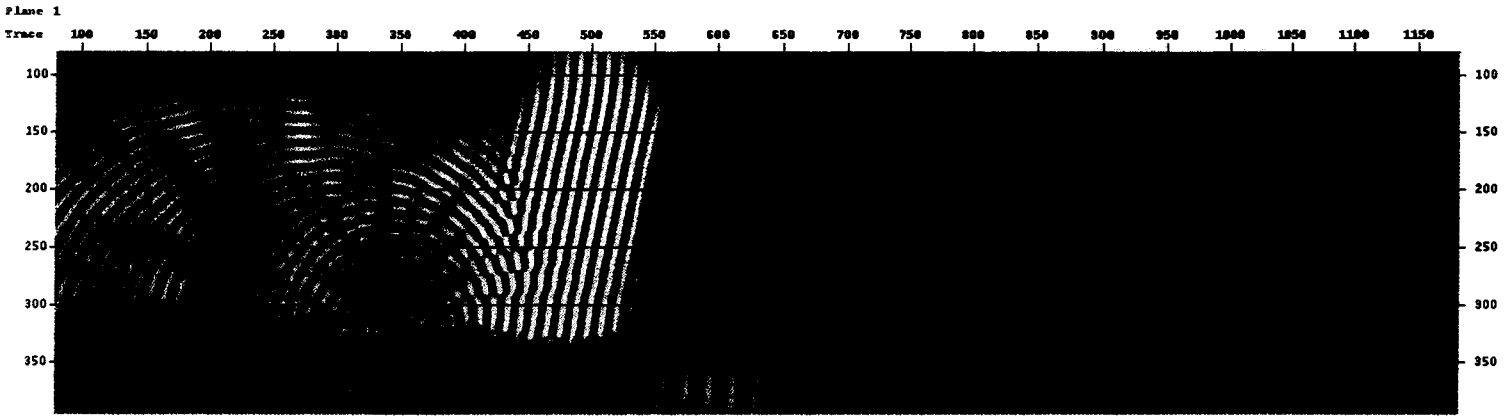
Plane 1
Trace
100 150 200 250 300 350 400 450 500 550 600 650 700 750 800 850 900 950 1000 1050 1100 1150
100
150
200
250
300
350

Figure 53 c.

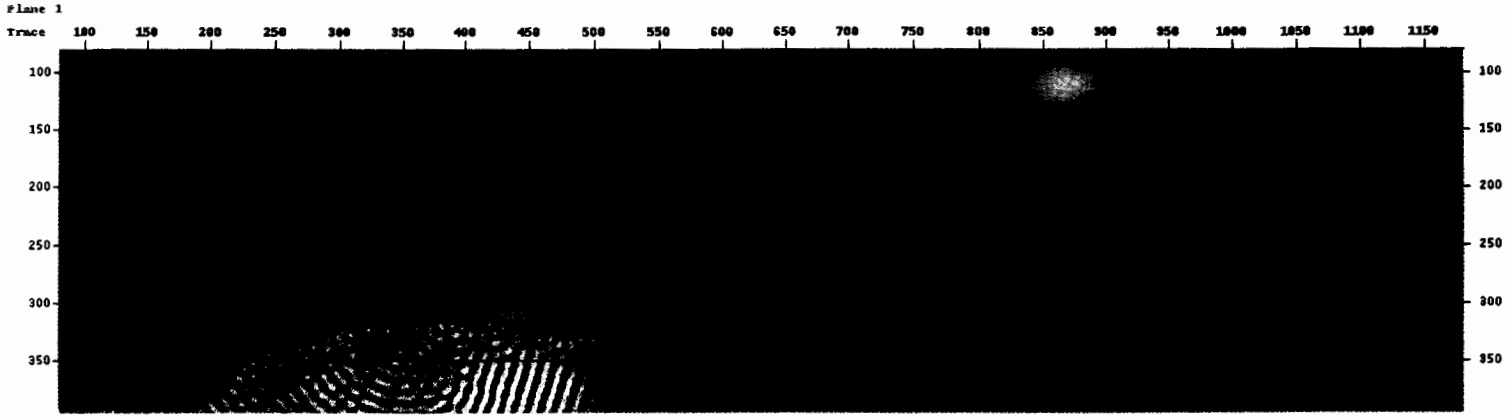
Plane 1
Trace
100
150
200
250
300
350
400
450
500
550
600
650
700
750
800
850
900
950
1000
1050
1100
1150

Figure 53 d.

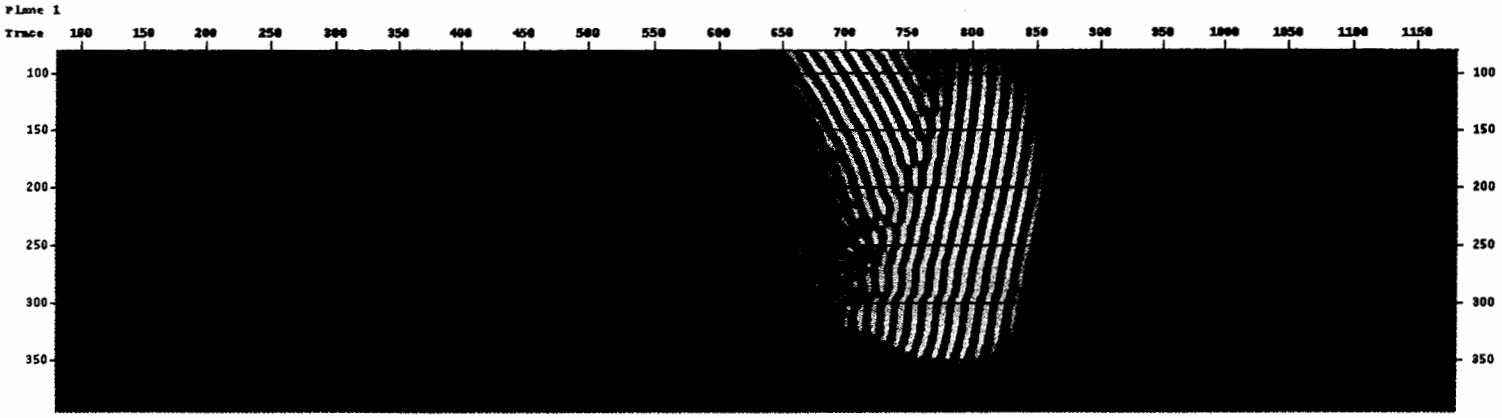
Plane 1
Trace
100
150
200
250
300
350
400
450
500
550
600
650
700
750
800
850
900
950
1000
1050
1100
1150

Figure 53 e.

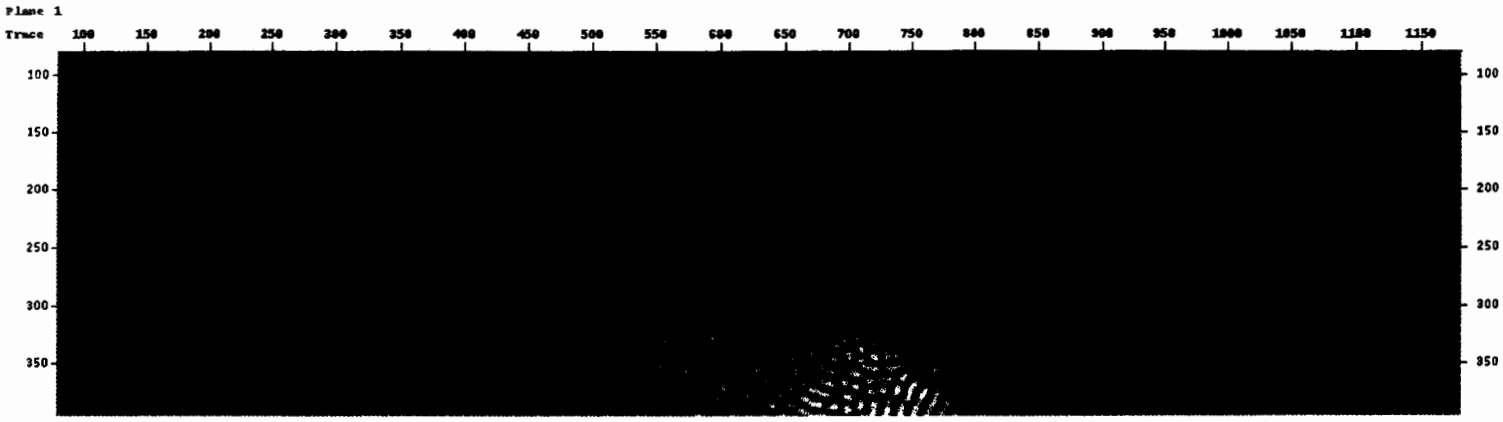
Plane 1
Trace
100
150
200
250
300
350
400
450
500
550
600
650
700
750
800
850
900
950
1000
1050
1100
1150

Figure 53 f.

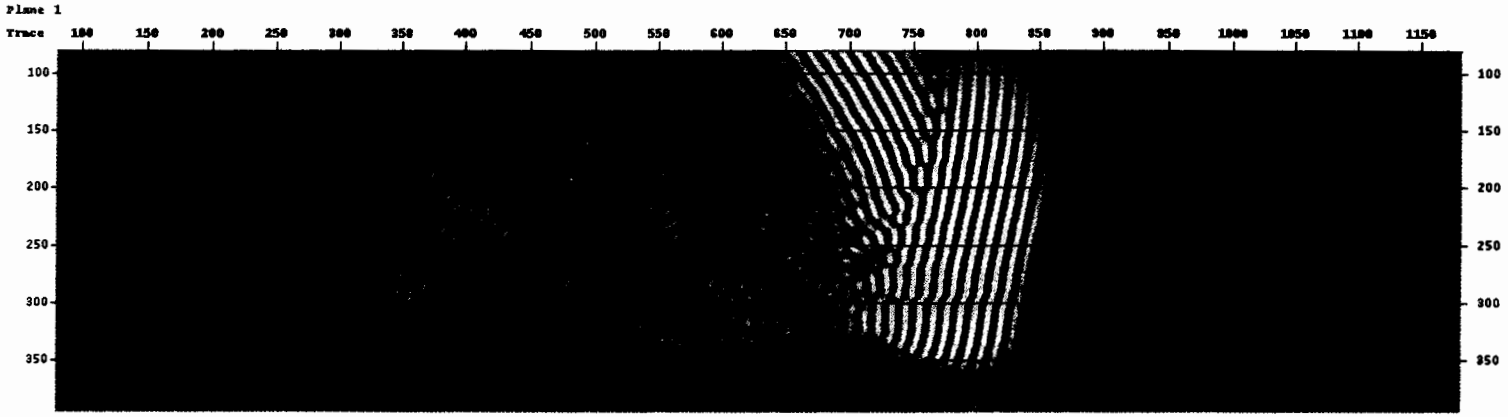
Plane 1
Trace
100
150
200
250
300
350
400
450
500
550
600
650
700
750
800
850
900
950
1000
1050
1100
1150

Figure 53 g.

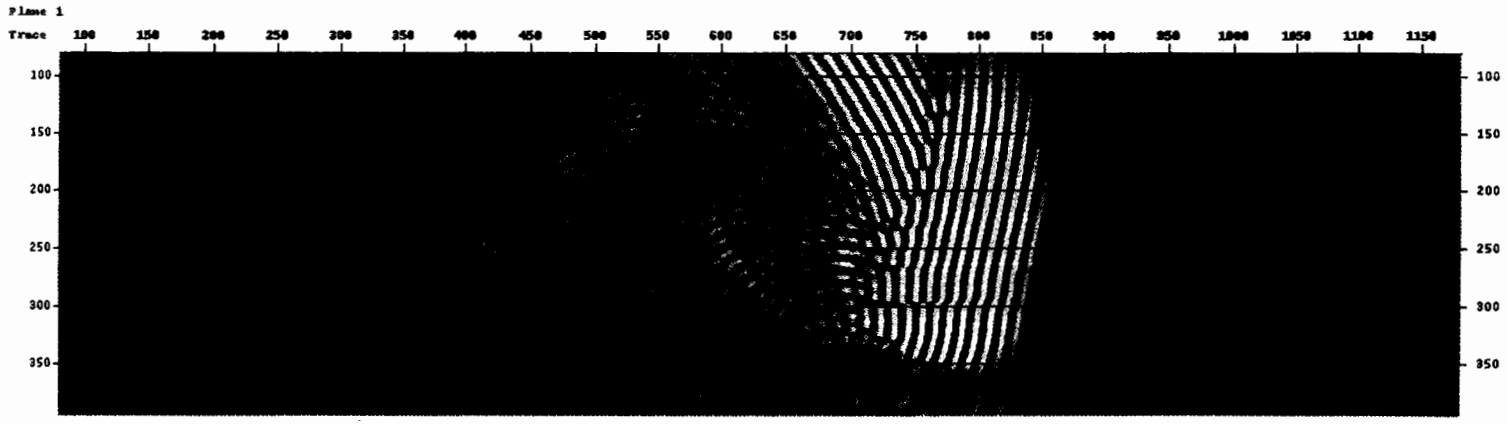
Plane 1
Trace
100
150
200
250
300
350
400
450
500
550
600
650
700
750
800
850
900
950
1000
1050
1100
1150

Figure 54.

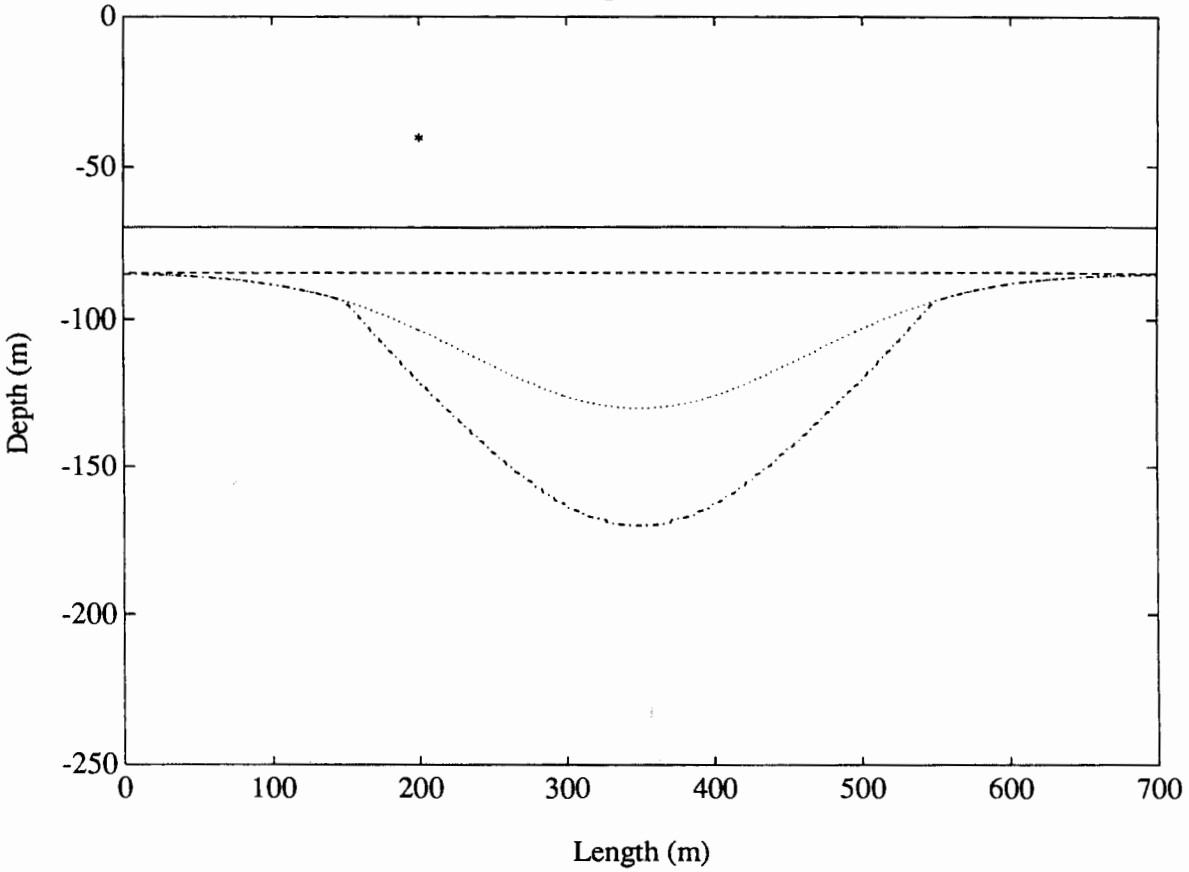
0
-50
-100
-150
-200
-250
Depth (m)
0
100
200
300
400
500
600
700
Length (m)

Figure 55.

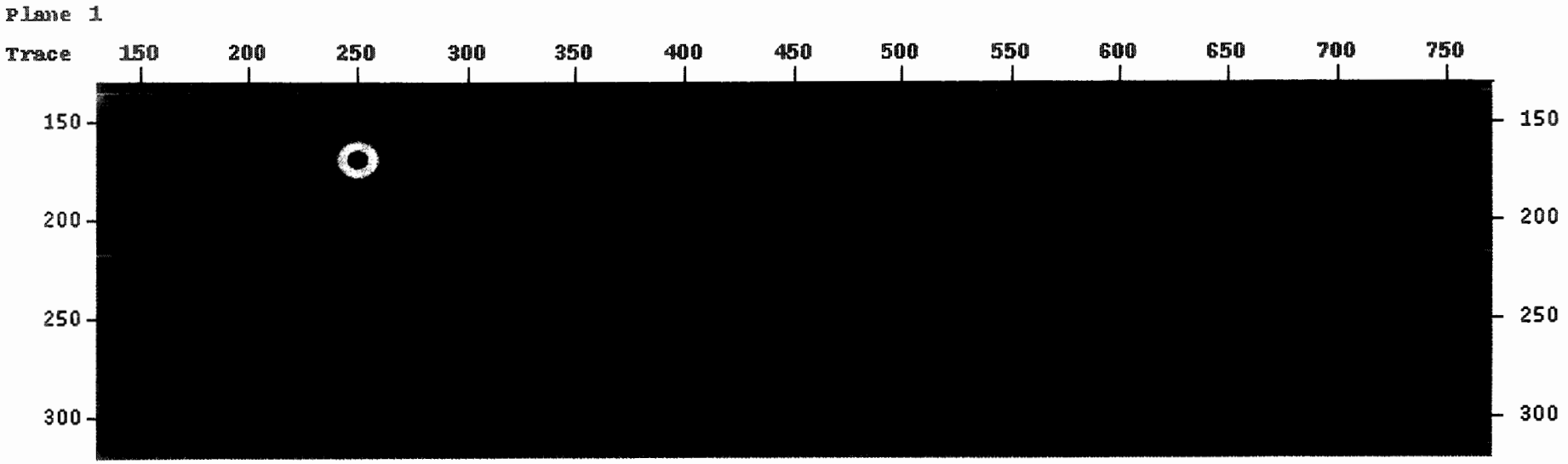
Plane 1
Trace
150
200
250
300
350
400
450
500
550
600
650
700
750
150
200
250
300
150
200
250
300

Figure 56 a.

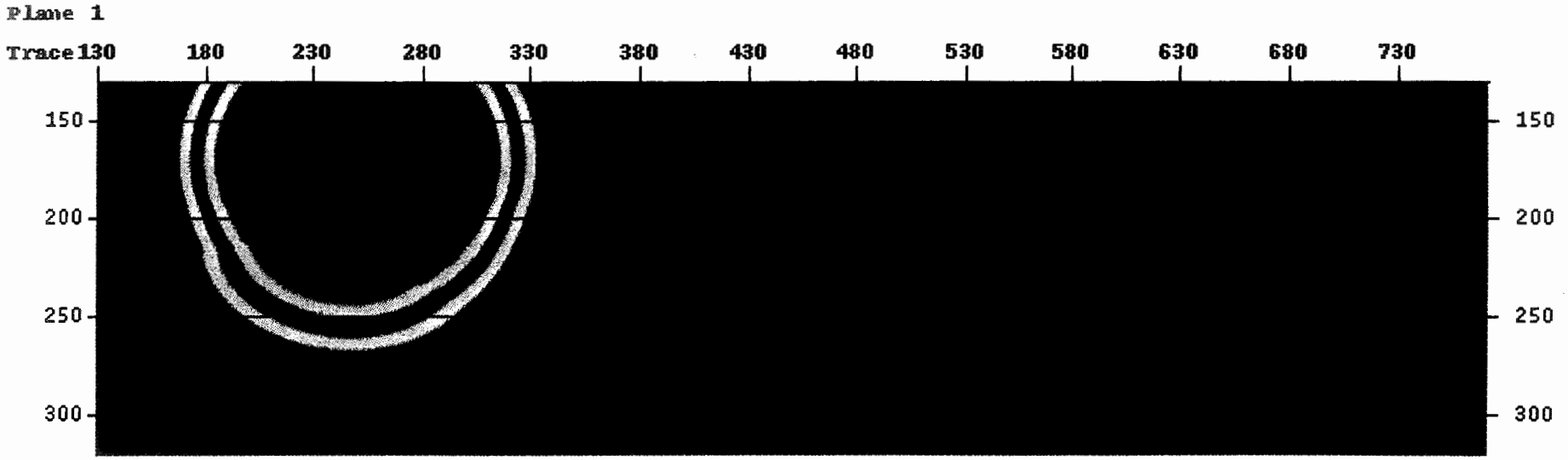
Plane 1
Trace 130
180
230
280
330
380
430
480
530
580
630
680
730
150
200
250
300
150
200
250
300

Figure 56 b.

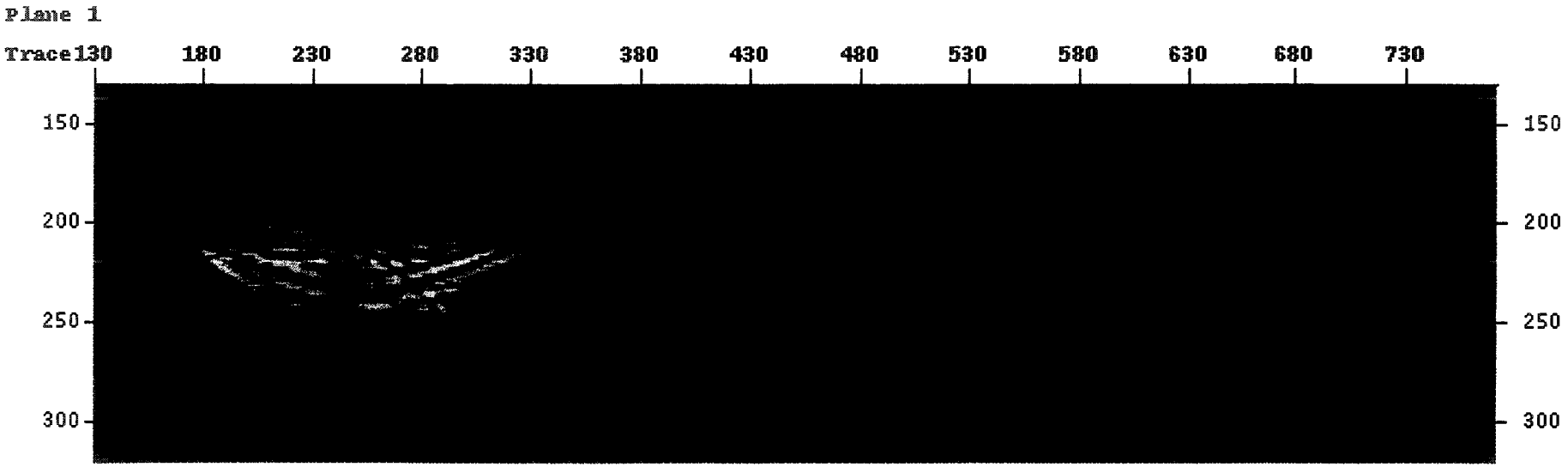
Plane 1
Trace 130
180
230
280
330
380
430
480
530
580
630
680
730
150
200
250
300
150
200
250
300

Figure 56 c.

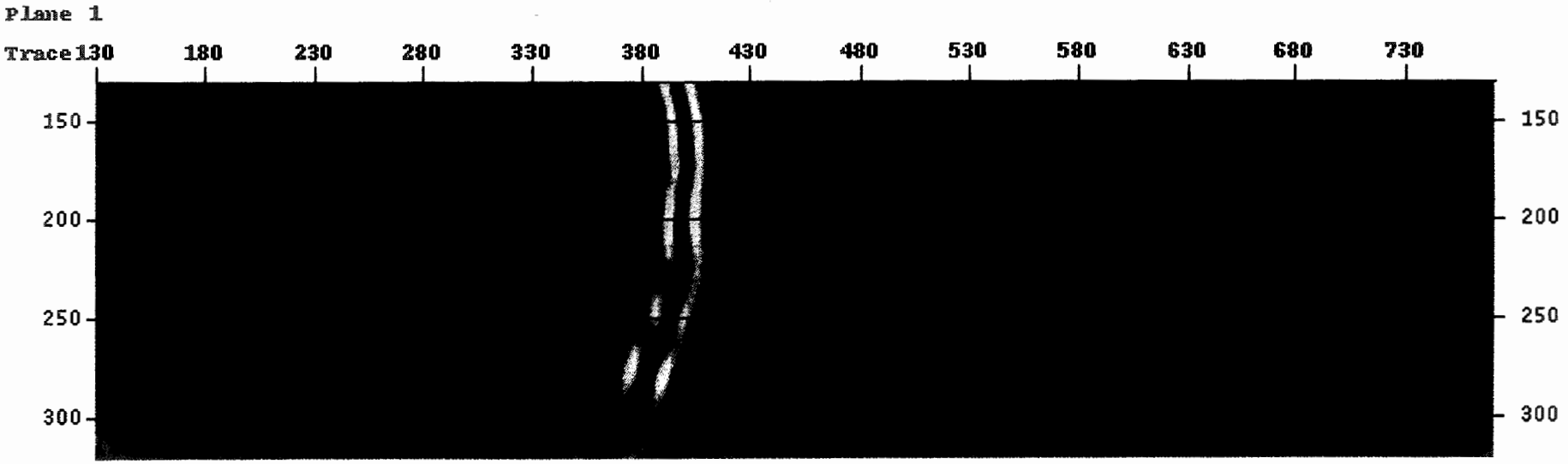
Plane 1
Trace
130
180
230
280
330
380
430
480
530
580
630
680
730
150
200
250
300
150
200
250
300

Figure 56 d.

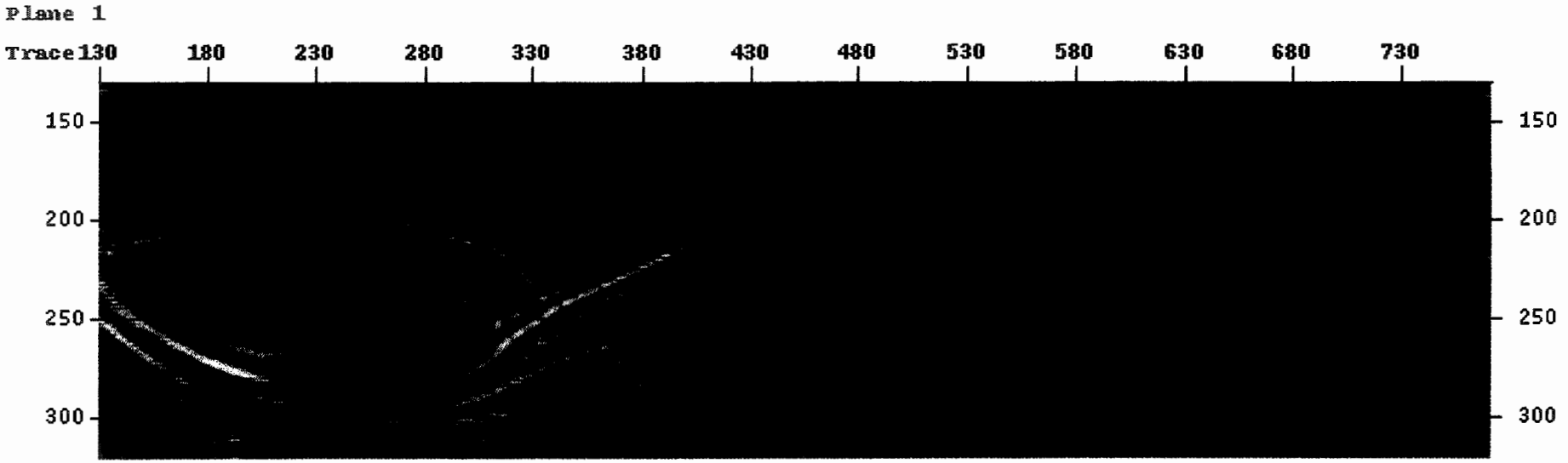
Plane 1
Trace 130
180
230
280
330
380
430
480
530
580
630
680
730
150
200
250
300
150
200
250
300

Figure 56 e.

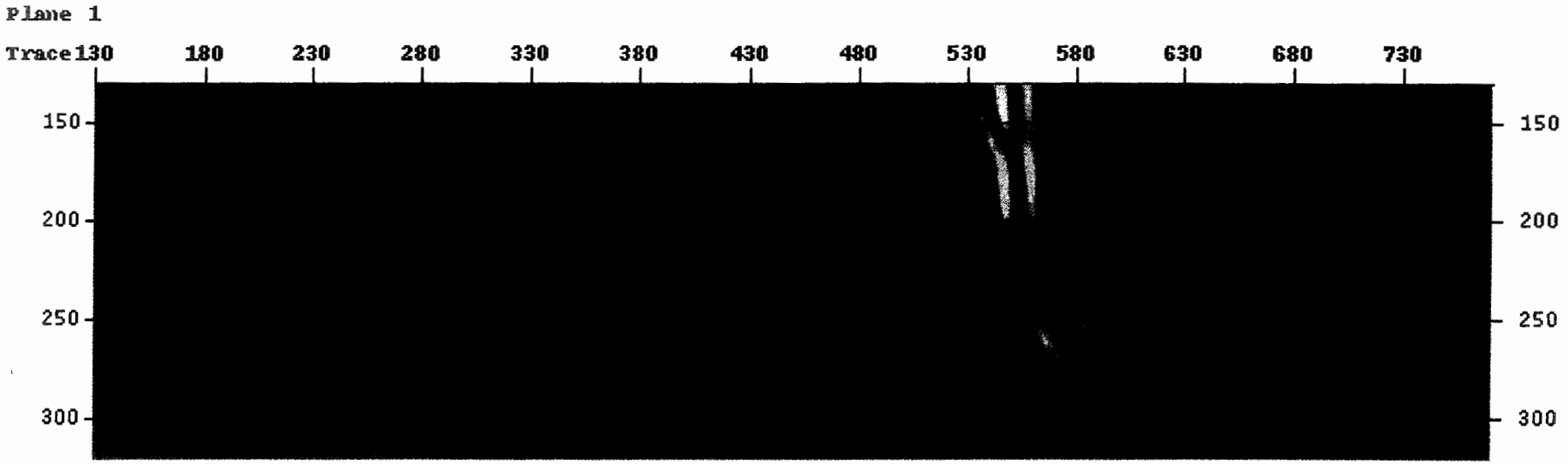
Plane 1
Trace 130
180
230
280
330
380
430
480
530
580
630
680
730
150
200
250
300
150
200
250
300

Figure 56 f.

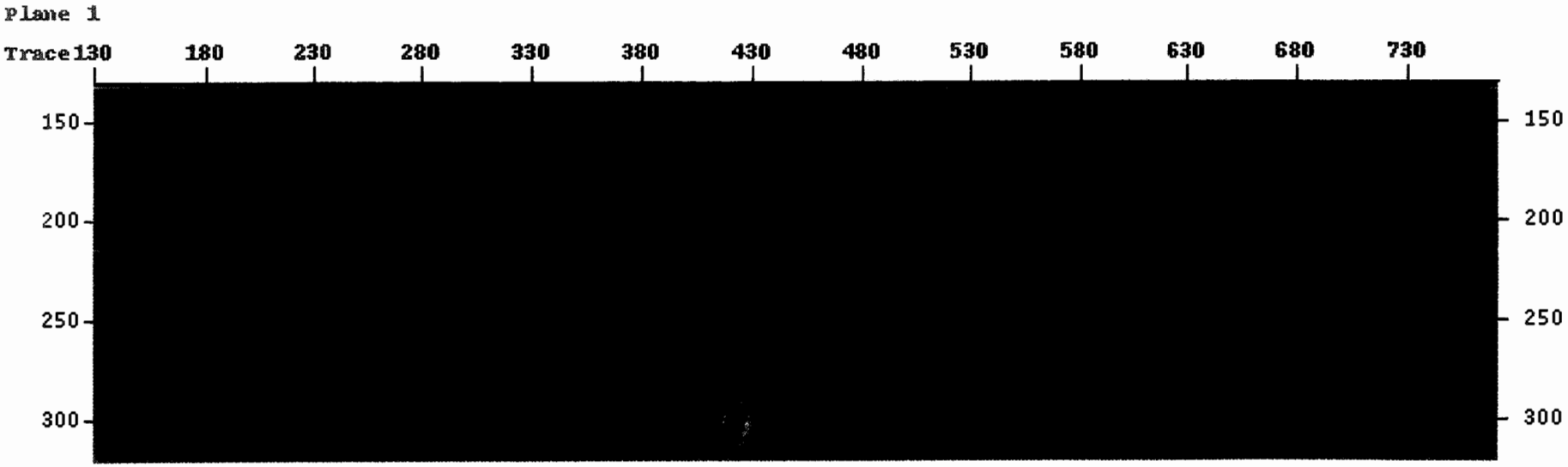
Plane 1
Trace 130
180
230
280
330
380
430
480
530
580
630
680
730
150
200
250
300
150
200
250
300

Figure 56 g.

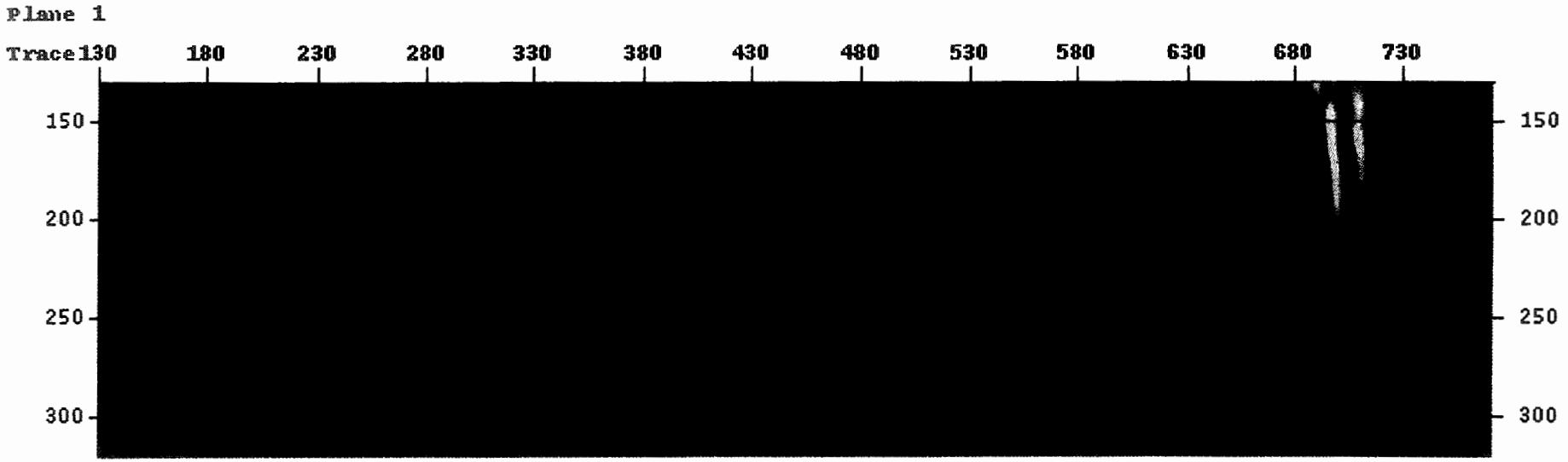
Plane 1
Trace 130
180
230
280
330
380
430
480
530
580
630
680
730
150
200
250
300
150
200
250
300

Figure 56 h.

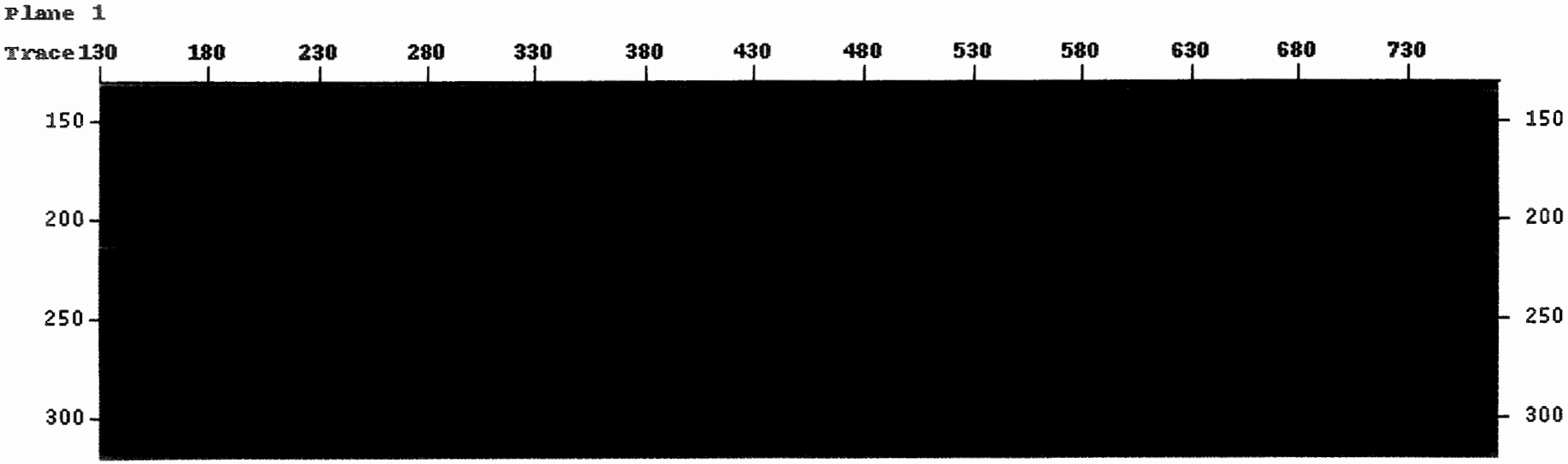
Plane 1
Trace 130
180
230
280
330
380
430
480
530
580
630
680
730
150
200
250
300
150
200
250
300

Figure 57 a.

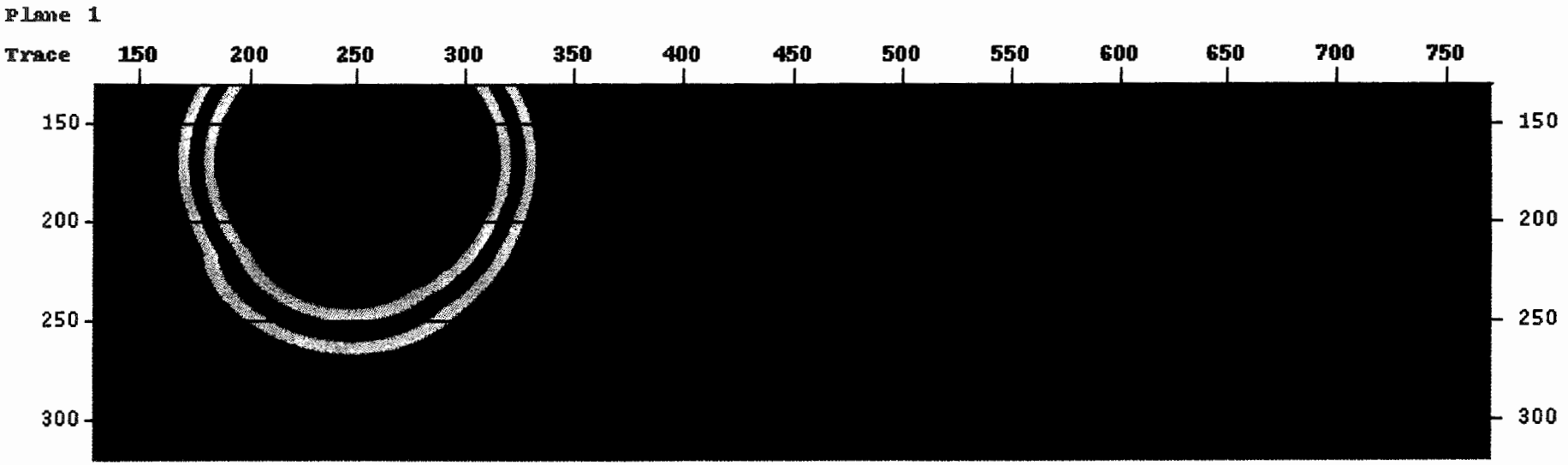
Plane 1
Trace
150
200
250
300
350
400
450
500
550
600
650
700
750
150
200
250
300
150
200
250
300

Figure 57 b.

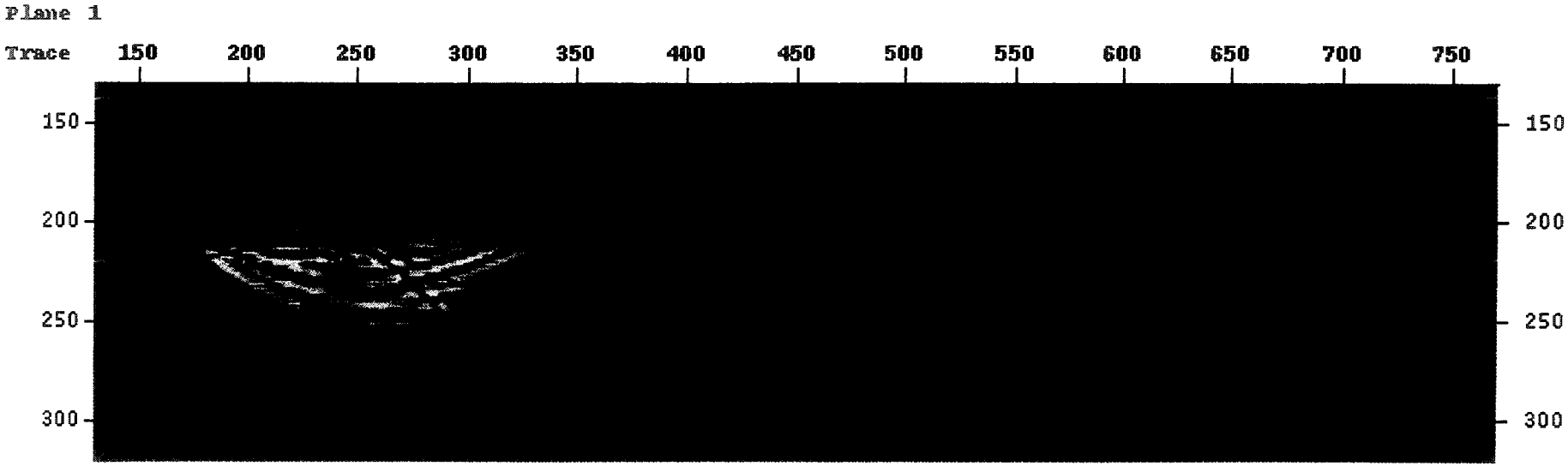
Plane 1
Trace
150
200
250
300
350
400
450
500
550
600
650
700
750
150
200
250
300
150
200
250
300

Figure 57 c.

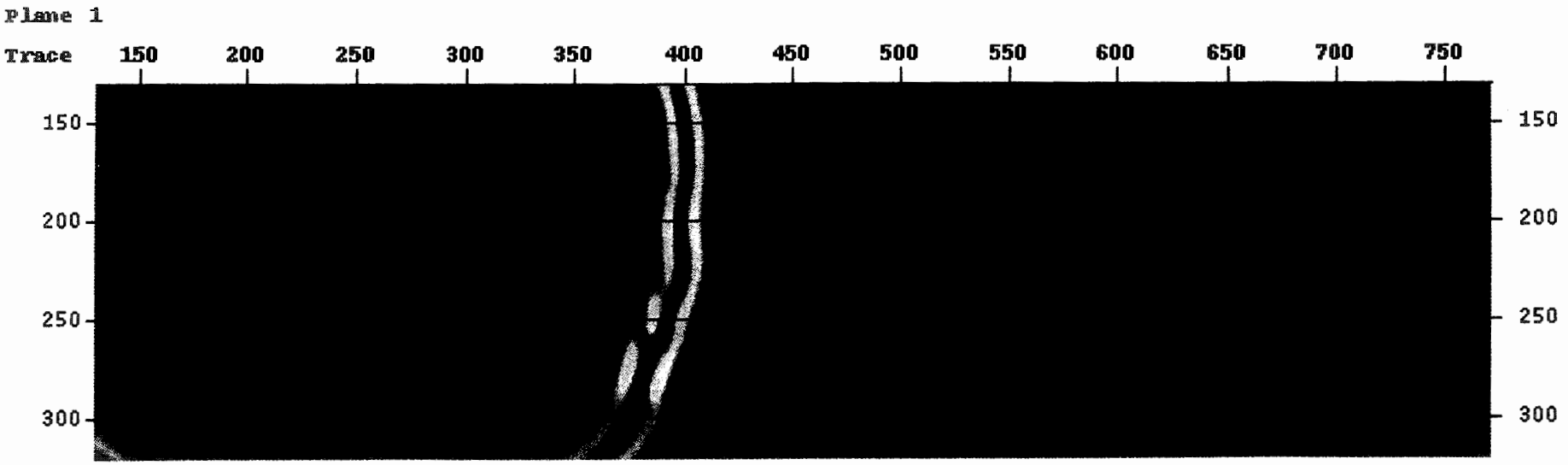
Plane 1
Trace
150
200
250
300
350
400
450
500
550
600
650
700
750
150
200
250
300
150
200
250
300

Figure 57 d.

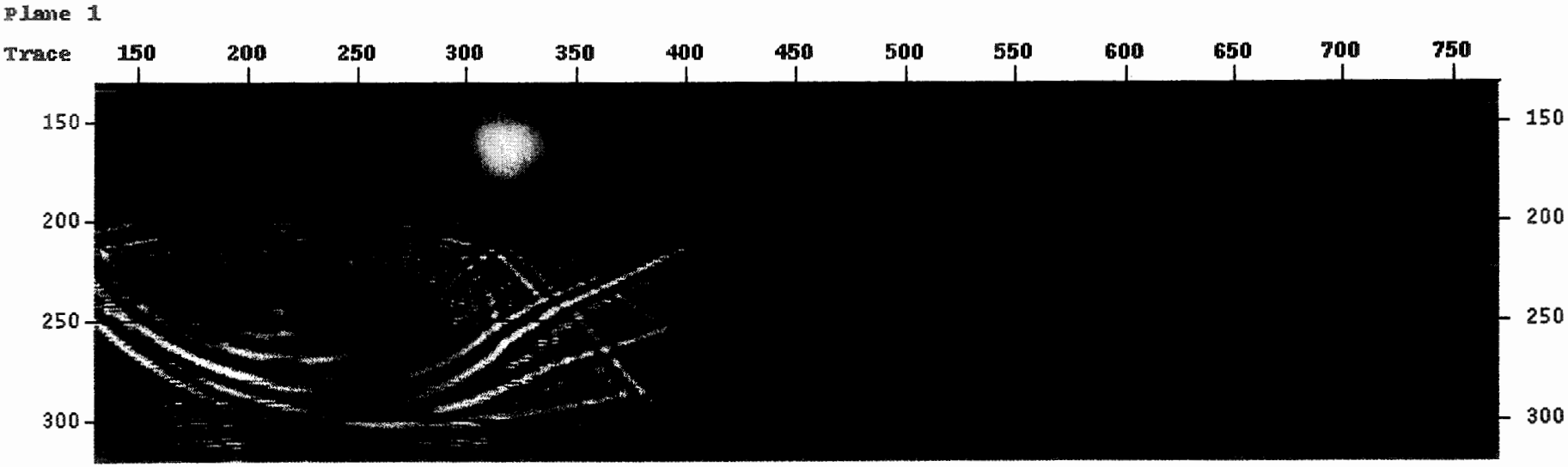
Plane 1
Trace
150
200
250
300
350
400
450
500
550
600
650
700
750
150
200
250
300
150
200
250
300

Figure 57 e.

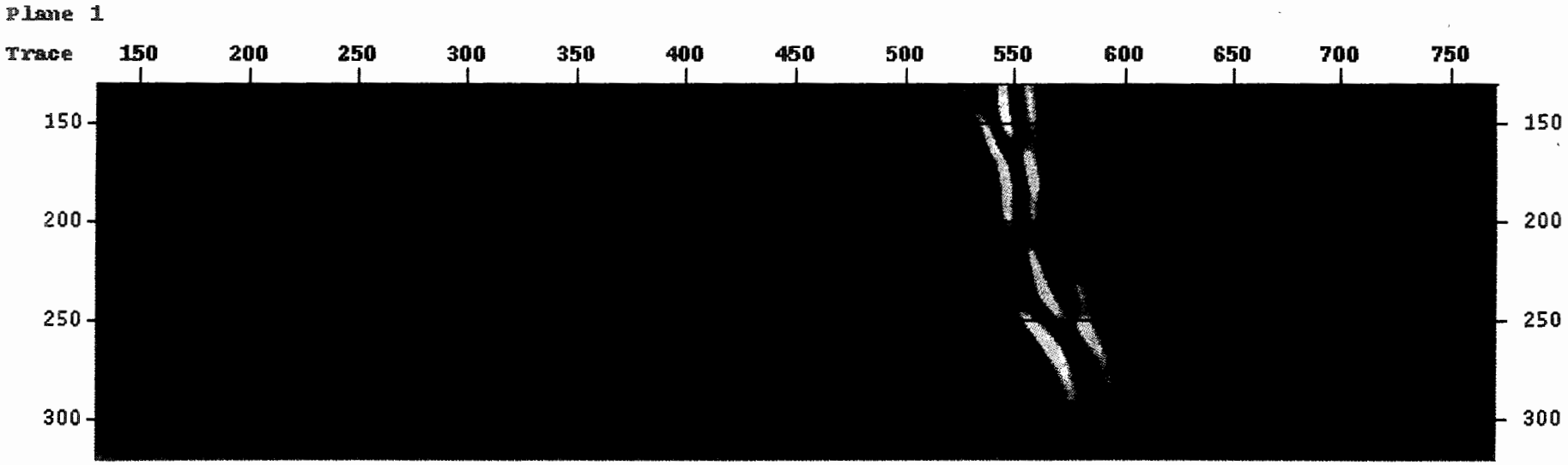
Plane 1
Trace
150
200
250
300
350
400
450
500
550
600
650
700
750
150
200
250
300
150
200
250
300

Figure 57 f.

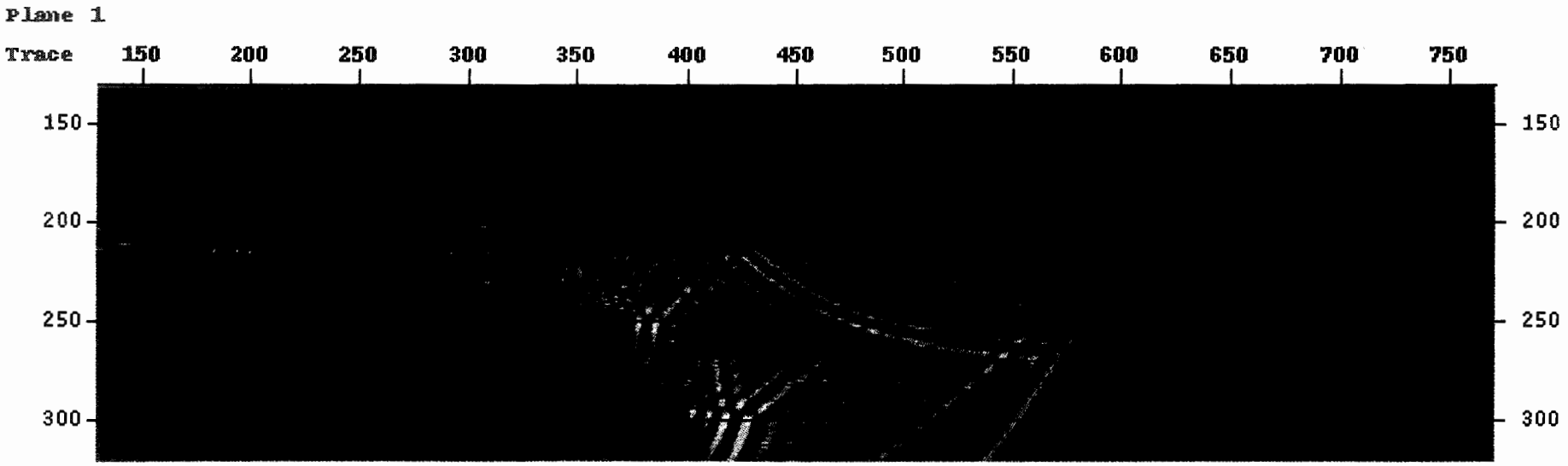
Plane 1
Trace
150
200
250
300
350
400
450
500
550
600
650
700
750
150
200
250
300
150
200
250
300

Figure 57 g.

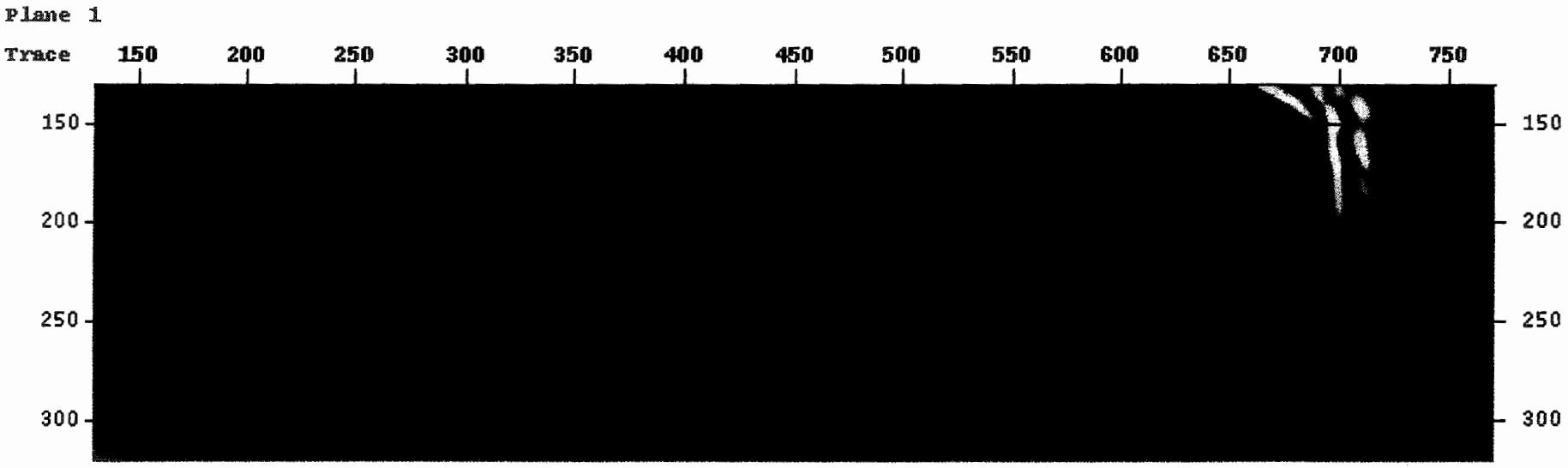
Plane 1
Trace
150
200
250
300
350
400
450
500
550
600
650
700
750
150
200
250
300
150
200
250
300

Figure 57 h.

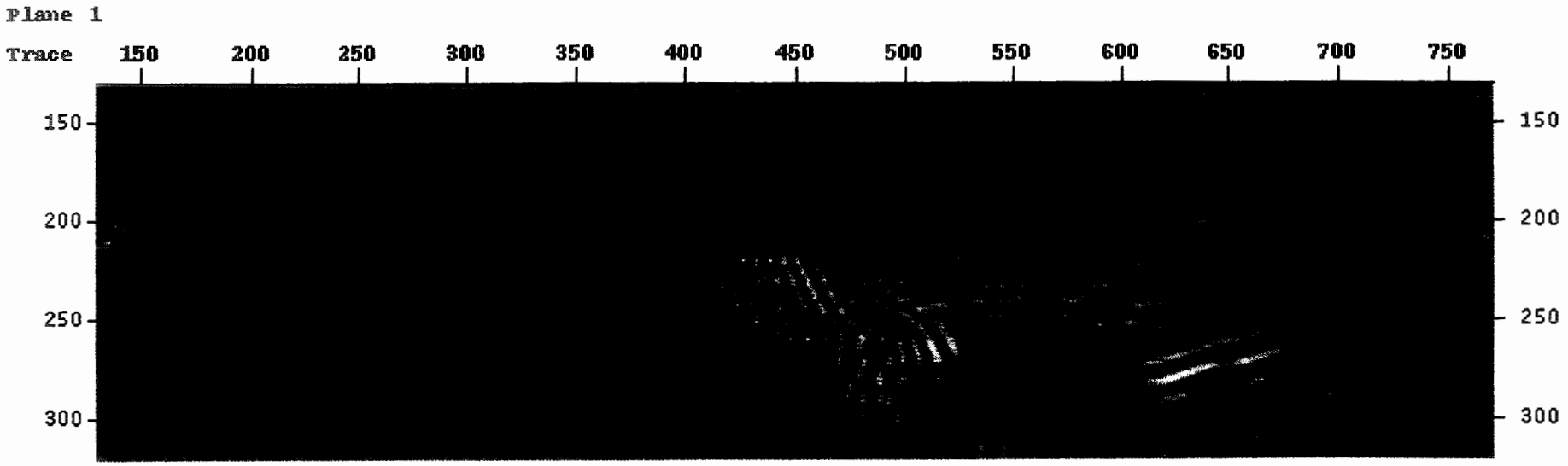
Plane 1
Trace
150
200
250
300
350
400
450
500
550
600
650
700
750
150
200
250
300
150
200
250
300